UNIVERSITÉ DE GENÈVE
Département d'informatique

FACULTÉ DES SCIENCES
Professeur B. Chopard
Professeur M. Droz

Mesoscopical modelling of complex systems.

THÈSE

présentée à la Faculté des sciences de l'Université de Genève
pour l'obtention du grade de Docteur ès sciences, mention interdisciplinaire

par

Stefan MARCONI

de
Vernier(GE)

Thèse N° xxxx

GENÈVE
2002

La Faculté des sciences, sur le préavis de Messieurs B. CHOPARD, professeur adjoint et directeur de thèse (Département d'informatique), ..., ???, professeur (), autorise l'impression de la présente thèse, sans exprimer d'opinion sur les propositions qui y sont énoncées.

Genève, le xxxx 2002

Thèse -xxxx-

Le Doyen, Jacques WEBER

But… why do you do this?
…because Nature does.

Contents

List of Figures **iii**

1 Introduction **1**

2 Solid modelling **5**

2.1 Introduction . . . 5
2.2 Theory . . . 6
2.2.1 The Navier equation of motion . . . 7
2.2.2 Examples of difficult solid modelling. . . . 9
2.3 The basic cellular automata model. . . . 10
2.3.1 Translational motion . . . 11
2.3.2 Rotational motion . . . 18
2.3.3 Conclusion . . . 23
2.4 The scalar lattice Boltzmann model . . . 23
2.4.1 Solid Dynamics . . . 26
2.4.2 Conservation of Momentum . . . 27
2.4.3 Conservation of energy and work . . . 27
2.4.4 Hooke's law . . . 29
2.4.5 Dissipation and the stationary state . . . 31
2.4.6 Dynamic boundary and contact conditions. . . . 32
2.4.7 Elastic properties . . . 33
2.5 Applications of the scalar model . . . 37
2.5.1 Collisions of solids . . . 37
2.5.2 The contact of a beam between two stops . . . 40
2.5.3 Energy at the tip of a crack . . . 41
2.5.4 Fracture . . . 42
2.5.5 Fragmentation . . . 44
2.6 Further developments . . . 46
2.6.1 Tensor coefficient . . . 48
2.6.2 $\boldsymbol{J}$-Π equilibrium . . . 51
2.7 Conclusion . . . 55

3 Incompressible Fluids **57**
3.1 Introduction 57
3.2 Theory 58
3.2.1 The Euler equation 58
3.2.2 The Navier-Stokes equation 59
3.2.3 Conditions for incompressibility 60
3.2.4 Lattice Boltzmann model of a fluid 61
3.3 State of the Art 64
3.3.1 The lattice Boltzmann pressure model 64
3.3.2 The sound speed feedback technique 66
3.4 The repulsive force model 67
3.4.1 Repulsive body force, pressure and compressibility 68
3.5 Numerical experiments 69
3.5.1 Poiseuille flow. 70
3.5.2 Womersley flow 71
3.5.3 Barometric fluid 73
3.6 Conclusion 75

4 Solid-Fluid interface **77**
4.1 Introduction 77
4.2 Summary of the lattice Boltzmann modelling of a Solid 78
4.3 Example of lattice Boltzmann models 80
4.3.1 Ladd's model 80
4.3.2 Aidun's deformable membrane 81
4.4 The solid-fluid lattice Boltzmann interface 82
4.5 Numerical Simulations 84
4.5.1 Drag experiment 84
4.5.2 Poiseuille flow 87
4.5.3 Flexible membrane 87
4.6 Conclusion 92

5 Viscoelasticity **93**
5.1 Introduction 93
5.2 Theory 94
5.2.1 Phenomenological Models 97
5.2.2 Microscopical Models 99
5.3 Lattice Boltzmann models for viscoelasticity: short review 100
5.3.1 Viscosity redefinition 100
5.3.2 Lattice Boltzmann and molecular dynamics 101
5.4 Multiple Lattice Boltzmann model for viscoelasticity 103
5.4.1 A single polymer 103
5.4.2 A polymerised fluid 105
5.5 Conclusion 108

6 A Lattice Gas Model of a Crowd **111**
6.1 Introduction 111
6.2 State of the art 113
6.2.1 The social force model. 113
6.2.2 The cellular automata model. 114
6.2.3 Conclusion 117
6.3 The Multiparticle Lattice Gas Automata Model 117
6.4 Numerical results 121
6.4.1 Lane formation 122
6.4.2 Door oscillations. 123
6.4.3 Evacuation problem 124
6.5 Conclusion 124

7 Conclusion **127**

Bibliography **129**

List of Figures

2.1 The definition of the strain-displacement relation. The strain ε is the function of x and y which gives the variation between point $\boldsymbol{P}$ and $\boldsymbol{Q}$ of the displacement $\boldsymbol{u}$ due to deformation of a solid. 7

2.2 A model to study the vibrations characteristics of mechanical joints. The problem consists in studying the vertical displacement $v(t)$ of a beam which is excited by the force $\phi(t)$ at one end while the movement of the free end is constrained by two stops. 10

2.3 A three particle string illustrating the one dimensional cellular automata rule. White particle do not move between time steps t and $t+1$. The black particle at position $\boldsymbol{r}$ jumps a distance $2\boldsymbol{\delta}$ over the geometrical center of mass of the neighboring particles. . 11

2.4 The position update rule of the 1d cellular automata illustrated with a black particles in the bulk (left) or on a border (right). The motion consists in a displacement of $2\boldsymbol{\delta}$ where $\boldsymbol{\delta}$ is defined slightly differently for each case. For a bulk particle $\boldsymbol{\delta}$ is the distance to the geometrical center of mass of the two neighbors. On the border, it is the distance to the tip of the spring as if it were at rest and connected to the neighbor. 12

2.5 The definition of intermediary variables for the dynamics of the cellular automata. The vectors $\boldsymbol{f}$ and $\boldsymbol{f}$ are the distances of the black particle to the tip of the springs as if they were at rest and attached to the neighboring particles. In terms of these $\boldsymbol{f}$ fields, the dynamic of motion simply consists in exchanging $\boldsymbol{f}$ and $\boldsymbol{f}$. . . 13

2.6 The dual relation between the $\boldsymbol{f}$ fields with regards of which particles is being considered. If the black particle is under consideration then the field $\boldsymbol{f}$ is defined. Alternatively, if the white particles is considered then it is $\boldsymbol{f}$. Therefore by writing that $\boldsymbol{f}(k) = -\boldsymbol{f}(k-1)$, we are simply stating that the distance between the two particles is the same for both points of view. 14

2.7 The motion of a one dimensional object using a cellular automata. This instance of the automata produce a motion in a discrete space. The overall motion is the result of the motion of each individual motion in a caterpillar-like way since the black and white particle are update alternatively. The speed of the chain can be calculated from the time and the distance it takes to return to the initial configuration, in this case 2/8. 15

2.8 The 2d cellular automata rule illustrated for the black particle. The distance to the springs of the two extra particles are defined using the fields $\boldsymbol{f}$ and $\boldsymbol{f}$. The black particle jumps over the center of mass of the four neighboring springs. 16

2.9 The motion of a two dimensional object using a cellular automata. 17

2.10 To model a rotation with a cellular automata, we connect particles with torsion bars. The state of the bar is then describe by an angle, θ or θ, depending on the particles considered. The rotational motion of the particle is approximate by the vector $\Delta\boldsymbol{r}$ which joins the to symmetric positions of the torsion bar. 19

2.11 The elementary motions used in order to create a rotating object. In analogy to infinitesimal rotation, the arc of rotation is approximated by the vector joining the new and old positions. The total rotation is obtained by linearly adding the rotations in the x and y directions. 20

2.12 Three examples of rotations with initial displacements angles $\theta = \pi/50, \pi/10, \pi/4$. The left pictures are that of the x position of one particle during simulation plotted against the corresponding perfect circle trajectory. The right pictures are the trajectories of a particle (the outer line) and the center of mass of the two particles (the inner line). 21

2.13 The rotation of a chain with 11 particles. The outer line is the trajectory of one of the border particles. Again while no physical quantity has clearly been identified, the scheme is remarkably stable and the chain keeps its integrity. 22

2.14 A spiraling chain resulting from a non uniform choice of angle θ in the chain. The size of the chain diverges which indicates that the angles chosen must obey some criteria in order to keep the integrity of the chain. 23

2.15 A particle, its four neighbors, the $\boldsymbol{f}$ fields and the rest lengths Δ between particles used in the dynamics of our model. 29

2.16 A one dimensional 2 particle system considered to study the elastic property of the model. 33

2.17 Deformation of a simple 2D solid. The original and final particle positions are shown, as well as the internal forces (thin arrows) and external forces (fat arrows). 35

2.18 The upper plots concern a system of two independent colliding particles while the lower plots are for a system of two chains of five particles each: the trajectory of the chains (left) and their kinetic energy $E = \sum f2$ (right). The duration of the interaction is easily expressed as the transient of right plots and we observe that it is dependent of the size of the chain. 38

2.19 The trajectory of two chains particles colliding with a microscopic elastic exchange of momentum (left), their kinetic energies (middle) and their total energies $E = \sum f2$ with the total energy of the system remaining constant (right). The non conservation of kinetic energy during the interaction is the clear sign that the collision is inelastic. 39

2.20 The setup of the simulation is illustrated on the top pictures for two different iteration steps. One end of the beam is fix and forced with an oscillating motion while the other end is free to move but constrained by two stops. The bottom plots show the position of the free end as a function of time (left) and the fourier transform of this signal (right). 41

2.21 The stress field at the tip of a crack. (left) the solid is initiated with a crack in its center and a uniform mode-I load is applied. (right) The stress field in the direction of the load is measured as of the tip of the crack level along the axis parallel to the crack. As expected from theory, the plot fits with a power-law with exponent equal to -2.0 far from the tip while near to the tip the exponent decreases but does not attain the expected value of $-1/2$. 42

2.22 A smooth fracture (left) and a branching fracture (right). Both fracture are obtained with an initial notch in a solid under mode-I load. The parameters which distinguish the results of the simulation are the dissipation in the solid and the disorder on the threshold of fracture. 43

2.23 The speeds of smooth and branching fractures. As is known experimentally, we see that the transition between the two types of fracture occurs at about half the speed of sound. 44

2.24 The spatial distribution of fragments for several time steps of simulation. The destruction of the solid is achieved by initiating all the $\boldsymbol{f}$ at a value near to the fracture threshold. The resulting size distribution of fragments follows a power-law distribution. 45

2.25 The size distribution of fragments in a typical fragmentation experiment. The distribution follows a power law with exponent equal to ~ 1 as has been seen in experimental data where the exponent ranges from 0.5 to 1.0 46

3.1 The base vectors of a D2Q7 or hexagonal lattice. The population of rest particles, i.e. the particles which do not propagate, are associated with direction $\boldsymbol{v} = 0$ which is the label for the site itself. 62

3.2 The Poiseuille flow velocity profile with repulsive force coupling constant $W = 0.17$. The velocity is unaffected by the addition of the repulsive force (left). The evolution of the mean density profile along the longitudinal direction (right); as the value of the coupling constant W of the repulsive body force between lattice sites increases, the gradient of the density profile decreases thus illustrating the convergence to incompressibility achieved by the scheme, see figure 3.3. 69

3.3 The density gradient along the longitudinal direction of a Poiseuille flow as a function of the coupling constant W of the repulsive force between sites. We see that the artificial density gradient is reduced by a factor 3 of the original value. Higher values of W are not reachable for numerical instability reasons. 70

3.4 (left) The Womersley flow velocity profile $u(y, t)$ across the channel at times $T/8$, $T/4$, $3T/8$ and $T/2$. The frequency of the drive is $\omega = 2\pi/T$ with $T = 1000$ and the Womersley number is thus $\alpha = 0.7$ (right) The residual density gradient along the channel for $W = 0.0$ and $W = .017$. 71

3.5 (left) The relative global error as a function of frequency of the pressure gradient. The upper curve is obtained with $W = 0.0$ while the lower curve is for $W = 0.17$. The value of the error mostly due to the value at the inlet. Therefore, the ratio of the errors (right) shows the improvement due to the incompressible scheme. At low frequencies, the error is thus reduced down to 25% of its original value. 72

3.6 Fluid at rest with gravity field.(left) Density profiles for various W. (right) Inverse of the density gradient. The plot behaves as $\approx W{-}1$ as expected from equation (3.59). 73

3.7 (left) Pressure p(y) in the fluid for $W = 0.0$ (circles) and $W = 0.17$ (crosses). We see that the pressure tends to be almost linear only for the value W which is confirmed by the plot of the pressure gradient(right). 75

4.1 The speed of fluid inside a solid. For a 10x10 square solid under traction in the x direction, we measure the normalized difference $\epsilon = |\frac{u-u}{u}|$ of velocity between a solid and a fluid site. The plot is that of the mean difference $<\epsilon>$ in both directions. We observe that apart for a thin layer on the boundaries facing the flow,the fluid inside a moving solid has the same velocity. 83

4.2 (left) the evolution of the velocity of the cylinder follows $u(t) = \frac{F}{a}(1 - e{-}at)$. (right) Stokes law for a cylinder; as expected we have $Cd \propto Re{-}1$ up to Reynolds number of a 100. 85

4.3 The left plots are the velocity profiles of a uniformly accelerated fluid contained within a solid at $t = 2000$ where the circles are the numerical experiments values and the crosses are the theoretical values. The viscosity of the fluid is $\nu = 0.125$. The right-hand plots are the error to the theoretical expression of the velocity. The top plots are a obtained with classical bounce-back scheme on walls and no solid and serve as reference. The middle plots are obtained with a rigid solid body $k = 10$. The bottom plots are with an elastic solid $k = 1/150$ and this causes the fluid contained in the solid to flow inside the solid whose permeability is now clearly observable. 86

4.4 The motion of a test particle in solid forming the boundary of a fluid driven by a pressure gradient. 88

4.5 Flow of a lattice Boltzmann fluid contained within a lattice Boltzmann solid at $t = 1000$. The solid is represented by circles and the fluids velocity field is represented by the contour lines of the norm of the velocity $\| \boldsymbol{u} \| = \sqrt{u2 + u2}$. 89

4.6 Flow of a lattice Boltzmann fluid contained within a lattice Boltzmann solid at $t = 1200$. The solid is represented by circles and the fluids velocity field is represented by the contour lines of the norm of the velocity $\| \boldsymbol{u} \| = \sqrt{u2 + u2}$. 90

4.7 The velocities of a lattice Boltzmann flow contained within a lattice Boltzmann solid. We observe that u is one order of magnitude larger than u demonstrating that although the solid is permeable most of the flow is in the direction parallel to the channel. 91

4.8 (left) The gradient of pressure in the direction normal to flow and (right) the shape of the solid serving as boundary. We see that the gradient peaks where the solid is most strained by the flow. 91

5.1 The Maxwell model for viscoelastic solid (1867). Viscoelastic behavior is obtained by arranging an elastic spring and a viscous irreversible component in series. In the same spirit, other models are therefore possible such as the Kelvin-Voigt model where the components are mounted in parallel. 98

5.2 The shape of the polymer placed in a shear flow at four different time steps. The polymer is initially orientated in the direction normal to the flow as the velocity (arrows) of the fluid at the particles positions shows. The chain then deforms in the flow while still keeping its integrity. Note however that the extension in the x direction is largely affected as the scale of the x axis shows. This is due to the fact that the polymer is chosen with elastic constant $k = 1/100$ which corresponds to a relatively high elasticity. 102

5.3 The orientation of a single polymer during time. The angle $\theta\circ = \arctan(ly/lx)$ is obtained by computing the ratio of the horizontal extension lx and vertical extension ly. We clearly evolve from a polymer normal to the flow towards a polymer with an angle of 20○. The fact that the polymer does not orientate is either due to the lack of rotational invariance at the end particles or to some more sophisticated physical effect. 103

5.4 The upper plots are the variation of horizontal and vertical extension of a single polymer in a shear flow. The oscillating nature of this variation shows how the polymer reacts to the extension imposed by the flow and demonstrates the finite extensibility of the model. The lower plots show the speed of the center of mass of the polymer. The overall motion is thus a complex combination of forward and backward movements in the flow. 104

5.5 Velocity profiles for a plain fluid and a fluid with 2000 polymers perpendicular to the flow. The flat profiles is however still a linear shear flow profile. The gradient differs of almost two orders of magnitude: the plain case exhibits a slope of 0.01 while for the perpendicular case it is worth 0.00022 leading to a apparent viscosity 45 times higher. 105

5.6 The Deborah number De as a function of the density κ of particles in a fluid under shear stress. The characteristic time scale used to calculate the Deborah number is the time needed for a plain fluid to establish a shear flow. This explains why the Deborah number starts at 1. We see that for the given elasticity constant $k = 1$ of the polymers, we are able to obtain a range of Deborah numbers by tuning the density of polymers in the flow. 106

5.7 The dependency of the gradient of u as a function of shear stress. The relation is linear, however the linearity constant and hence the viscosity depends on the ratio ζ between parallel and perpendicular polymers. The two plots are for a total of 2000 polymers and $\zeta = 1$ and $\zeta = 1/3$ 107

6.1 Flow oscillation of pedestrians at a door serving as a bottleneck, taken from [1]. The arrows represent the speed $\boldsymbol{v}$ of each pedestrian. The top situation shows the right population having gained passage through the door while in the bottom situation the flow is inversed. Both population act as pressure on each other and it is the fluctuations which allow for one pedestrian to pass through the door. Once the first pedestrian gains access, it is easier for the others to follow until the situation inverses again. 115

6.2 Jamming at a door of pedestrian while evacuating a room, taken from [2]. The evacuation problem shows the interesting phenomena of "faster-is-slower". If the crowd moves to the door too quickly, interaction between pedestrians is higher and the total evacuation time is larger. This result has direct implications in evacuations procedures or more precisely in preventive education of pedestrians behavior. 116

6.3 The two phases of a lattice gas algorithm. Pedestrians coming from neighboring sites interact in the central site. This results in a redistribution of the pedestrians among possible directions including the rest direction which means a pedestrian will not move during this time step. The propagation step merely consists in moving a pedestrian to the site pointed at by the direction resulting from the collision term. 118

6.4 A pedestrian may consider several directions in order to find alternate routes. The parameter ξ determines the number of directions neighboring his favored direction $\boldsymbol{c}$ that are to be taken into account 119

6.5 Lane formation in a crowd. Three different situations are depicted, which correspond to different values of the models parameters. The left picture shows a crowd with no lanes: movement is essentially a sequence of collision with no deviation. The center picture shows the presence of dense lanes where pedestrians strongly follow each other. The right picture shows a sparse lane where pedestrians spread over the whole space. Black triangles indicate cells in which the mobility points to the left, whereas white ones indicate that the mobility points to the right. A cross shows a cell with zero mobility. 121

6.6 A measure of total mobility in a crowd for the three cases shown in figure 6.5:(squares) no lanes $\lambda \approx 0, \eta \approx \frac{1}{2}$, (diamonds) dense lanes $\lambda \approx 1, \eta \approx \frac{1}{2}$,(line) sparse lanes $\lambda \approx 0, \eta \approx 1$. Note that the maximum value of the total mobility is 2500, i.e. the total number of pedestrians. 122

6.7 Measure of total mobility(left) and its Fourier transform(right) at a door of width 3 in a 200×50 hexagonal lattice with a wall at $x = 100$. The bottom plots are obtained with pedestrians who do not interact. This measure serves as a test of the noise at the door due to the initial random configuration of the crowd. The top plots are the ones with an interacting crowd: we observe higher amplitude peaks at low frequency showing that the two crowd gain access through the door with oscillations. 123
6.8 The evacuation of 2500 pedestrians out a room through a single door. Initially the crowd is randomly distributed. In the first few time steps, the whole crowd gathers around the door and creates jamming. The time of evacuation as a function of the disorder parameter ξ is shown on figure 6.9. 124
6.9 The time T needed to evacuate a room as a function of λ. Low λ means people do not consider other directions than the favorite one. The plot shows that by increasing the directions considered and thus slowing the mean velocity to the door, higher throughput is achieved and the total evacuation time is reduced. The plot is the result of single runs with all pedestrians on one side of wall with a door of size 3. 125

Chapter 1

Introduction

E pur si muove.
Galileo Galilei

Galileo is famous for several reasons: he invented the telescope; in his *Dialogues Concerning Two New Sciences* (1646) he presents the basis of mechanics and elasticity; finally he was put in front of the inquisition for defending the heliocentric system invented by Copernicus. All these reasons are important, either technically or scientifically. Strangely, the telescope is a beautiful invention for both reasons. Indeed, it is an invention but ultimately it also contains in it the concept of levels of observation. With it, man can see in full details objects which are far and through a microscope see the details of objects which are too small for the eye. Through it, Science has therefore vastly opened up its field of investigation. Will it be possible to describe everything in full details? Is it really necessary? The answer is no, not all the details are necessary: it is possible to put oneself at an intermediate or mesoscopic level of description and leave the details out.

The subject of this thesis is the mesoscopical modelling of complex systems. This introduction ultimately wants to explain how topics as diverse as solid dynamics, fluid dynamics and pedestrian dynamics can be apprehended in the same way. To do so, allow us to briefly summarize four centuries of science into the following words: observe nature, translate its behavior into mathematical equations and learn how to solve mathematical equations. Fulfilling such a program, entitles one to boldly state having understood Nature and being able to predict its behavior. The success of the method is obvious to contemporary man surrounded as he is by modern technology. Nevertheless, the fulfillment of this program rest highly on the capacity to solve mathematical equations and mathematics as such obviously has its limits. Fluid dynamics for example is still a very active area of research even though the equation describing it is relatively easy to put down on paper. Solving the equation on the other hand is difficult. The difficulty is not purely technical, it is also inherent to the problem. In the case of a fluid, everyone is acquainted with the numerous pattern one may observe in the current of a river. Therefore, even the simplest equation must be able to reproduce such complex behaviors. This ability to produce all sort of behaviors from simple laws is called complexity. It is also the catch 22 of the mathematical approach. Eventually all science tries to understand and control phenomena by studying the simplest cases. Often, the simplest cases teach us practically all there is to know about a subject; other times, not at all, since the assembly of simple things can produce complexity. Nonetheless, mathematics possesses highly powerful tools in the form of numerical analysis. The purpose of numerical analysis is to calculate the best approximations to a given equation. The calculation may be tedious but the coming of modern computers, has had tremendous consequences into solving equations with no known solutions. Nevertheless, once the limits of an approach have been reached it is legitimate to try to find other ways of doing science.

The models to be found in this thesis belong to a different approach of science. The basis of this approach consists of statistical physics and computers. Statistical physics has provided the tools and intellectual framework to explain how the microscopical world of atoms and particles leads to the macroscopic world we all experience. The power of modern computer, on the other hand, enables one not only to solve equations but also to directly simulate the same microscopical elements and numerically observe the macroscopical behavior emerging from them. We can therefore state that

Physics is in the computer.

Some problems, such as the direct simulation of a dynamic fracture in a solid atom by atom, are still limited either by the computation time or the memory needed. It is therefore necessary to distinguish two very different purposes for performing simulations. Either one needs a very precise numerical solution to a problem as for example an engineer building a bridge and considers that eventually the computers will become more and more powerful. Or one wants a qualitative confirmation that the essential ingredients of a physical process have been understood. In this case, statistical physics teaches us that not all the microscopic details are necessary to understand and reproduce macroscopical phenomena. The ability to leave out details and only keep the essential ingredients consists in adopting a mesoscopical or intermediate level of description. Ultimately, even with the mesoscopic approach to modelling, one ultimately would like to create numerical scheme which an engineer will come to use. Indeed, because the details have been left aside, the real ambition is to produce numerical schemes which are more efficient and therefore more attractive than classical ones. To satisfy this ambition, it is wise to be patient and not to get discouraged by the limits our models will encouter in modelling complex phenomena. It is indeed a difficult task to follow Einstein's motto

Everything should be made as simple as possible, but not simpler

With these ideas in mind, it is honest to say that the models presented in this thesis have yet to come to maturity. Nonetheless, what they teach us is clearly of great value when the potential achievements are considered. This thesis is divided into five subjects and corresponding chapters. Each subject constitutes an example of the mesoscopical approach to modelling. By this diversity, we thus aim at demonstrating the power of this approach.

1. The modelling of solid dynamics. This chapter deals essentially with the lattice Boltzmann modelling of the Navier equation of linear elasticity. As far as we know, the results in this chapter constitute the only attempt at modelling solid dynamics within the lattice Boltzmann community. The stakes at hand is therefore no less than completely opening up the field of classical solid dynamics to the lattice Boltzmann approach.

2. The modelling of incompressible fluids. Within the classical Boltzmann model of fluid dynamics, we propose a numerical recipe based on a physical principle to diminish the residual compressibility of the scheme. Other models have been proposed which either simplify the problem loosing some generality or make use of a numerical technique which has no physical basis. Our technique works well and is only limited by the appearance of numerical instability when incompressibility is nearly reached.

3. The modelling of the solid-fluid interface. This model combines the lattice Boltzmann solid and fluid models to create a solid interface containing the fluid. The goal is to have a dynamically changing border to the fluid as would be expected with blood in arteries, for example. The interaction between the the fluid and the solid is easily modeled with a local transfer of momentum. Although the solid is not impermeable, nor is it in other models, we are able to reproduce much of the qualitative behavior expected from such an interface.

4. The modelling of viscoelastic fluids. This chapter combines the lattice Boltzmann models of solid and fluid dynamics in order to model the viscoelastic phase of matter. Particles or polymer-like chains are modeled with the solid model and immersed within a lattice Boltzmann fluid. We show that the presence of the solid particles enables to modify the behavior of the fluid.

5. The modelling of a crowd. Using the paradigm of lattice gas, we model the motion of a crowd, each particle being an pedestrian. The update rule however is constructed such as to reproduce the behavior observed in

crowds. Example of complex crowd behavior is the formation of lanes in two crowd moving in opposite direction. The novelty of this model is to have relaxed the principle that no two pedestrian may occupy the same physical location at the same time. This is the ingredient which enables to use the lattice gas paradigm. Therefore, contrary to other approaches such as cellular automata, we are theoretically able to adjust the scale of the simulation and thus perform large-scale simulations.

The work in this thesis has given rise to several publications

- Stefan Marconi and Bastien Chopard, *Modelling the Navier equation with a Lattice Boltzmann Model*, in preparation.

- Stefan Marconi and Bastien Chopard, *A Lattice Boltzmann Model of a Solid Body*, 153-156, 17(1-2), IJMP B.

- Bastien Chopard and Stefan Marconi, *A lattice boltzmann wave model applied to fracture phenomena*, 14th Int, Symposium of Mathematical theory of network and systems, 2000, University of Perpigan, France.

- Stefan Marconi, Bastien Chopard and Jonas, *Reducing the compressibility of a lattice boltzmann fluid using a repulsive force*, IJMP C, 2003.

- Bastien Chopard and Stefan Marconi, *Lattice boltzmann solid particles in a lattice boltzmann fluid*, Journal of Statistical Physics, 107(1/2):23–37, April 2002.

- Stefan Marconi and Bastien Chopard, *A multiparticle lattice gas automata model for a crowd*, In Stefania Bandini, Bastien Chopard, and Marco Tomassini, editors, Cellular Automata, number 2493 in LNCS, pages 231–238. Springer, 2002.

Chapter 2

Solid modelling

2.1 Introduction

The aim of this chapter is to promote the development of a lattice Boltzmann model for the dynamics of a solid body. Although the lattice Boltzmann method has in the last decade successfully been used to model fluid dynamics through the modelling of the Navier-Stokes equation, little interest has been shown towards establishing a similar model for the dynamics of solids. This lack of interest is probably due to the fact that the many theoretical challenges and potential applications offered by solids dynamics are less known than the ones offered by fluid dynamics. Nevertheless, such challenges do exist. The modelling of the contact of a car tire on the road is an example both of theoretical and practical difficulties. No doubt that, as for fluids dynamics, the vast and complex area of research of solid dynamics is in the need of a simple, intuitive and very efficient algorithm such as the lattice Boltzmann model can potentially offer.

To better understand the theoretical challenge of solid dynamics modelling, we must first realise that it is commonly divided into two classes of problems: the motion of a solid and the deformation of the solid. The motion of a solid can be further decomposed into the motion of the center of mass and the rotation of the solid around its center of mass. The deformation of a solid is described with the linear theory of elasticity to which one can add the difficult problem of contact conditions. Except for the latter, these problems are individually the subject of study of undergraduate courses in physics. In our modelling therefore, the first difficulty arises from the fact that all these are macroscopic theories and that the lattice Boltzmann model will have to be based on a microscopic description. The second difficulty is that on a macroscopic scale it is usual to decouple motion and deformation. At a microscopic level, however, there always is a combination of both. The general and complete modelling of solid dynamics, however simple each separate aspect may be, is therefore a difficult problem as will be illustrated in this chapter.

Leaving aside the complete theory of solid dynamics, a cornerstone in the modelling is to establish a model for the Navier equation of motion which is the linear elasticity equivalent to the Navier-Stokes equation for fluid dynamics. Less known than the Navier-Stokes equation, the complexity arising from the Navier equation is shaded by the fact that it is a linear equation and can be decomposed into wave equations. In fact, the complexity of the problem resides in the border conditions where the waves can interact and which themselves can be subject to dynamical changes. The process of dynamical fracture is the most prominent example of theoretical and practical complexity to be found in the Navier equation. A successful modelling of the Navier equation, as any steps towards it, would therefore give deep insights into complex physical problems.

The chapter is organized as follow. First, the theory of linear elasticity is introduced as it is the main object of our modelling. Examples of difficulties arising in modelling the solid dynamics are then given to illustrate the diversity of approaches and the complexity of the domain. Then, a lattice Boltzmann model is presented. We start with a cellular automata model which gives a good intuitive understanding of the mechanisms at work and then move forward with a lattice Boltzmann wave model applied to the dynamics of a solid. Finally we end with the latest developments concerning a lattice Boltzmann to directly model the Navier equation of linear elasticity. The conclusion will put in perspective the limits and the future developments of the model.

2.2 Theory

From point of view of classical physics, the dynamics of a solid body falls into two fields: mechanics and elasticity. The first is the study of the overall motion of a solid without deformation and includes translational and rotational motions. The second is concerned with the deformation of a body in the absence of global motion. Each field operates in distinct representation namely the Lagrangian one for mechanics and the Eulerian one for elasticity. The Eulerian representation deals with the value of a field such as displacement at a given point in space while the Lagrangian representation fixes the origin and describes the trajectory of particles in such a reference frame. Indeed, the Eulerian representation is often termed the material representation while the Lagrangian is named the spatial representation. In order for the mathematical description to be consistent, it is not possible to combine the two representations and this gives rise to limitations in the attempt at modelling the complete dynamic of solid body.

In the following section, we provide a brief overview of the theory of linear elasticity followed by examples of difficult problems to solve. Being part of any undergraduate course in physics, the notions relevant to kinematic theory are considered to be known to the reader. The best reference on the matter remains the series of Feynman Lectures on Physics [3]

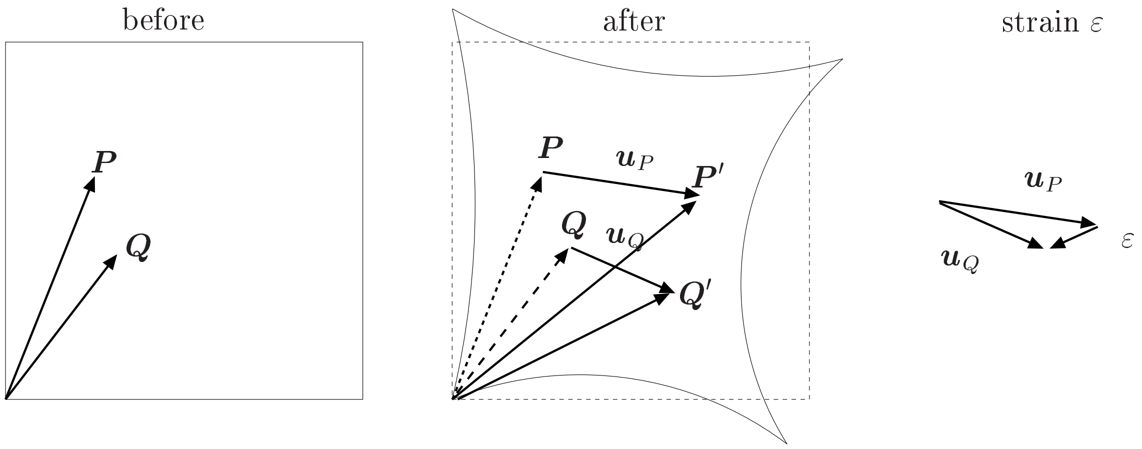

Figure 2.1: The definition of the strain-displacement relation. The strain ε is the function of x and y which gives the variation between point $\boldsymbol{P}$ and $\boldsymbol{Q}$ of the displacement $\boldsymbol{u}$ due to deformation of a solid.

2.2.1 The Navier equation of motion

In order to study the deformation of an elastic body, we first define the strain ε in the body as the tensor field which corresponds to the variation of displacement $\boldsymbol{u}$ in the body due to deformation, see figure 2.1,

$$\varepsilon_{ij} = \frac{1}{2}(\frac{\partial u_i}{\partial x_j} + \frac{\partial u_j}{\partial x_i}) \tag{2.1}$$

The strain is symmetric so as not to take into account rotations since these do not actually give rise to deformation. The strain of the solid arises from the stress σ applied to it. The most general relation $\sigma_{ij} = C_{ijkl}\varepsilon_{kl}$ between the strain and stress tensor is given by the elasticity tensor C_{ijkl} which is a rank four tensor with 81 components. Due to symmetry, isotropy and homogeneity, this relation simplifies to the well-known linear stress-strain relation for an elastic body

$$\sigma_{ij} = \lambda\varepsilon_{kk}\delta_{ij} + 2\mu\varepsilon_{ij} \tag{2.2}$$

where λ and μ are the Lamé coefficients. The momentum balance equation with external force $\boldsymbol{F}$ resulting from Newton's law is

$$\sum_j \frac{\partial\sigma_{ij}}{\partial x_j} + \rho F_i = \rho\ddot{u}_i \tag{2.3}$$

where the stress tensor is symmetric in order to satisfy the balance of angular momentum. The combination of equations (2.1), (2.3) and (2.2) yields the equation of motion in the elastic solid

$$(\lambda + \mu)\partial_{x_i}\partial_{x_j}u_j + \mu\partial_{x_j}^2 u_i + \rho F_i = \rho\ddot{u}_i \tag{2.4}$$

or equivalently

$$(\lambda + \mu)\nabla(\nabla \cdot \boldsymbol{u}) + \mu\nabla^2\boldsymbol{u} + \rho\boldsymbol{F} = \rho\ddot{\mathbf{u}} \tag{2.5}$$

known as the Navier equation. In the case of an unbounded infinite body, solutions to the Navier equation are obtained as follow. Using the vector identity

$$\nabla \times (\nabla \times \boldsymbol{u}) = \nabla(\nabla \cdot \boldsymbol{u}) - \nabla^2\boldsymbol{u} \tag{2.6}$$

the Navier equation can be written as

$$c_d^2\nabla(\nabla \cdot \boldsymbol{u}) - c_s^2\nabla \times (\nabla \times \boldsymbol{u}) + \boldsymbol{F} = \ddot{\mathbf{u}} \tag{2.7}$$

where

$$c_d^2 = \frac{\lambda + 2\mu}{\rho} \qquad \text{and} \qquad c_s^2 = \frac{\mu}{\rho} \tag{2.8}$$

Momentarily considering the body force $\boldsymbol{F}$ equal to zero, the application on this equation of, either the divergence operator $\nabla\cdot$ or the curl operator $\nabla\times$ and relation (2.6) again, yields two wave equations

$$\partial_t^2(\nabla \cdot \boldsymbol{u}) - c_d^2\nabla^2(\nabla \cdot \boldsymbol{u}) = 0 \tag{2.9}$$

$$\partial_t^2(\nabla \times \boldsymbol{u}) - c_s^2\nabla^2(\nabla \times \boldsymbol{u}) = 0 \tag{2.10}$$

where $\nabla \cdot \boldsymbol{u}$ and $\nabla \times \boldsymbol{u}$ are the dilation and the rotation vectors and c_d^2 and c_s^2 the respective sound speeds. The equation of motion can thus be decoupled into two waves, the dilatational wave and the shear wave. It is of the utmost importance to notice that this is true in the bulk of the solid, but that at boundaries the two waves will interact. This is the feature that accounts for most of the complication in solving the equation of motion. A complete discussion of plane wave reflection on boundaries can be found in [4]. The effect of dynamically varying borders however is an even more difficult problem, a discussion of which can be found in [5]. The integration of the equation of motion (2.4) however is greatly advantaged by the decomposition into wave equations since various means are available to solve these. A difficulty, though, consists in showing that this new representation is complete namely that is really does represent all the solutions of equation (2.4). A detailed discussion of such a proof is discussed in [6]. An example of a complete representation is given by the Lamé representation which uses the Helmholtz additive decomposition of a vector field. The displacement is now written as

$$\boldsymbol{u} = \nabla\phi + \nabla \times \boldsymbol{\psi} \tag{2.11}$$

where the scalar field ϕ and the vector field $\boldsymbol{\psi}$ both obey the wave equation as can directly be verified by replacing (2.11) into (2.9). In addition, the vector field must obey the following relation

$$\nabla \cdot \boldsymbol{\psi} = 0 \tag{2.12}$$

This last condition is one of the difficulties which arises when trying to numerically solve the vector wave equation since it couples all components of the vector field. It is therefore not possible to simply model three independent scalar waves for each component of the vector field $\boldsymbol{\psi}$.

2.2.2 Examples of difficult solid modelling.

The vast area of applications and existing numerical tools to model the dynamics of a solid is clearly to large to be completely presented here and the scope of the problem would be most probably be lost in the details of each method. Again, although our aim will be to model the Navier equation of motion, not all approaches start with the theory of linear elasticity. Our first example for instance belongs to the field of molecular dynamics. The examples below thus serve two purposes. First they provide a good illustration of problems which are usually simple to understand yet provide theoretical and numerical difficulties which limit early on any simulations. Second, they describe the problem on two different levels: the microscopical and macroscopic levels. The lattice Boltzmann approach, we believe, is a sound approach when wanting to reconcile both levels and this will be illustrated when later in this chapter we will put our model in practice to investigate the same two problems presented here.

Dynamic fracture

The subject of dynamic fracture is a very exciting problem, the theory of which remains full of very challenging problems simply because experiments are not in full agreement with theory [5]. One possible way to explore such phenomena consist in performing molecular dynamics simulations. The simulations in [7] study the dynamics of two dimensional system made of up to 10^6 atoms and the authors have, since then, also performed three dimensional simulations involving up to 10^9 atoms. In order to perform these simulations, one obviously needs powerful computers and indeed the authors have access to the most powerful computers. The counterpart of this computing power limitation is that the timescale which can be explored is limited to a few nanoseconds. Nonetheless, the clear advantages of performing molecular dynamics is that the complete physics is present in the simulation. Indeed, the simulations have allowed to shed light on previously unknown phenomena such as supersonic crack speeds [8].

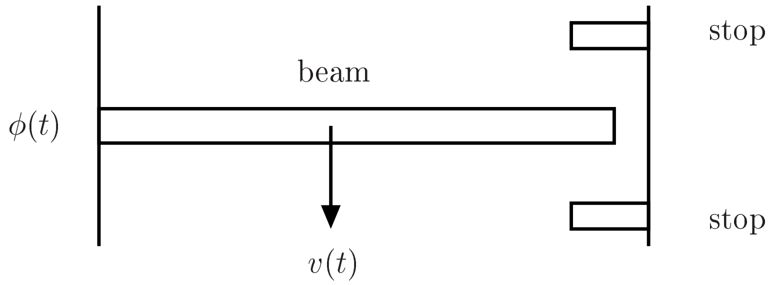

Figure 2.2: A model to study the vibrations characteristics of mechanical joints. The problem consists in studying the vertical displacement $v(t)$ of a beam which is excited by the force $\phi(t)$ at one end while the movement of the free end is constrained by two stops.

Contact

Problems of mechanical contact are to be found in a lot of very practical situations such as the brakes in a car or the contact of wheels during the landing of a plane. In order to illustrate the mathematical complexity behind these problems, we propose to describe qualitatively an example of a simple model for such processes. Even though the constitutive relations and equations are linear, these problems are nonlinear because of the contact conditions. Often, therefore, the mathematical result consists solely in a existence and uniqueness theorem of the solution to the equations describing the problem without explicitly giving any solutions.

The model we describe here aims at understanding the noise and vibrations characteristics of mechanical joints. It consists of a beam which may be excited at one end with a vertical force $\phi(t)$ while the other end is free to move within the space fixed by two stops. The setup is shown on figure 2.2. In the case of rigid stops, the contact between the beam and the stops consists in applying a stress opposite to the displacement when contact occurs. The equation of motion is more complicated than the Navier equation since the constitutive equation is that of a beam and not the simple case found in equation (2.2). The mathematical analysis of this system can be found in [9]. The main result is that there exists an unique function $v(t)$ giving the vertical displacement of the beam. Properties of the function $v(t)$ shows that the system may have chaotic behavior and numerical simulations are needed to fully study the system.

2.3 The basic cellular automata model.

We present here two cellular automata models. The first is a slightly modified version of the original cellular automata for a large-scale moving object [10]. In the same spirit, the second model is an attempt at modelling a rotating object.

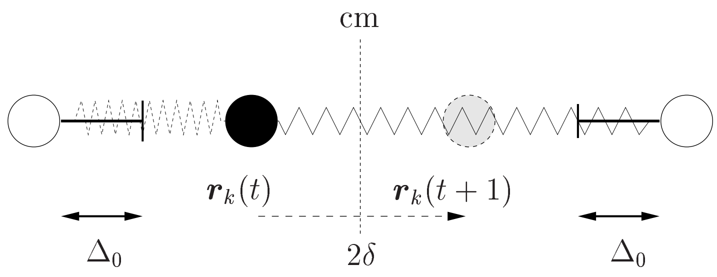

Figure 2.3: A three particle string illustrating the one dimensional cellular automata rule. White particle do not move between time steps t and $t+1$. The black particle at position $\boldsymbol{r}_k$ jumps a distance $2\boldsymbol{\delta}$ over the geometrical center of mass of the neighboring particles.

The former model although based on very simple and intuitive physical assumptions exhibits most of the complexity of subsequent models presented later in this chapter while the latter constitutes only the mere beginning at modelling the dynamics of rotations with an automata. The basic ingredients of the automata are the connection of particles with either springs in the first model or torsion bars in the second model. An ad-hoc rule then describes either the elongation or the rotation of elements connecting two particles. The motion resulting from this local rule should as a first step be able to keep the integrity of the solid. The second step consists in identifying physical quantities associated with the motion and showing that they obey proper conservation laws. As we shall see, the model for translation satisfies both requirements while in the present state, the rotation model is only able to partially keep integrity of the solid and there is no conservation of angular momentum.

2.3.1 Translational motion

The cellular automata model of a large-scale moving object consists of a D1Q2[1] lattice to model a chain or a D2Q4 lattice for a two dimensional object, both moving in either a 1d, 2d or 3d plane. The main achievement of this model is to have shown that it is possible to model an object whose size is larger than the range of the cellular automata rule while still conserving its size and integrity. Also it is possible to define adjustable mass, momentum and energy. The basic idea behind the automata is to achieve a discrete motion of particles connected by springs by only considering the two limiting states of a spring: full compression and full extension. Let first consider a one dimensional chain with three particles

[1]this notation due to Qian simply states the number of dimension D of the lattice topology and the number of connection Q between sites.

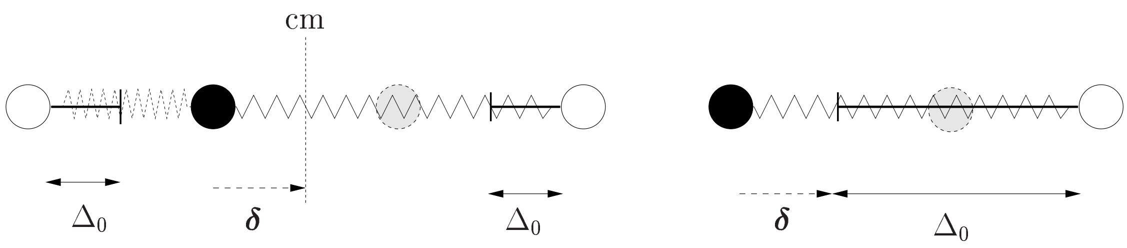

Figure 2.4: The position update rule of the 1d cellular automata illustrated with a black particles in the bulk (left) or on a border (right). The motion consists in a displacement of $2\boldsymbol{\delta}$ where $\boldsymbol{\delta}$ is defined slightly differently for each case. For a bulk particle $\boldsymbol{\delta}$ is the distance to the geometrical center of mass of the two neighbors. On the border, it is the distance to the tip of the spring as if it were at rest and connected to the neighbor.

as illustrated on figure 2.3. A particle in the bulk of the lattice (in this case the black particle) is considered to be linked to its two neighbors by springs with rest length Δ_0. Considering the neighbors to be fixed, should the particle not be in its rest position, one would expect it to have an harmonic-like motion with two symmetric limiting positions given by its initial displacement. The automata will therefore only model these two positions. Subsequently, by alternating the motion of black and white particles we obtain a caterpillar-like movement. With this picture in mind, the automata rule is as follow:

1. divide the chain into two sub-chains (black/white) in a checkerboard manner.
2. alternatively update all particles positions in each sub-chain.

The update rule for particle k in the chain simply is

$$\boldsymbol{r}_k(t+1) = \boldsymbol{r}_k(t) + 2\boldsymbol{\delta} \tag{2.13}$$

where $\boldsymbol{\delta}$ is the distance to the geometrical center of mass of the two neighbors, see figure 2.4 (left). For a particle at the border with only one neighbor, $\boldsymbol{\delta}$ is the distance to the tip of the spring as it were at rest and attached to the neighbor particle, see figure 2.4 (right). Again theses rules derives from the fact that the motion is reduced to the positions of a particle when the spring is either in full extension or full compression for a given initial displacement.

In order to render the connection to latter developments of the model more logical, it is useful to slightly transform the algebra of this cellular automata rule. It is in fact possible two have exactly the same rule for particles in the bulk and particles on borders by considering the following observation: the geometrical center of mass of the two neighbor of a bulk particle is identical to the geometrical

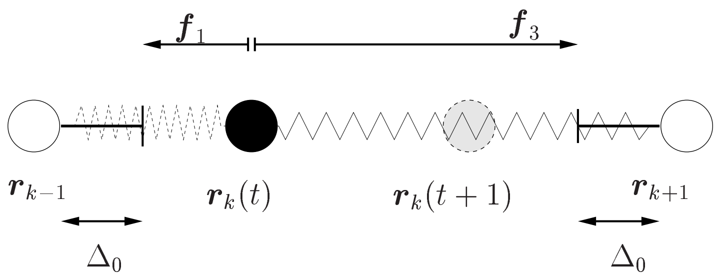

Figure 2.5: The definition of intermediary variables for the dynamics of the cellular automata. The vectors $\boldsymbol{f}_1$ and $\boldsymbol{f}_3$ are the distances of the black particle to the tip of the springs as if they were at rest and attached to the neighboring particles. In terms of these $\boldsymbol{f}$ fields, the dynamic of motion simply consists in exchanging $\boldsymbol{f}_1$ and $\boldsymbol{f}_3$.

center of mass of the springs as if they were at rest and attached to the neighboring particles. The rule given in equation (2.13) therefore does not change and the definition of $\boldsymbol{\delta}$ valid for any particles can now be written as

$$\boldsymbol{\delta} = \left(\frac{1}{K} \sum_{l \in \Omega_k} \tilde{\boldsymbol{r}}_l \right) - \boldsymbol{r}_k \tag{2.14}$$

where K is the number of neighbors of particle k, Ω_k is the neighborhood of particle k and

$$\tilde{\boldsymbol{r}}_l = \begin{cases} \boldsymbol{r}_l(t) + \Delta_0 & \text{for a left particle} \\ \boldsymbol{r}_l(t) - \Delta_0 & \text{for a right particle} \end{cases} \tag{2.15}$$

It is already noteworthy to say that with the above definition we have already chosen a fixed orientation of the chain. Indeed, the above definition mixes the choice of topology with the position update rule and thus doesn't take into account the possible changes of what might be a left and right particles. The consequence of this fact will remain throughout the modelling of the solid and the potential solutions to this fixed orientation problem should most probably be solved at this stage of the modelling. Nevertheless, for a one dimensional chain with no rotation the orientation is not expected to change.

In addition, for reasons which will also be clear with later models, it is useful to use in the dynamics the following intermediary variables defined as[2], see figure 2.5

[2]the reason for the non-consecutive labels $1, 3$ is to keep the consistency with the 2d model notation.

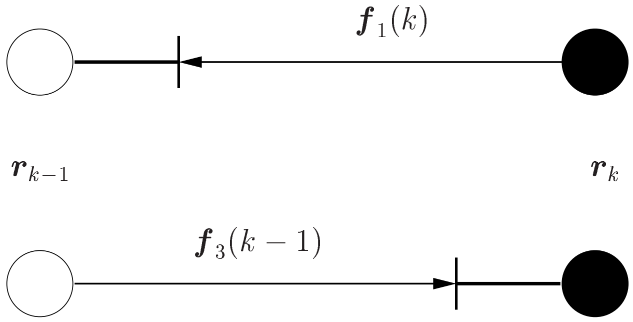

Figure 2.6: The dual relation between the $\boldsymbol{f}$ fields with regards of which particles is being considered. If the black particle is under consideration then the field $\boldsymbol{f}_1$ is defined. Alternatively, if the white particles is considered then it is $\boldsymbol{f}_3$. Therefore by writing that $\boldsymbol{f}_1(k) = -\boldsymbol{f}_3(k-1)$, we are simply stating that the distance between the two particles is the same for both points of view.

$$\boldsymbol{f}_1 = \boldsymbol{r}_{k-1} + \Delta_0 - \boldsymbol{r}_k \tag{2.16}$$

$$\boldsymbol{f}_3 = \boldsymbol{r}_{k+1} - \Delta_0 - \boldsymbol{r}_k \tag{2.17}$$

and their sum

$$\boldsymbol{\psi} = \sum_{i=1,3} \boldsymbol{f}_i \tag{2.18}$$

Thus equation (2.14) can be rewritten as

$$\boldsymbol{\delta} = \frac{1}{K} \sum_{l \in \Omega_k} \Big(\tilde{\boldsymbol{r}}_l - K\boldsymbol{r}_l(t) \Big) = \frac{1}{K} \sum_{i=1,3} \boldsymbol{f}_i = \frac{\boldsymbol{\psi}}{K} \tag{2.19}$$

and consequently equation (2.13) becomes

$$\boldsymbol{r}_k(t+1) = \boldsymbol{r}_k(t) + \frac{2}{K}\boldsymbol{\psi}(t) \tag{2.20}$$

By introducing these new variables, one can observe that the cellular automata rule for the motion a particle actually consists in exchanging $\boldsymbol{f}_1$ and $\boldsymbol{f}_3$ for particle k. This will also be referred to as the propagation of the fields $\boldsymbol{f}_1$ and $\boldsymbol{f}_3$. It is simply the consequence of the jump by the black particle over the center of mass of its two neighbors. We would now like to write the dynamic of motion in terms of these new $\boldsymbol{f}$ fields. Since the updating rule acts only in one sub-chain

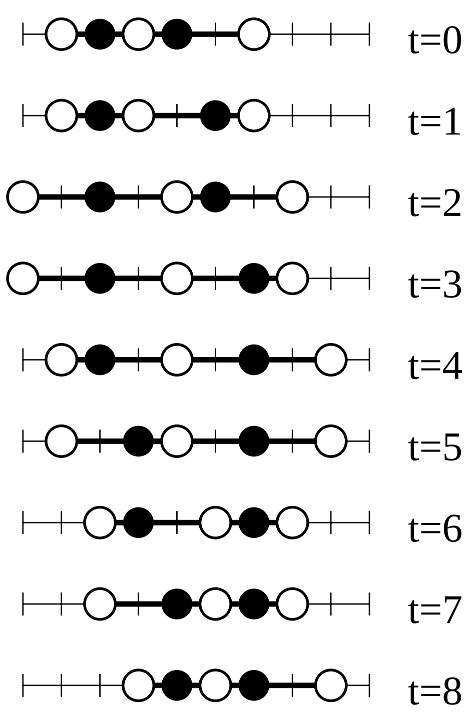

Figure 2.7: The motion of a one dimensional object using a cellular automata. This instance of the automata produce a motion in a discrete space. The overall motion is the result of the motion of each individual motion in a caterpillar-like way since the black and white particle are update alternatively. The speed of the chain can be calculated from the time and the distance it takes to return to the initial configuration, in this case 2/8.

at a time, the values of $\boldsymbol{f}_1$ and $\boldsymbol{f}_3$ after the motion of the black particle actually describe the state of the neighboring white particles for the following iteration, see figure 2.6. We can therefore write

$$\begin{aligned}\boldsymbol{f}_3(k-1,t+1) &= -\boldsymbol{f}_1(k,t+1) \\ &\overset{(2.16)}{=} -\left(\boldsymbol{r}_{k-1}(t+1)+\boldsymbol{r}_0-\boldsymbol{r}_k(t+1)\right) \\ &\overset{(2.13)}{=} -\left(\boldsymbol{r}_{k-1}(t+1)+\boldsymbol{r}_0-\boldsymbol{r}_k(t)-2\boldsymbol{\delta}\right) \\ &\overset{(2.19)}{=} \frac{2}{K}\boldsymbol{\psi}-\boldsymbol{f}_1(k,t)\end{aligned} \tag{2.21}$$

and symmetrically for $\boldsymbol{f}_1(k+1,t+1)$. We now have a dynamic for the motion in terms of the $\boldsymbol{f}$ instead of the positions $\boldsymbol{r}$. This form will enable us to directly generalize our model once the lattice Boltzmann model for a wave is presented

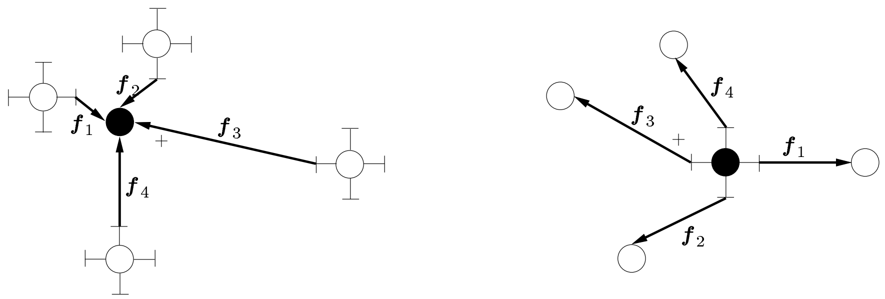

Figure 2.8: The 2d cellular automata rule illustrated for the black particle. The distance to the springs of the two extra particles are defined using the fields $\boldsymbol{f}_2$ and $\boldsymbol{f}_4$. The black particle jumps over the center of mass of the four neighboring springs.

in section 2.4. The motion produced by this automata for a chain placed in a discrete space, i.e. both $\boldsymbol{r}$ and Δ_0 are discrete, is shown on figure 2.7.

⋆ ⋆ ⋆

The simple one dimensional automata can easily be extended to a two dimensional version by using a D2Q4 lattice for representing the topology of the solid. The cellular automata rule remains the same: a checkerboard division of the lattice; alternatively white/black particle jumps over the center of mass of their four neighbors springs, see figure 2.8. The algebra developed above remains the same except for the definitions of two extra fields $\boldsymbol{f}_2$ and $\boldsymbol{f}_4$ for the new neighbors. In the bulk, it is possible to decouple the x and y axis movements of particles which thus leads to a very simple numerical scheme. Explicitly, $\boldsymbol{f} = (f_x, f_y)$ is now a vector with two separate dynamics for the x and y components. This choice, however, breaks the invariance under rotation for the motion of particles on the borders. Indeed, in this case, the update rule does not correspond to a jump over the center of mass of the neighbors anymore. This does provide a clear limitation when a complete dynamic of a solid is needed. For the moment however, we continue in the same line as the one dimensional automata by defining the $\boldsymbol{f}$ fields as

$$\boldsymbol{f}_1 = \boldsymbol{r}_{i-1,j} + \boldsymbol{\Delta}_{0x} - \boldsymbol{r}_{ij} \tag{2.22}$$
$$\boldsymbol{f}_3 = \boldsymbol{r}_{i+1,j} - \boldsymbol{\Delta}_{0x} - \boldsymbol{r}_{ij} \tag{2.23}$$
$$\boldsymbol{f}_2 = \boldsymbol{r}_{i,j-1} + \boldsymbol{\Delta}_{0y} - \boldsymbol{r}_{ij} \tag{2.24}$$
$$\boldsymbol{f}_4 = \boldsymbol{r}_{i,j+1} - \boldsymbol{\Delta}_{0y} - \boldsymbol{r}_{ij} \tag{2.25}$$

where $\boldsymbol{\Delta}_{0x} = (|\Delta_0|, 0)$ and $\boldsymbol{\Delta}_{0y} = (0, |\Delta_0|)$. Again, the definition of the $\boldsymbol{f}$ links the position and the orientation/topology of the object which is not a problem

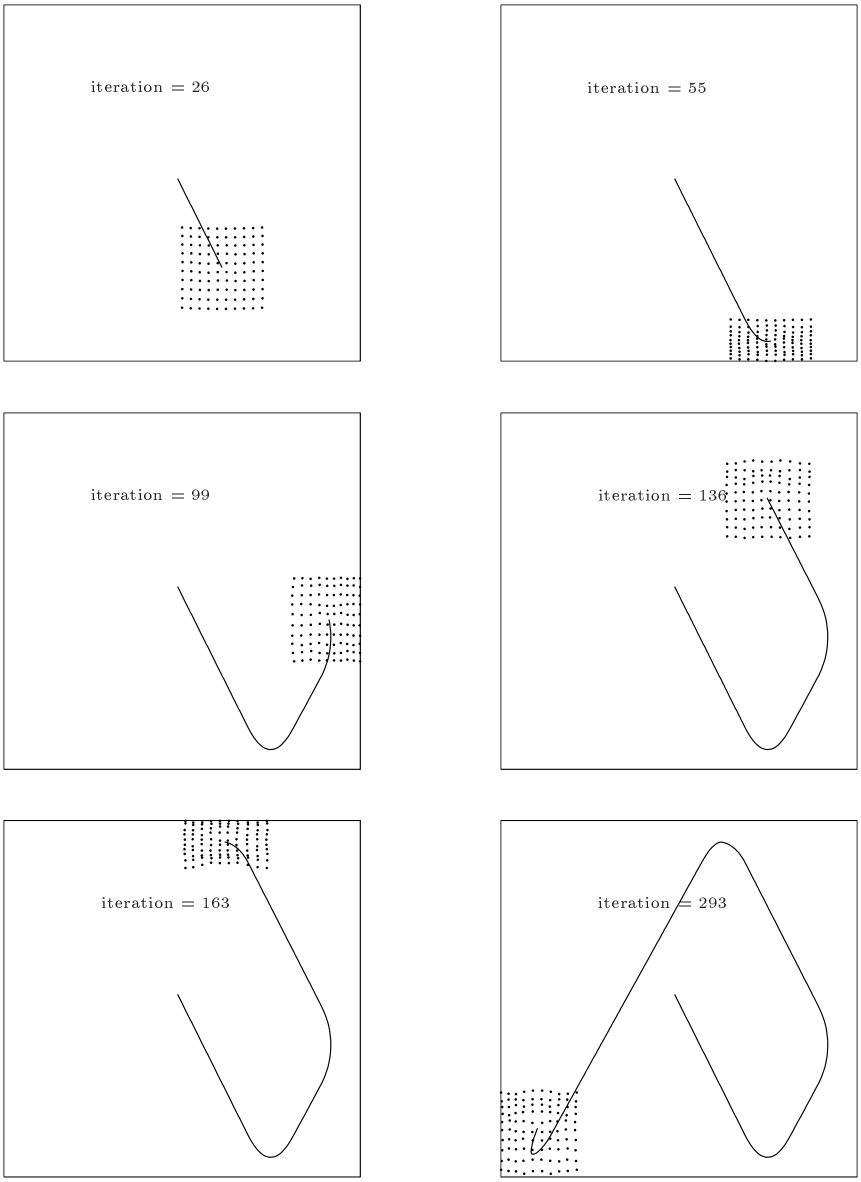

Figure 2.9: The motion of a two dimensional object using a cellular automata.

as long as rotations are not considered. The dynamics for the $\boldsymbol{f}$ can again be written as

$$\boldsymbol{f}_i(\boldsymbol{l} + \boldsymbol{c}_i, t+1) = \frac{2}{K}\boldsymbol{\psi} - f_{i+2}(\boldsymbol{l}, t) \tag{2.26}$$

where $\boldsymbol{l}$ is the position of a particle in the lattice and $\boldsymbol{c}_i$ is the unit vector pointing to the neighbor site in direction i. In a matrix form, the dynamics in the bulk can be written as

$$\begin{pmatrix} f_1(\boldsymbol{l}+\boldsymbol{c}_1, t+1) \\ f_2(\boldsymbol{l}+\boldsymbol{c}_2, t+1) \\ f_3(\boldsymbol{l}+\boldsymbol{c}_3, t+1) \\ f_4(\boldsymbol{l}+\boldsymbol{c}_4, t+1) \end{pmatrix} = \frac{1}{2} \begin{pmatrix} 1 & 1 & -1 & 1 \\ 1 & 1 & 1 & -1 \\ -1 & 1 & 1 & 1 \\ -1 & 1 & 1 & 1 \end{pmatrix} \begin{pmatrix} f_1(\boldsymbol{l}, t) \\ f_2(\boldsymbol{l}, t) \\ f_3(\boldsymbol{l}, t) \\ f_4(\boldsymbol{l}, t) \end{pmatrix} \tag{2.27}$$

This matrix formulation is exactly the form given in the transmission line matrix formalism(TLM) used to model the propagation of electromagnetic waves in a electrical circuit [11] [12]. This analogy will later be used in order to establish the lattice Boltzmann wave model for the solid. Examples of motion of a two dimensional objects are illustrated on figure 2.9. In order for the solid to bounce, any x or y motion over the boundary is simply forbidden. In the case of the $\boldsymbol{f}$ dynamics, the value of $\boldsymbol{f}$ are then simply recalculated with equations (2.22)-(2.25) to correspond to the position of the particle. In the lattice Boltzmann model presented further on, this bounce rule will be obtained through an external force acting on the solid.

Physical quantities can be associated with the automata. At a particle level, momentum $\boldsymbol{p}$ and mass M which can be deduced from equation (2.20) as

$$\boldsymbol{p} = \psi \qquad \text{and} \qquad m = \frac{K}{2} \tag{2.28}$$

On a macroscopic level, the whole solid has a momentum and mass given by

$$\boldsymbol{P} = \sum_k p_k \qquad \text{and} \qquad M = \sum_k m_k \tag{2.29}$$

which can be associated with the center of mass $\sum_k m_k \boldsymbol{r}_k / \sum_k m_k$ of the solid. The total energy E of the object of l particles is also defined as

$$E = \frac{1}{2} \sum_l \sum_i f_i^2 \tag{2.30}$$

and, in fact, the update rule can be derived from this expression with a discrete Hamiltonian formalism as presented in [10]. All the physical quantities can be shown to be conserved by the dynamics. This will be clearly shown in later models.

2.3.2 Rotational motion

The cellular automata presented above is an attempt at the global motion of a solid. However, we have seen that it is not designed to model rotational motions even though some particular one dimensional chains configuration do exhibit rotation-like motion, see [10]. To incorporate rotations in the same spirit of modelling, it is necessary to find a mechanism similar to that of the springs

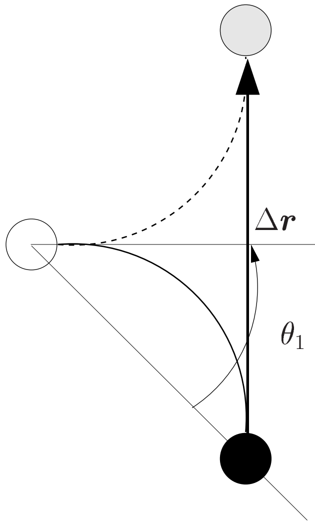

Figure 2.10: To model a rotation with a cellular automata, we connect particles with torsion bars. The state of the bar is then describe by an angle, θ_1 or θ_3, depending on the particles considered. The rotational motion of the particle is approximate by the vector $\Delta \boldsymbol{r}$ which joins the to symmetric positions of the torsion bar.

of the previous automata. We are therefore tempted to connect particles with torsion bars instead of springs and use the same black/white alternate motion. It is easy for one to imagine that the analogy is possible when particles have only one neighbors. On the other hand, it is not clear how to combine the torsion coming from two different neighbors. This difficulty is related to the fact that finite rotations with different rotation centers do not commute and this might constitute a severe theoretical limit to modelling a rotation from a microscopical point of view. Nevertheless, it is possible to construct a "toy" model which exhibit rotation-like motion and which can be numerically stable for well defined initial conditions. In the following model, no sensible physical quantity have been identified to correspond to inertia, angular momentum or energy. However, these quantities can be measured and although they might not be conserved microscopically, it may be possible that in the good limits, we recover the corresponding macroscopic quantities. In what follows, we limit ourselves to exhibiting the automata and its behavior.

The model is built in analogy to the one dimensional translational automata. Instead of having $\boldsymbol{f}_1$ and $\boldsymbol{f}_3$ relating to the elongation of the springs connecting adjacent particles, we now introduce the fields θ_1 and θ_3 as the angles of torsion between adjacent particles, see figure 2.10. In analogy to the previous automata, the rule for motion will then be constructed from a combination of these fields. Lets first consider at a two particle object. The rotation of the bar defines a rotation center. In the black/white alternance picture, this center of rotation can

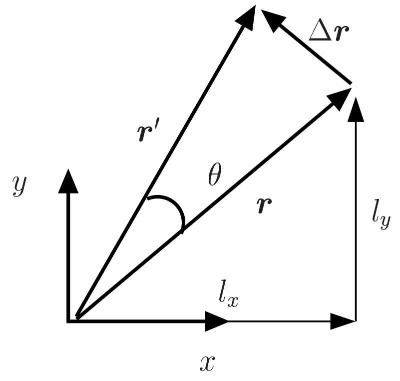

Figure 2.11: The elementary motions used in order to create a rotating object. In analogy to infinitesimal rotation, the arc of rotation is approximated by the vector joining the new and old positions. The total rotation is obtained by linearly adding the rotations in the x and y directions.

simply be chosen to be the neighbor particle. The trajectory of the torsion bar is approximated by the vector $\Delta \boldsymbol{r}$ joining the new and the old position of the particle at the end of the bar, see figure 2.10, which in the case of an infinitesimal angle is a good approximation. The most general case of rotation is shown on figure 2.11. The change in the horizontal extension l_x and vertical extension l_y of the bar is simply given by a rotation matrix with angle θ

$$\begin{pmatrix} \Delta l_x \\ \Delta l_y \end{pmatrix} = \begin{pmatrix} \cos\theta & \sin\theta \\ -\sin\theta & \cos\theta \end{pmatrix} \begin{pmatrix} l_x \\ l_y \end{pmatrix} \tag{2.31}$$

The displacements $(\Delta l_x, \Delta l_y)$ directly give the displacement of the particle at the end of the torsion bar. For a two particle system, this rule directly models the rotation th system as shown on figure 2.12 for various initial angles of displacements. Obviously the precision of the motion is directly proportional to the angle chosen.

The next step consist in generalizing the dynamics for a chain of arbitrary length. In order to combine the torsion arising from two different neighbor particles, we choose to simply average the motion given in equation (2.31) in the following way

$$\Delta l'_x = \frac{1}{K}(\Delta l_x^{\text{left}} + \Delta l_x^{\text{right}}) \tag{2.32}$$

$$\Delta l'_y = \frac{1}{K}(\Delta l_y^{\text{left}} + \Delta l_y^{\text{right}}) \tag{2.33}$$

where $K = 1, 2$ is the number of neighbors and $\Delta l_y^{\text{left}}, \Delta l_x^{\text{left}}$ and $\Delta l_x^{\text{right}}, \Delta l_y^{\text{right}}$ indicates the positions calculated with equations (2.31) respectively for the left or right neighbor particle alone. The resulting motion for different time steps is

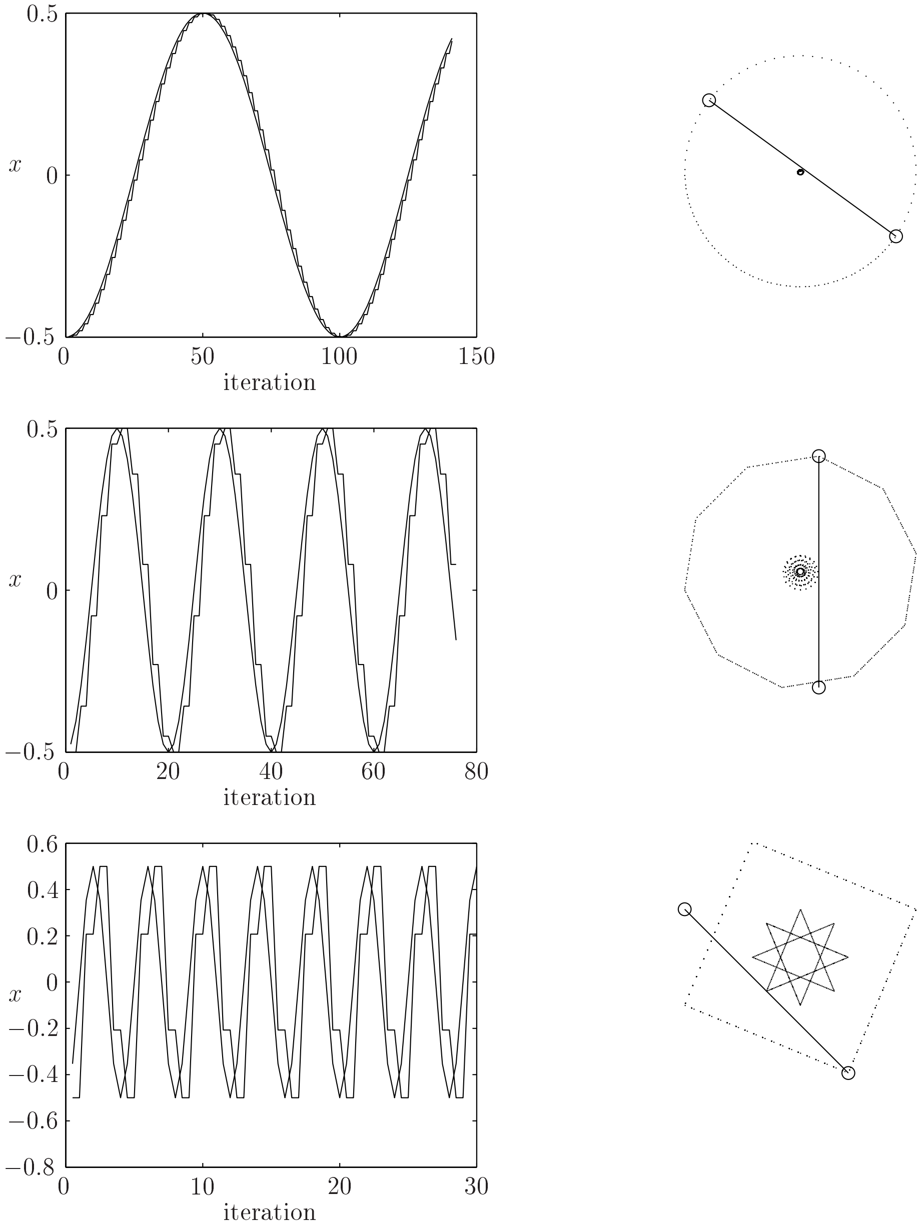

Figure 2.12: Three examples of rotations with initial displacements angles $\theta = \pi/50, \pi/10, \pi/4$. The left pictures are that of the x position of one particle during simulation plotted against the corresponding perfect circle trajectory. The right pictures are the trajectories of a particle (the outer line) and the center of mass of the two particles (the inner line).

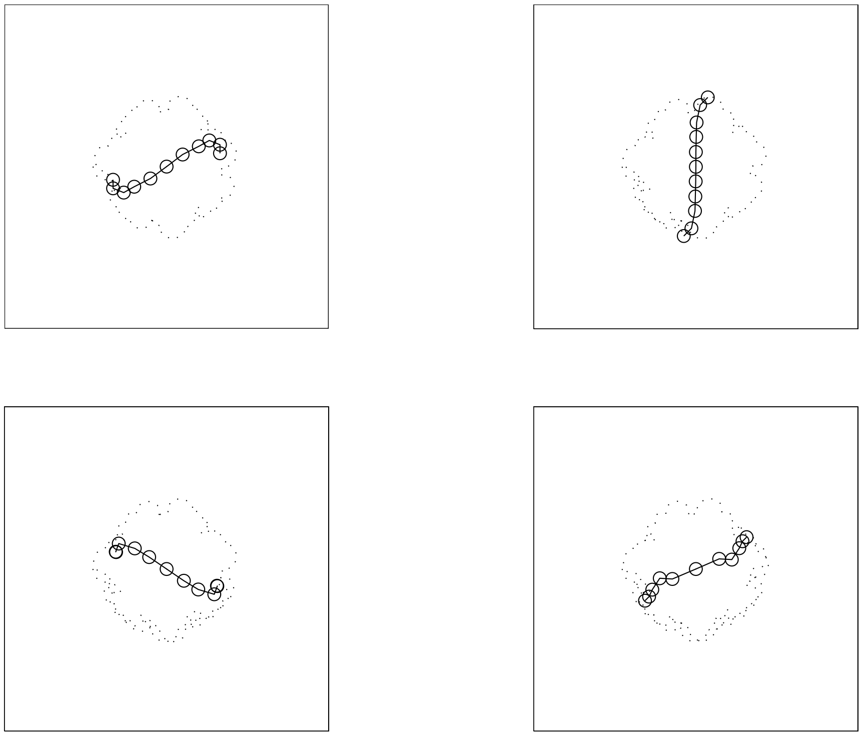

Figure 2.13: The rotation of a chain with 11 particles. The outer line is the trajectory of one of the border particles. Again while no physical quantity has clearly been identified, the scheme is remarkably stable and the chain keeps its integrity.

illustrated on figure 2.13 with a chain of 11 particles. The motion does conserve the integrity of the chain. However, no physical quantity has clearly been identified, though that fact that the scheme is numerically stable and the chain keeps its integrity is a strong indication that there is some quantity which is conserved even if only on average. The example given here is obtained with a constant angle at every lattice site. However, if we look at a system with only few particles in torsion, we observe that the resulting motion is similar to a spiral and the size of the chain diverges, see figure 2.14. On this pictures, both end particles received an initial kick. From this observation, we deduce that the distribution of angles in the chain must obey some criteria in order for the chain to keep its integrity. Identifying such criteria would in fact correspond to identifying the conservation law laying behind. This automata must therefore be considered as a collection of clues on how to model a microscopic rotation.

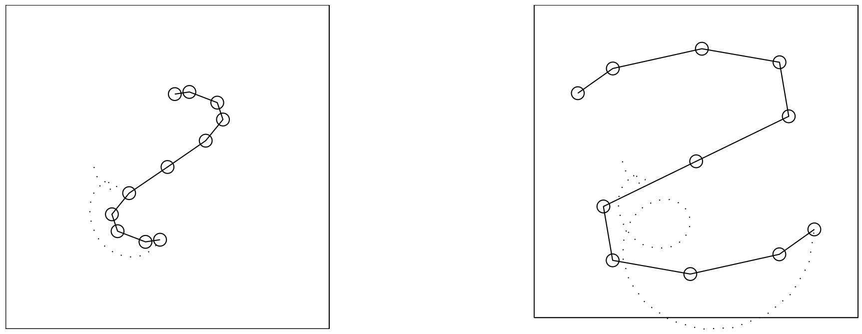

Figure 2.14: A spiraling chain resulting from a non uniform choice of angle θ in the chain. The size of the chain diverges which indicates that the angles chosen must obey some criteria in order to keep the integrity of the chain.

2.3.3 Conclusion

Through the two cellular automata presented in this section, we have seen the microscopic mechanisms at work in order to model the dynamics of a solid. These ideas will therefore guide us when trying to extend the model to a more physical situation. The limitations consisting of the mixture of Eulerian and Lagrangian representation and the lack of rotational motion will continue to plague the modelling and constitute clear challenges to be solved in an elegant and numerically efficient way. The following section will essentially present the extension of the cellular automata for translational motion rendered possible by the identification of the cellular automata with a wave model.

2.4 The scalar lattice Boltzmann model

Lattice Boltzmann models are the numerical implementation of the Boltzmann transport equation [13] with discrete space $\{\boldsymbol{r} + \boldsymbol{c}_i\}$ and time Δt

$$f_i(\boldsymbol{r} + \boldsymbol{c}_i \Delta r, t + \Delta t) - f_i(\boldsymbol{r}, t) = \Omega_i \tag{2.34}$$

where the vectors $\boldsymbol{c}_i$ are the lattice direction. In the fluid dynamics model which follows the statistical theory of transport, the f_i fields traditionally represent the density distributions of particles moving in direction i during the streaming phase with the direction $i = 0$ corresponding to the population of particles at rest. The exact interpretation of the f fields in the case of solid modelling will be discussed later on. The collision term Ω_i contains all information concerning the physical process. Since the space is discrete, the collision term is sometimes completely described, i.e. all the possible configuration of particles are explicitly taken into account, such as for the FHP models [14]. Another popular approach, the so-called Bhatnagar-Gross-Krook or BGK- model[15], consist in replacing the collision term by a relaxation to a local equilibrium

$$f_i(\boldsymbol{r} + \boldsymbol{c}_i \Delta r, t + \Delta t) - f_i(\boldsymbol{r}, t) = \frac{1}{\tau}\left(f_i^{(0)}(\boldsymbol{r}, t) - f_i(\boldsymbol{r}, t)\right) \tag{2.35}$$

where τ is the relaxation time. All the information concerning the physical process is thus contained in the local equilibrium. In order to model a wave [14], the choice for the local equilibrium is a linear form

$$f_i^{(0)} = a\psi + b\boldsymbol{c}_i \cdot \boldsymbol{J} \quad \text{for} \quad i > 0 \qquad \text{and} \quad f_0^{(0)} = a_0\psi \tag{2.36}$$

where

$$\psi = \sum_{i \geq 0} m_i f_i \qquad \text{and} \qquad \boldsymbol{J} = \sum_{i > 0} m_i f_i \boldsymbol{c}_i \tag{2.37}$$

are a scalar and its associated current, the conserved quantities of the dynamics. The values of the parameters a, a_0 and b are chosen such as to conserve ψ and $\boldsymbol{J}$. For isotropy reasons, the values of the m_i are constrained by the shape of the lattice and are thus named lattice weights.

In order to derive the macroscopic behavior at a scale where $T \gg \Delta_t$ and Ł $\gg \Delta_r$ from microscopical dynamics, it is common to use the Chapman-Enskog multi-scale expansion [14]. With our choice for the local equilibrium and the particular value of $\tau = 1/2$, this expansion leads to the following macroscopic equations for ψ and $\boldsymbol{J}$

$$\partial_t \psi + \partial_\beta \boldsymbol{J}_\beta = 0 \tag{2.38}$$

$$\partial_t \boldsymbol{J}_\alpha + c_s^2 \partial_\alpha \psi = 0 \tag{2.39}$$

By combining these two equations, we obtain the wave equation

$$\partial_t^2 \psi - c_s^2 \nabla^2 \psi = 0 \tag{2.40}$$

The sound speed c_s is given by

$$c_s^2 = aC_2 \tag{2.41}$$

where the coefficient C_2 is defined as

$$\sum_i m_i c_{i\alpha} c_{i\beta} = C_2 \delta_{\alpha\beta} \tag{2.42}$$

The choice for $\tau = 1/2$ is twofold. First, it suppresses viscous terms and unwanted anisotropic terms due to the lattice which appear during the Chapman-Enskog derivation. Second and foremost, it is required in order to obtain time reversal invariance as can be check in equation (2.36) with $\boldsymbol{J} \to -\boldsymbol{J}$ and $\psi \to \psi$.

Note that in hydrodynamics, the limit $\tau = 1/2$ corresponds to zero viscosity and is known to be numerically unstable. We thus impose that the dynamics (2.35) be unitary in order to have a numerically stable scheme. Indeed, ψ may be conserved with diverging values of f_i since these may as well be positive or negative. The unitary condition thus ensures the f_i will not diverge since it translates in the conservation of a quadratic form

$$E = \gamma f_0^2 + \sum_{i>0} f_i^2 \tag{2.43}$$

where $\gamma > 0$ is a function of the parameters a, a_0 and b and the lattice weights m_i.

The simplest choice of the lattice for the wave model is a D2Q5 lattice namely a square lattice with rest field. In this case, all the spatial weights $m_{i\neq 0}$ are equal and set to 1 without loss of generality. The condition of unitarity (2.43) leads to the value

$$\gamma = \frac{a}{a_0} m_0 \tag{2.44}$$

while the conservation of ψ and $\boldsymbol{J}$ respectively lead to

$$aC_0 + m_0 a_0 = 1 \qquad \text{and} \qquad b = \frac{1}{C_2} \tag{2.45}$$

where $C_0 = \sum_{i>0} m_i$. At this point, we are left with three parameters a, a_0, m_0 and one equation. We are therefore allowed to arbitrarily fix the value of one of these parameters. Previous wave models [14] have thus chosen $m_0 = 1$. We will here choose

$$a_0 = a m_0 \qquad \text{namely} \qquad \gamma = 1 \tag{2.46}$$

The dynamics (2.35) can now be written as

$$f_i(\boldsymbol{r} + \boldsymbol{c}_i \Delta r, t + \Delta t) = 2a\boldsymbol{\psi} - f_{i+2}(\boldsymbol{r}, t) \tag{2.47}$$

$$f_0(\boldsymbol{r}, t + \Delta t) = 2a m_0 \boldsymbol{\psi} - f_0(\boldsymbol{r}, t) \tag{2.48}$$

which is to be put in direct relation with the dynamics of the cellular automata given in equation (2.26). The speed of sound is therefore

$$c_s^2 = \frac{C_2}{C_0 + m_0^2} \tag{2.49}$$

which is always positively defined and whose maximum value $c_{max}^2 = C_2/C_0$ is obtained when $m_0 = 0$. It is thus possible to define a refraction index c_{max}/c_s as

$$n = \sqrt{\frac{m_0^2 + C_0}{C_0}} \tag{2.50}$$

Given that for a D2Q5, $C_2 = 2$ and that for a bulk site $C_0 = 4$, the maximum value for the sound speed is $c_{max} = 1/\sqrt{2}$. This value is lower than 1, the speed at which information travels in the lattice.

2.4.1 Solid Dynamics

In analogy to the cellular automata model presented in section 2.3, in order to model the evolution of displacements in a solid, we first transform the scalar density distributions f_i into vectors $\boldsymbol{f}_i = (f_{ix}, f_{iy})$ where each component independently obeys the wave equation. Therefore, $\boldsymbol{\psi}$ is now a vector with two components, and such was already the case in the cellular automata model, and $J_{\alpha\beta}$ a tensor. For reasons which will become clear below, we introduce the following change of notation

$$\frac{1}{2M} \equiv a \qquad \text{and} \qquad K \equiv C_0 \qquad \text{and} \qquad M_0 \equiv m_0 \tag{2.51}$$

with the choice of equation (2.46). By labelling lattice sites with an index $\boldsymbol{\ell}$, the dynamics (2.47) (2.48) at site $\boldsymbol{\ell}$ can be written as

$$\boldsymbol{f}_i(\boldsymbol{\ell} + \boldsymbol{c}_i, t + \Delta t) = M^{-1}(\boldsymbol{\ell})\boldsymbol{\psi}_{\boldsymbol{\ell}}(t) - \boldsymbol{f}_{i+2}(\boldsymbol{\ell}, t) + M^{-1}(\boldsymbol{\ell})\frac{\boldsymbol{F}(\boldsymbol{\ell}, t)}{2} \tag{2.52}$$

$$\boldsymbol{f}_0(\boldsymbol{\ell}, t + \Delta t) = M_0(\boldsymbol{\ell})M^{-1}(\boldsymbol{\ell})\boldsymbol{\psi}(\boldsymbol{\ell}, t) - \boldsymbol{f}_0(\boldsymbol{\ell}, t) + M_0(\boldsymbol{\ell})M^{-1}(\boldsymbol{\ell})\frac{\boldsymbol{F}(\boldsymbol{\ell}, t)}{2} \tag{2.53}$$

with

$$M = \frac{1}{2}(M_0^2 + K) \tag{2.54}$$

and K is the number of neighbors of the lattice site. The dynamics is therefore also completely defined for border sites. The extra term in $\boldsymbol{F}(\boldsymbol{\ell}, t)$ simply results from the adjunction of a constant term $\boldsymbol{F}$ in equation (2.35). The interpretation of this quantity will follow below. Lets note that since the $\boldsymbol{f}_i$ are vectors, the most general expression for M_0 and hence M is a matrix which is in theory able to couple the x and y components of $\boldsymbol{f}_i$. We will not make use of this possibility although constraints on M_0 will appear when the conservation of energy is rederived. We now use this wave equation to model the evolution of displacements in a body. The actual position of each particle of our solid is then given by the following rule

$$\boldsymbol{r}(\boldsymbol{\ell}, t + \Delta t) = \boldsymbol{r}(\boldsymbol{\ell}, t) + M^{-1}(\boldsymbol{\ell})\boldsymbol{\psi}(\boldsymbol{\ell}, t)\Delta t + M^{-1}(\boldsymbol{\ell})\frac{\boldsymbol{F}(\boldsymbol{\ell}, t)}{2}\Delta t^2 \tag{2.55}$$

which corresponds to a discrete update rule for a particle with mass M, momentum Ψ and external force $\boldsymbol{F}$. This interpretation for M, $\boldsymbol{\psi}$ and $\boldsymbol{F}$ will be justified once we will have shown the conservation of $\boldsymbol{\psi}$ and the conservation energy. At this point it is very important to understand the difference between the lattice site $\boldsymbol{\ell}$ and the position $\boldsymbol{r}$ of the particle it represents. The lattice represents the information on the topological connection between particles in the solid while the actual positions of particles in continuous space are given by $\boldsymbol{r}$.

In the following sections, the $^{\text{out}}$ index corresponds to a value after collision but before the streaming process.

2.4.2 Conservation of Momentum

Lets compute the value of $\boldsymbol{\psi}$ after collision using (2.37) (2.52) and (2.53)

$$
\begin{aligned}
\boldsymbol{\psi}^{\text{out}} &= M_0 \boldsymbol{f}_0^{\text{out}} + \sum_{i>0} \boldsymbol{f}_i^{\text{out}} && (2.56)\\
&= M_0^2 M^{-1} \boldsymbol{\psi}^{\text{in}} - M_0 \boldsymbol{f}_0^{\text{in}} + M_0^2 M^{-1} \frac{\boldsymbol{F}}{2} && (2.57)\\
&\quad + K M^{-1} \boldsymbol{\psi}^{\text{in}} + (-\boldsymbol{\psi}^{\text{in}} + M_0 \boldsymbol{f}_0^{\text{in}}) + K M^{-1} \frac{\boldsymbol{F}}{2} && (2.58)\\
&= (M_0^2 + K) M^{-1} \boldsymbol{\psi}^{\text{in}} - \boldsymbol{\psi}^{\text{in}} + (M_0^2 + K) M^{-1} \frac{\boldsymbol{F}}{2} && (2.59)
\end{aligned}
$$

which can be simplified with equation (2.54). We therefore end up with

$$
\begin{aligned}
\boldsymbol{\psi}^{\text{out}} &= 2\boldsymbol{\psi}^{\text{in}} - \boldsymbol{\psi}^{\text{in}} + \boldsymbol{F} && (2.60)\\
&= \boldsymbol{\psi}^{\text{in}} + \boldsymbol{F} && (2.61)
\end{aligned}
$$

The variation of $\boldsymbol{\psi}$ during collision is the body force $\boldsymbol{F}$. Thus, $\boldsymbol{\psi}$ is naturally identified with the momentum of a particle. An important property of this conservation law is that it is true for an arbitrary set of neighbors of a lattice site. Indeed, these are taken into account with the value of M as can be seen in equation (2.54). In this respect, it worth saying that in traditional lattice Boltzmann models, the conserved quantities of the dynamics are not conserved on the borders which usually require a special attention.

2.4.3 Conservation of energy and work

Lets first define

$$
\boldsymbol{\Phi} = \boldsymbol{\psi} + \frac{\boldsymbol{F}}{2} \qquad (2.62)
$$

Now

$$\begin{aligned}
E^{\text{out}} &= \sum_{i\geq 0}\left(\boldsymbol{f}_i^{out}\right)^2 && (2.63)\\
&= \left(M_0 M^{-1}(\boldsymbol{\psi}+\frac{\boldsymbol{F}}{2})-\boldsymbol{f}_0\right)^2+\sum_{i>0}\left(M^{-1}(\boldsymbol{\psi}+\frac{\boldsymbol{F}}{2})-\boldsymbol{f}_{i+2}\right)^2 && (2.64)\\
&= \left(M_0 M^{-1}\boldsymbol{\Phi}-\boldsymbol{f}_0\right)^2+\sum_{i>0}\left(M^{-1}\boldsymbol{\Phi}-\boldsymbol{f}_{i+2}\right)^2 && (2.65)\\
&= (M_0 M^{-1}\boldsymbol{\Phi})^T(M_0 M^{-1}\boldsymbol{\Phi})-2(M_0 M^{-1}\boldsymbol{\Phi})^T\boldsymbol{f}_0+\boldsymbol{f}_0^2 && (2.66)\\
&\quad +K(M^{-1}\boldsymbol{\Phi})^T(M^{-1}\boldsymbol{\Phi})-2\sum_{i>0}(M^{-1}\boldsymbol{\Phi})^T f_{i+2}+\sum_{i>0}\boldsymbol{f}_{i+2}^2 && (2.67)\\
&= \boldsymbol{\Phi}^T M^{-1}\left[M_0^T M_0 M^{-1}+KM^{-1}-2\right]\boldsymbol{\Phi}-2(M_0 M^{-1}\boldsymbol{\Phi})^T f_0 && (2.68)\\
&\quad +2(M^{-1}\boldsymbol{\Phi})^T M_0 f_0+2(M^{-1}\boldsymbol{\Phi})^T\frac{F}{2}+\sum_{i\geq 0} f_i^2 && (2.69)
\end{aligned}$$

where the subscript ^{T} designate the matrix transpose operation. Also, we have used that

$$\sum_{i>0}(M^{-1}\boldsymbol{\Phi})^T\boldsymbol{f}_{i+2}=(M^{-1}\boldsymbol{\Phi})^T\sum_{i>0}\boldsymbol{f}_{i+2}=(M^{-1}\boldsymbol{\Phi})\left(\boldsymbol{\Phi}-\frac{F}{2}-M_0\boldsymbol{f}_0\right) \quad (2.70)$$

Let us now consider the quadratic term in $\boldsymbol{\Phi}$. It reads

$$\boldsymbol{\Phi}^T\left(M^{(-1)}\right)^T\left[M_0^T M_0 M^{-1}+KM^{-1}-2\right]\boldsymbol{\Phi}=\boldsymbol{\Phi}^T\left(M_{(-1)}\right)^T\left[(M_0^T M_0+K)M^{-1}-2\right]\boldsymbol{\Phi}=0 \quad (2.71)$$

because, from (2.54), one has $M_0^T M_0+K=2M$, provided that M_0 is **symmetric**, i.e.

$$M_0^T M_0 = M_0^2 \quad (2.72)$$

Also, when $M_0^T=M_0$, two terms $(M_0 M^{-1}\boldsymbol{\psi})^T\boldsymbol{f}_0$ and $(M^{-1}\boldsymbol{\psi})^T M_0\boldsymbol{f}_0$ cancel. We are therefore left with

$$\begin{aligned}
E^{\text{out}} &= E^{\text{in}}+2\Phi^T M^{-1}\frac{F}{2} && (2.73)\\
& E^{\text{in}}+2(\boldsymbol{\psi}+\frac{F}{2})^T M^{-1^T}\frac{F}{2} && (2.74)\\
& E^{\text{in}}+2(M^{-1}\boldsymbol{\psi})^T\frac{F}{2}+2(M^{-1}\frac{F}{2})^T\frac{F}{2} && (2.75)\\
& E^{\text{in}}+(M^{-1}\boldsymbol{\psi}+M^{-1}\frac{F}{2})^T\cdot F && (2.76)\\
& E^{\text{in}}+(\boldsymbol{r}_{\boldsymbol{\ell}}(t+\tau)-\boldsymbol{r}_{\boldsymbol{\ell}})\cdot F && (2.77)
\end{aligned}$$

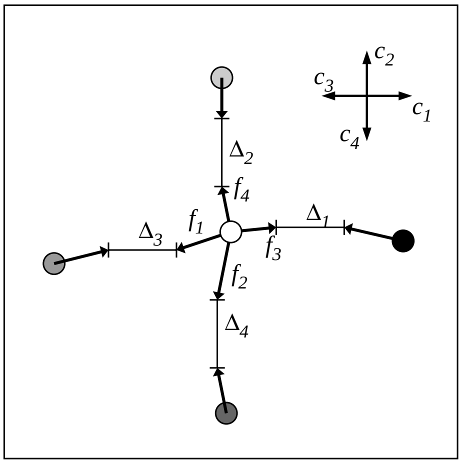

Figure 2.15: A particle, its four neighbors, the $\boldsymbol{f}_i$ fields and the rest lengths Δ_i between particles used in the dynamics of our model.

where we have used the definition of motion in equation (2.55). We can therefore conclude that the variation of E is given by the work done by the body force and thus we identify E with the total energy of a particle. The only constraint is that M_0 be a symmetric matrix.

2.4.4 Hooke's law

We now look at the relation between the f_i and the position of particles. From evolution rule (2.52)

$$\boldsymbol{f}_i(\boldsymbol{\ell}+\boldsymbol{c}_i, t+\tau) = M_{\boldsymbol{\ell}}^{-1}\boldsymbol{\psi}_{\boldsymbol{\ell}}(t) - \boldsymbol{f}_{i+2}(\boldsymbol{\ell}, t) + M_{\boldsymbol{\ell}}^{-1}\frac{1}{2}\boldsymbol{F}_{\boldsymbol{\ell}}(t) \tag{2.78}$$

one obtains, for $t \to t-\tau$

$$M_{\ell}^{-1}\boldsymbol{\psi}_{\boldsymbol{\ell}}(t-\tau) = \boldsymbol{f}_i(\boldsymbol{\ell}+\boldsymbol{c}_i, t) + \boldsymbol{f}_{i+2}(\boldsymbol{\ell}, t-\tau) - M_{\boldsymbol{\ell}}^{-1}\frac{1}{2}\boldsymbol{F}_{\boldsymbol{\ell}}(t-\tau) \tag{2.79}$$

and, also, for $\boldsymbol{\ell} \to \boldsymbol{\ell}+\boldsymbol{c}_i$, $i \to i+2$, $t \to t-\tau$

$$M_{\boldsymbol{\ell}+\boldsymbol{c}_i}^{-1}\boldsymbol{\psi}_{\boldsymbol{\ell}+\boldsymbol{c}_i}(t-\tau) = \boldsymbol{f}_{i+2}(\boldsymbol{\ell}, t) + \boldsymbol{f}_i(\boldsymbol{\ell}+\boldsymbol{c}_i, t-\tau) - M_{\boldsymbol{\ell}}^{-1}\frac{1}{2}\boldsymbol{F}_{\boldsymbol{\ell}+\boldsymbol{c}_i}(t-\tau) \tag{2.80}$$

On the other hand, from dynamic of motion of the a particle

$$\boldsymbol{r}_{\boldsymbol{\ell}}(t+\tau) = \boldsymbol{r}_{\boldsymbol{\ell}}(t) + M_{\boldsymbol{\ell}}^{-1}\Psi_{\ell}(t) + M_{\boldsymbol{\ell}}^{-1}\frac{\boldsymbol{F}_{\boldsymbol{\ell}}(t)}{2} \tag{2.81}$$

the separation between two adjacent particles $\boldsymbol{\ell}$ and $\boldsymbol{\ell}+\boldsymbol{c}_i$ is given by

$$\begin{aligned}\boldsymbol{r}_{\boldsymbol{\ell}+\boldsymbol{c}_i}(t)-\boldsymbol{r}_{\boldsymbol{\ell}}(t) &= \boldsymbol{r}_{\boldsymbol{\ell}+\boldsymbol{c}_i}(t-\tau)-\boldsymbol{r}_{\boldsymbol{\ell}}(t-\tau)\\ &\quad +M^{-1}_{\boldsymbol{\ell}+\boldsymbol{c}_i}\boldsymbol{\psi}_{\boldsymbol{\ell}+\boldsymbol{c}_i}(t-\tau)+M^{-1}_{\boldsymbol{\ell}}\frac{1}{2}\boldsymbol{F}_{\boldsymbol{\ell}+\boldsymbol{c}_i}(t-\tau)\\ &\quad -M^{-1}_{\boldsymbol{\ell}}\boldsymbol{\psi}_{\boldsymbol{\ell}}(t-\tau)-M^{-1}_{\boldsymbol{\ell}}\frac{1}{2}\boldsymbol{F}_{\boldsymbol{\ell}}(t-\tau)\end{aligned}\tag{2.82}$$

Using (2.79) and (2.80), we then obtain

$$\begin{aligned}\boldsymbol{r}_{\boldsymbol{\ell}+1}(t)-\boldsymbol{r}_{\boldsymbol{\ell}}(t) &= \boldsymbol{r}_{\boldsymbol{\ell}+\boldsymbol{c}_i}(t-\tau)-\boldsymbol{r}_{\boldsymbol{\ell}}(t-\tau)\\ &\quad +\boldsymbol{f}_{i+2}(\boldsymbol{\ell},t)+\boldsymbol{f}_i(\boldsymbol{\ell}+\boldsymbol{c}_i,t-\tau)\\ &\quad -\boldsymbol{f}_i(\boldsymbol{\ell}+\boldsymbol{c}_i,t)-\boldsymbol{f}_{i+2}(\boldsymbol{\ell},t-\tau)\end{aligned}\tag{2.83}$$

Rearranging the terms gives

$$\boldsymbol{r}_{\boldsymbol{\ell}+\boldsymbol{c}_i}(t)-\boldsymbol{r}_{\boldsymbol{\ell}}(t)+\boldsymbol{f}_i(\boldsymbol{\ell}+\boldsymbol{c}_i,t)-\boldsymbol{f}_{i+2}(\boldsymbol{\ell},t)=\boldsymbol{r}_{\boldsymbol{\ell}+\boldsymbol{c}_i}(t-\tau)-\boldsymbol{r}_{\boldsymbol{\ell}}(t-\tau)+\boldsymbol{f}_i(\boldsymbol{\ell}+\boldsymbol{c}_i,t-\tau)-\boldsymbol{f}_{i+2}(\boldsymbol{\ell},t-\tau)\tag{2.84}$$

In other words, the following quantity is a constant of motion

$$\boldsymbol{r}_{\boldsymbol{\ell}+\boldsymbol{c}_i}(t)-\boldsymbol{r}_{\boldsymbol{\ell}}(t)+\boldsymbol{f}_i(\boldsymbol{\ell}+\boldsymbol{c}_i,t)-\boldsymbol{f}_{i+2}(\boldsymbol{\ell},t)\equiv\Delta_i^0(\boldsymbol{\ell})\tag{2.85}$$

which we interpret as the equilibrium separation between particles $\boldsymbol{\ell}$ and $\boldsymbol{\ell}+\boldsymbol{c}_i$ because that is what it should be when the $\boldsymbol{f}$'s are zero. This relation justifies picture given in figure 2.15. It is also the relation to be used to specify correctly set the initial positions of the particles and the $\boldsymbol{f}$'s at time $t=0$. Thus, the local deformation of the solid along direction i is computed as

$$\Delta_i(\boldsymbol{\ell},t) \equiv \underbrace{\boldsymbol{r}_{\boldsymbol{\ell}+\boldsymbol{c}_i}(t)-\boldsymbol{r}_{\boldsymbol{\ell}}(t)-\Delta_i^0(\boldsymbol{\ell})}_{\Delta x}=\underbrace{-\boldsymbol{f}_i(\boldsymbol{\ell}+\boldsymbol{c}_i,t)+\boldsymbol{f}_{i+2}(\boldsymbol{\ell},t)}_{F/k}\tag{2.86}$$

We therefore obtain a relation between the deformation Δx of the "spring" with rest length $\Delta_i^0(\boldsymbol{\ell})$ connecting two adjacent particles and the fields F/k acting on it. It is thus natural to consider this as the expression of Hooke's law with constant of proportionality k equal to 1. From this observation, the interpretation of the $\boldsymbol{f}$ fields becomes clear. They represent the microscopical forces connecting the particles together. The fact the the elasticity constant $k=1$ is fixed holds true only when a solid is modeled alone. Indeed, any re-normalization of $\Delta_i^0(\boldsymbol{r})$ is arbitrary and does not numerically set any specific scale. When modelling the interaction with another body such as another solid or fluid, on the other hand, the choice of the scale of $\Delta_i^0(\boldsymbol{r})$ gives rise to the possibility of adjusting the elastic constant with regards to the spatial scale. Therefore by incorporating an extra scale parameter α to equation (2.55) such that

$$\boldsymbol{q}(t+\tau) = \boldsymbol{q}(t) + \alpha \left(\frac{\boldsymbol{\psi}(t)}{M} + \frac{\boldsymbol{F}(t)}{2M} \right) \tag{2.87}$$

the effect on equation (2.86) is to produce an elastic constant

$$k = \frac{1}{\alpha} \tag{2.88}$$

this possibility will be used in chapters 4 and 5 when modelling the interaction of solids and fluids. Also, an interesting observation can be made here: it is possible to imagine that plasticity and other non-linear situations may be modeled by modifying the value of $\Delta_i^0(\boldsymbol{l})$ with time.

There is another important remark to be made at his stage. Take a one dimensional chain, the summation of the the displacements $\Delta_i(\boldsymbol{\ell}, t)$, as defined in equation (2.86) over all particles is

$$\sum_{\boldsymbol{\ell}} \Delta_i(\boldsymbol{\ell}, t) = \sum_{\boldsymbol{\ell}} -\boldsymbol{f}_i(\boldsymbol{\ell} + \boldsymbol{c}_i, t) + \boldsymbol{f}_{i+2}(\boldsymbol{\ell}, t) = \sum_{\boldsymbol{\ell}} \boldsymbol{J}_{\boldsymbol{\ell}} \tag{2.89}$$

where we have correctly rearranged all terms. Indeed, it is in fact unfortunate that the definition in equation (2.86) is not local since this simple example shows that it would then be straightforward to give $\boldsymbol{J}$ the physical meaning of stress. The local equilibrium used to obtain the wave equation model could have then be composed of two conserved quantities: displacement and stress. We will return to this observation in the last section of this chapter where further developments of our model are presented.

2.4.5 Dissipation and the stationary state

In the above formulation, our solid has no internal dissipation (since $\tau = 1/2$ in equation (2.35) contrary to fluids models) and if moved away from equilibrium, its particles will keep oscillating for ever, possibly producing an overall motion of the object. In order to be able to reach a time-independent state when an external force is applied and thus measure the static deformation resulting from an applied stress, it is convenient to add some dissipation in *ad hoc* way. This is achieved with the following substitution in the dynamics of the model given in equations (2.52) and (2.53)

$$\boldsymbol{\psi} \to \mu \boldsymbol{\psi} \tag{2.90}$$

where μ is a scalar in the range $0 < \mu \leq 1$. When $\mu = 1$, no dissipation take place, but as soon as $\mu < 1$, the momentum $\boldsymbol{\psi}$ is no longer conserved and a damping of the motion occurs as if the entire solid were subject to some external friction.

When the sum of the external forces $\boldsymbol{F}_{\boldsymbol{\ell}}$ is zero, the solid eventually reaches a state where all particles are at rest, in static equilibrium between the external and internal forces. We show that this final stage is independent of the value of μ. Indeed, For a situation at rest (no time dependence), one has $\boldsymbol{r}_{\boldsymbol{\ell}}(t+\tau) = \boldsymbol{r}_{\boldsymbol{\ell}}(t)$, thus equation (2.55) becomes

$$\mu M_{\boldsymbol{\ell}}^{-1}\boldsymbol{\psi}_{\boldsymbol{\ell}}(t) + \mu M_{\boldsymbol{\ell}}^{-1}\frac{\boldsymbol{F}_{\boldsymbol{\ell}}(t)}{2} = 0 \tag{2.91}$$

or more simply

$$\boldsymbol{\psi}_{\boldsymbol{\ell}} + \frac{\boldsymbol{F}_{\boldsymbol{\ell}}}{2} = 0 \tag{2.92}$$

After substitution of this condition in the dynamics given in equations (2.52) (2.53), one obtains

$$\boldsymbol{f}_i(\boldsymbol{\ell} + \boldsymbol{c}_i) = -\boldsymbol{f}_{i+2}(\boldsymbol{\ell}) \tag{2.93}$$
$$\boldsymbol{f}_0(\boldsymbol{\ell}) = -\boldsymbol{f}_0(\boldsymbol{\ell}) = 0 \tag{2.94}$$

This relations will come into use when studying static deformation of objects. Equation (2.93 simply means that the adjacent forces acting on two neighboring particles are identical in the stationary state. Finally, equation (2.100 shows that the final state does not depend on f_0 which already entails that deformations will not depend on the speed of sound of the wave in the solid. The dynamics to reach the stationary state however does.

2.4.6 Dynamic boundary and contact conditions.

As we have already mentioned, the dynamics (2.52) is valid for any number K of neighbors in the lattice through the definition of mass in equation (2.54). It is therefore possible to introduce a dynamically change of the border of a solid. This will be used in the fracture and fragmentation experiments described later on. The rule for a change in topology consists in suppressing the connection between two particles if the energy $E_i = f_i^2$ contained in direction i of either sites is higher than a critical value

$$E_i > \epsilon_{\text{threshold}} \tag{2.95}$$

The effect of this local rule obviously affects the neighboring site. Since, by definition, physical quantities such as mass, momentum and energy depend on the number of connected neighbors, they are consequently not conserved by this change of topology.

The next dynamical condition consists at modelling the contact condition between our solid and any other object. The underlying microscopic principle is

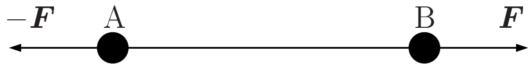

Figure 2.16: A one dimensional 2 particle system considered to study the elastic property of the model.

that solids are in contact through the contact of they constitutive particles. We choose the simplest imaginable case of contact between particles is that of an elastic collisions. This is achieved in the model by computing the external force corresponding to wanted exchange of momentum. In the case of a rigid wall, for instance, this instantaneous force is simply equal to the following transfer of momentum

$$\Delta P = -2\boldsymbol{\psi} \tag{2.96}$$

while for two dynamic objects in contact through particles A and B

$$\Delta P = 2\frac{m_A m_B}{m_A + m_B}(\boldsymbol{u}_A - \boldsymbol{u}_B) \tag{2.97}$$

where $\boldsymbol{u}_A$ and $\boldsymbol{u}_B$ are velocities of the particles namely the instantaneous displacements giving by equation (2.55). Relation (2.97) is classically obtained by the conservation of momentum and energy as can be found in textbooks [3].

Note that depending of the nature of the problem the computational complexity of collision detection may very well be quite heavy with regards to the local computation in the solid. Also, this detection cannot, for numerically obvious reason, be point-like and this therefore introduces a grain to scale of the modelling.

2.4.7 Elastic properties

Although we do not recover the complete relations of linear elasticity, given in equation (2.2), establishing their equivalents in our model allows for a much better understanding of the model and its limits.

1d case

Consider a chain of 2 particles A and B on which a force F is applied such that $F(A) = -F$ and $F(B) = F$, see figure 2.16. Due to the geometry of the system we have $K = 1$ and we assume that M_0 and M are scalars. The only internal fields are $f_0(A)$, $f_3(A)$, $f_0(B)$ and $f_1(B)$, which we want to compute in a static situation. From equations (2.92) and (2.94), one has

$$f_1(B) = -f_3(A) \qquad f_0(A) = f_0(B) = 0 \tag{2.98}$$

Since in this particular situation one has $\psi(A) = f_3(A)$ and $\psi(B) = f_1(B)$, the conditions (2.92) $\psi_{A,B} = -\frac{1}{2}F_{A,B}$ give

$$-\frac{1}{2}F_A = f_3(A) \qquad -\frac{1}{2}F_B = f_1(B) \tag{2.99}$$

that is

$$f_3(A) = \frac{F}{2} \qquad f_1(B) = -\frac{F}{2} \tag{2.100}$$

Therefore the deformation, which we compute from equation (2.86), is

$$r_B - r_A - \Delta_0 = f_3(A) - f_1(B) = F \tag{2.101}$$

We can generalize straightforwardly to a chain of arbitrary length N and constant rest length Δ_0 for each spring in the chain by writing

$$r(N) - r(1) - (N-1)\Delta_0 = \sum_{l=1}^{N-1}\big(r(l+1) - r(l) - \Delta_0(l)\big) = \sum_{l=1}^{N-1}\big(f_3(l) - f_1(l+1)\big) = (N-1)F \tag{2.102}$$

where we have used the transitivity effect of equality (2.93) to compute the values of the f inside the bulk from the values at the borders given by equation (2.100). To understand this relation with regards to Hooke's law $F = k\Delta x$, we write

$$F = \underbrace{\frac{1}{(N-1)}}_{k}\underbrace{\big(\boldsymbol{r}(N) - \boldsymbol{r}(1) - (N-1)\Delta_0\big)}_{\Delta x} \tag{2.103}$$

and observe that the corresponding elasticity coefficient is $k = 1/(N-1)$ and can be adjusted by changing the number of particles in the chain. In practice what does this mean. Suppose you want to model a chain of length l, depending on how many discrete particles you use to numerically segment your chain, you will end up with a more or less elastic chain. Thus your elastic constant is dependent on your computation power and it would have been much better to have a paramter to tune this constant.

Another method which can be considered is changing the value of Δ_0. More explicitly, changing the value of Δ_0 can be seen as changing the value of Δx in Hooke's law. This in turn can be re-absorbed in the elasticity coefficient k. Formally, however, this does not change anything but the scale of the simulation which is arbitrary from the start. It will however be possible, in the case of interacting solids, to use the value of Δ_0 to set a scale for each object and hence determine their relative elasticity.

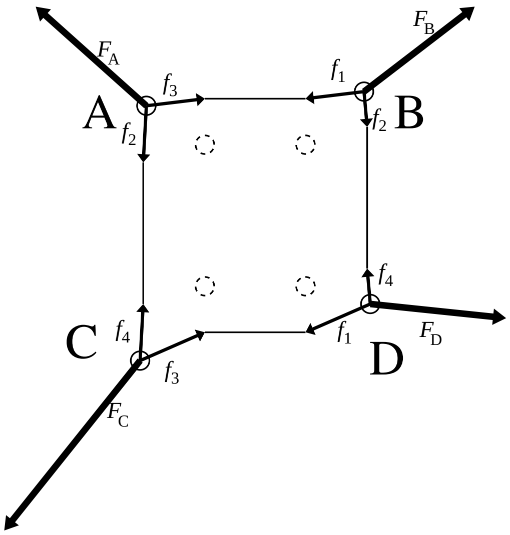

Figure 2.17: Deformation of a simple 2D solid. The original and final particle positions are shown, as well as the internal forces (thin arrows) and external forces (fat arrows).

2d case

The same static deformation calculation can be performed for a simple 2D solid with four particles labeled A, B, C and D as shown on figure 2.17. We restrict here the calculation to the case where $M_0 = 0$ and $K = 2$ since each particle has two neighbors. We denote the external forces as $\boldsymbol{F}_A$, $\boldsymbol{F}_B$, $\boldsymbol{F}_C$, and $\boldsymbol{F}_D$ and we assume that

$$\boldsymbol{F}_A + \boldsymbol{F}_B + \boldsymbol{F}_C + \boldsymbol{F}_D = 0 \tag{2.104}$$

which is a necessary condition in order not to produce an overall motion of the solid even in the stationary case. The problem then consists in finding the following eight values

$$\boldsymbol{f}_2(A) \quad \boldsymbol{f}_3(A), \quad \boldsymbol{f}_1(B) \quad \boldsymbol{f}_2(B), \quad \boldsymbol{f}_3(C) \quad \boldsymbol{f}_4(C), \quad \boldsymbol{f}_1(D) \quad \boldsymbol{f}_4(D) \tag{2.105}$$

The calculation follows the same lines as in the previous section. For each particle, the equilibrium condition allows us to write

$$\begin{array}{rcl} \boldsymbol{\psi}_A + F_A & = & 0 \\ \boldsymbol{\psi}_B + F_B & = & 0 \\ \boldsymbol{\psi}_C + F_C & = & 0 \\ \boldsymbol{\psi}_D + F_D & = & 0 \end{array} \leftrightarrow \begin{array}{rcl} \boldsymbol{f}_2(A) + \boldsymbol{f}_3(A) + F_A & = & 0 \\ \boldsymbol{f}_1(B) + \boldsymbol{f}_2(B) + F_B & = & 0 \\ \boldsymbol{f}_3(C) + \boldsymbol{f}_4(C) + F_C & = & 0 \\ \boldsymbol{f}_1(D) + \boldsymbol{f}_4(D) + F_D & = & 0 \end{array} \tag{2.106}$$

which is a system of four equations and eight unknowns. In the stationary state, equality (2.93) holds, we have $\boldsymbol{f}_4(C) = -\boldsymbol{f}_2(A)$, $\boldsymbol{f}_3(C) = -\boldsymbol{f}_1(D)$, $\boldsymbol{f}_1(B) = -\boldsymbol{f}_3(A)$ and $\boldsymbol{f}_2(B) = -\boldsymbol{f}_4(D)$. We are therefore left with a system of four equations and the following four unknowns

$$\boldsymbol{f}_2(A) \quad \boldsymbol{f}_3(A) \quad \boldsymbol{f}_1(D) \quad \boldsymbol{f}_4(D) \tag{2.107}$$

The system, however, needs an extra condition to be solved because the equations are in fact not independent. One has to take into account the fact that the four particles form a closed loop, namely that following the deformations from $\boldsymbol{r}_A$ through $\boldsymbol{r}_B$, $\boldsymbol{r}_D$ and $\boldsymbol{r}_D$, one ends up again in $\boldsymbol{r}_A$ namely $\sum_{\boldsymbol{l}} \sum_i \Delta_i^0(\boldsymbol{l}) = 0$. Therefore, by using equation (2.85) for each particles, one has the extra equation

$$-\boldsymbol{f}_4(D) + \boldsymbol{f}_1(D) - \boldsymbol{f}_2(A) + \boldsymbol{f}_3(A) = 0 \tag{2.108}$$

After, some algebra, the solution of system (2.106) is

$$\begin{array}{rcl} \boldsymbol{f}_3(A) & = & \frac{1}{2}\left(-\frac{1}{2}\boldsymbol{F}_A + \frac{1}{4}\boldsymbol{F}_B - \frac{1}{4}\boldsymbol{F}_C\right) \\ \boldsymbol{f}_4(D) & = & \frac{1}{2}\left(\ \ \frac{1}{2}\boldsymbol{F}_A + \frac{3}{4}\boldsymbol{F}_B + \frac{1}{4}\boldsymbol{F}_C\right) \\ \boldsymbol{f}_2(A) & = & \frac{1}{2}\left(-\frac{1}{2}\boldsymbol{F}_A - \frac{1}{4}\boldsymbol{F}_B + \frac{1}{4}\boldsymbol{F}_C\right) \\ \boldsymbol{f}_1(D) & = & \frac{1}{2}\left(\ \ \frac{1}{2}\boldsymbol{F}_A + \frac{1}{4}\boldsymbol{F}_B + \frac{3}{4}\boldsymbol{F}_C\right) \end{array} \tag{2.109}$$

We would now like to express the deformations in terms of the stress

$$\begin{array}{rcl} \boldsymbol{r}_B - \boldsymbol{r}_A - \Delta_{AB}^0 = 2\boldsymbol{f}_3(A) & = & \left(-\frac{1}{2}\boldsymbol{F}_A + \frac{1}{4}\boldsymbol{F}_B - \frac{1}{4}\boldsymbol{F}_C\right) \\ \boldsymbol{r}_C - \boldsymbol{r}_A - \Delta_{AC}^0 = 2\boldsymbol{f}_2(A) & = & \left(-\frac{1}{2}\boldsymbol{F}_A - \frac{1}{4}\boldsymbol{F}_B + \frac{1}{4}\boldsymbol{F}_C\right) \\ \boldsymbol{r}_D - \boldsymbol{r}_C - \Delta_{CD}^0 = -2\boldsymbol{f}_1(D) & = & \left(-\frac{1}{2}\boldsymbol{F}_A - \frac{1}{4}\boldsymbol{F}_B - \frac{3}{4}\boldsymbol{F}_C\right) \\ \boldsymbol{r}_D - \boldsymbol{r}_B - \Delta_{BD}^0 = -2\boldsymbol{f}_4(D) & = & \left(-\frac{1}{2}\boldsymbol{F}_A - \frac{3}{4}\boldsymbol{F}_B - \frac{1}{4}\boldsymbol{F}_C\right) \end{array} \tag{2.110}$$

To express these results in terms of elasticity theory, we define the stress tensor S_{xy} as (α denote the x or y component)

$$S_{x\alpha} = F_{A\alpha} + F_{C\alpha} = F_{B\alpha} + F_{D\alpha} \tag{2.111}$$

and

$$S_{y\alpha} = F_{A\alpha} + F_{B\alpha} = F_{C\alpha} + F_{D\alpha} \tag{2.112}$$

The strain tensor ε_{xy} is defined as

$$\varepsilon_{x\alpha} = \frac{1}{2}(u_{B\alpha} - u_{A\alpha}) + \frac{1}{2}(u_{D\alpha} - u_{C\alpha}) \tag{2.113}$$

and

$$\varepsilon_{y\alpha} = \frac{1}{2}(u_{A\alpha} - u_{C\alpha}) + \frac{1}{2}(u_{B\alpha} - u_{D\alpha}) \tag{2.114}$$

where

$$(\boldsymbol{u}_B - \boldsymbol{u}_A) = \boldsymbol{r}_B - \boldsymbol{r}_A - \Delta^0_{AB} \tag{2.115}$$

After some algebra, we obtain that

$$S_{\alpha\beta} = 2\varepsilon_{\alpha\beta} \tag{2.116}$$

Therefore, only one elasticity constant exist in this model and it has a fixed value.

2.5 Applications of the scalar model

The modelling of the elasticity of a solid has been presented above and we have seen that in that respect our model is incomplete. Nonetheless, in the of philosophy of statistical physics, it is possible that some details do not count and the hope is that our model will, to a certain extent, be able to capture important aspects of complex problems. In this section, we apply our model to five different problems which all are interesting because of their border conditions. These problems are: the collision of solids, the contact of a beam between two stops, the problem of a static fracture or crack, the dynamics of a fracture and the fragmentation of a solid. Again, although not completely satisfying with regards to elasticity, we believe that the framework and the facility to model borders conditions, as presented in subsection 2.4.6, are perfectly suited to investigate such kind of problems. In addition, these problems are well adapted to understand the strength and the limits of our approach.

2.5.1 Collisions of solids

We have shown that quantities such as mass, momentum and energy are well-defined in our model. Also, we have seen how the contact of a solid with another solid or a wall can be easily achieved through microscopic elastic collisions. In this experiment, we study the collision of two 1d chains. We will see that although the local interaction is elastic, i.e. momentum and energy are totally transfered from one particle to another, the interaction of chains does not necessarily behave in this way.

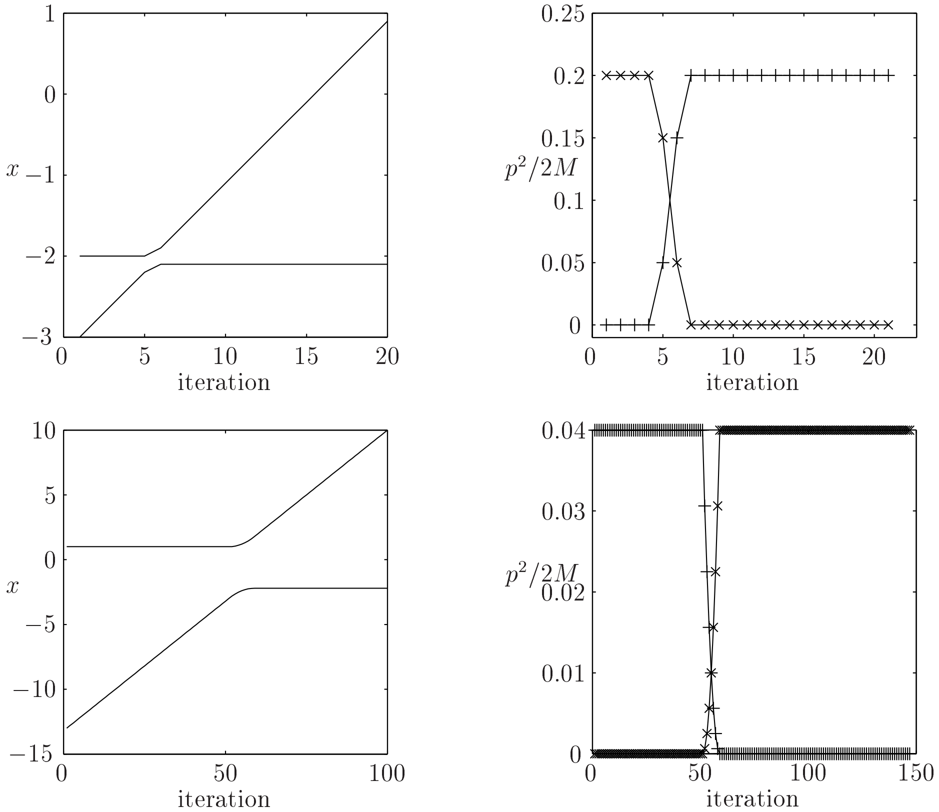

Figure 2.18: The upper plots concern a system of two independent colliding particles while the lower plots are for a system of two chains of five particles each: the trajectory of the chains (left) and their kinetic energy $E = \sum_i f_i^2$ (right). The duration of the interaction is easily expressed as the transient of right plots and we observe that it is dependent of the size of the chain.

The experimental setup is simple. We take two identical chains which are allowed to move only in one dimension. Initially the chains are apart and one of them is given momentum in the direction of the second which is at rest. Once the two extremities of the chains occupy the same physical location, they interact through the local contact condition given in equation (2.97). Figure 2.18 shows the measurements of the trajectory and the kinetic energy

$$E_{\text{kin}} = \frac{(\sum_{\boldsymbol{\ell}} \psi_{\boldsymbol{\ell}})^2}{2\sum_{\boldsymbol{\ell}} m_{\boldsymbol{\ell}}} \tag{2.117}$$

of the chain. The first set of plots are obtained with two free particles[3] and directly illustrate the elastic local interaction mechanism. The second set are obtained with two chains of five particles each. Again, they are characteristic

[3]It is indeed possible in the model to have a particle with no neighbors at all and use the rest field $\boldsymbol{f}_0$ to obtain momentum.

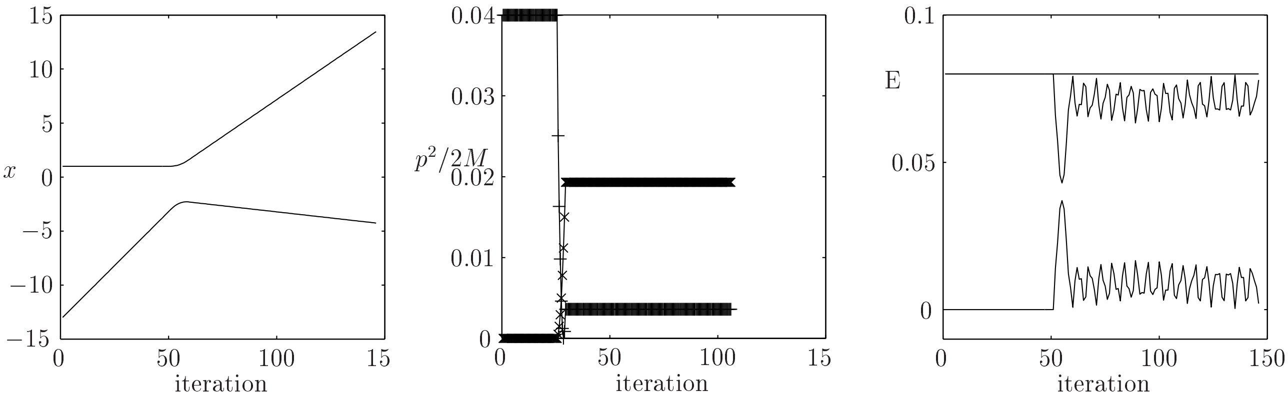

Figure 2.19: The trajectory of two chains particles colliding with a microscopic elastic exchange of momentum (left), their kinetic energies (middle) and their total energies $E = \sum_i f_i^2$ with the total energy of the system remaining constant (right). The non conservation of kinetic energy during the interaction is the clear sign that the collision is inelastic.

of an elastic interaction between chains namely total transfer of momentum and energy. The only notable fact is the duration of the interaction which is related to the size of the chain as can be seen on the transient part of plots in figure 2.18. With chains, however, it is possible to obtain a behavior other than an elastic collision as is illustrated on figure 2.19. Indeed, these plots, which are obtained either by changing the speed of sound in one of the chains or by using chains of differents lengths, show that after the interaction the kinetic energy has not been conserved, see figure 2.19 (middle). The total energy plot, figure 2.19 (right) offers an explanation of what has happened. The total energy of the system is conserved but we see that the energy of each chains oscillates. Indeed, the chains have this capacity and while initially one chain was given momentum in such a way that it did not oscillate, the collision has induced one in the chains. The energy of a chain therefore possesses two components, kinetic energy and internal energy. Unfortunately, an exact interpretation of both energies in term some physical quantities of the system, does not exist at present except for the one dimensional case where it can be easily shown that

$$E = \psi^2 + \boldsymbol{J}^2 \tag{2.118}$$

In the more general case, an expression for the internal energy can be deduced from the total energy E and the kinetic energy expression taking into account that ψ is the momentum of a solid. We therefore can write

$$E_{\text{int}} = \sum_l \sum_{i\geq 0} f_i^2 - \frac{(\sum_l \psi_l)^2}{2\sum_l m_l} \tag{2.119}$$

which is the energy balance for one chain.

The reason why the collision may exhibit these inelasticity effects must be looked for in the duration of contact between chains. Indeed, chains may exchange momentum only as long as they are in contact. In the simulation above, the duration has been modified by either changing the speed of sound in chain, and therefore changing the global rate of momentum transfer within the chain itself, or by changing the length of one chain, and therefore also changing the global rate of transfer of momentum in the chain. In both cases, momentum is not completely distributed within the chains before the end of contact. Consequently, the chains have an oscillating motion and the collision is inelastic. To conclude, let say that it has only been possible to put forward the existence of an inelastic effect and to see that it is correlated it to the time of contact of the chains. The exact characterisation and prediction of the collision has not yet been obtained in our model nor is it clear whether it is possible in real systems. Therefore, whether inelastic effects of real solid systems are to be put in correspondence with this feature of our model is yet to be established. Nevertheless, it is commonly believed that collisions of macroscopic objects are inelastic and in that respect our model has the advantage of proposing a simple explanation for the mechanism.

2.5.2 The contact of a beam between two stops

Contact conditions in mechanical systems is of high interest in a wide range of engineering problem from brakes in a car to film coating. The theoretical understanding of such systems however is much less deep. This is mainly due to the fundamental difficulties of the mathematical analysis. In fact, very simple systems already offer difficult resolution, often only achieving existence theorems as a result. A better understanding of complex mechanical problems therefore can, still today, be achieved via simple systems. The experimental setup of the system we shall consider here, and which was already presented in section 2.2.2, is that of a beam attached at one end and constrained at the other by two stops, see figure 2.20. The beam is forced into a oscillatory motion and the contact of the free end with the stops introduces a dynamical contact condition. This problem has been studied mathematically in [9] with a numerical implementation using a finite difference method. The main result are the existence and uniqueness of a solution $y(t)$ to the problem giving the vertical displacement of the beam and that the properties of the function $y(t)$ can exhibit chaotic behavior. The results of our simulation of the problem shown on figure 2.20 indeed indicates that the position $y(t)$ of the free end as a function of time is more than noisy. This is confirmed by the fourier transform of this signal which clearly illustrates the complex behavior of the motion. To conclude, we see that our model can very easily model complex problems which require complicate mathematical analysis and that it achieves similar results with a simple numerical scheme.

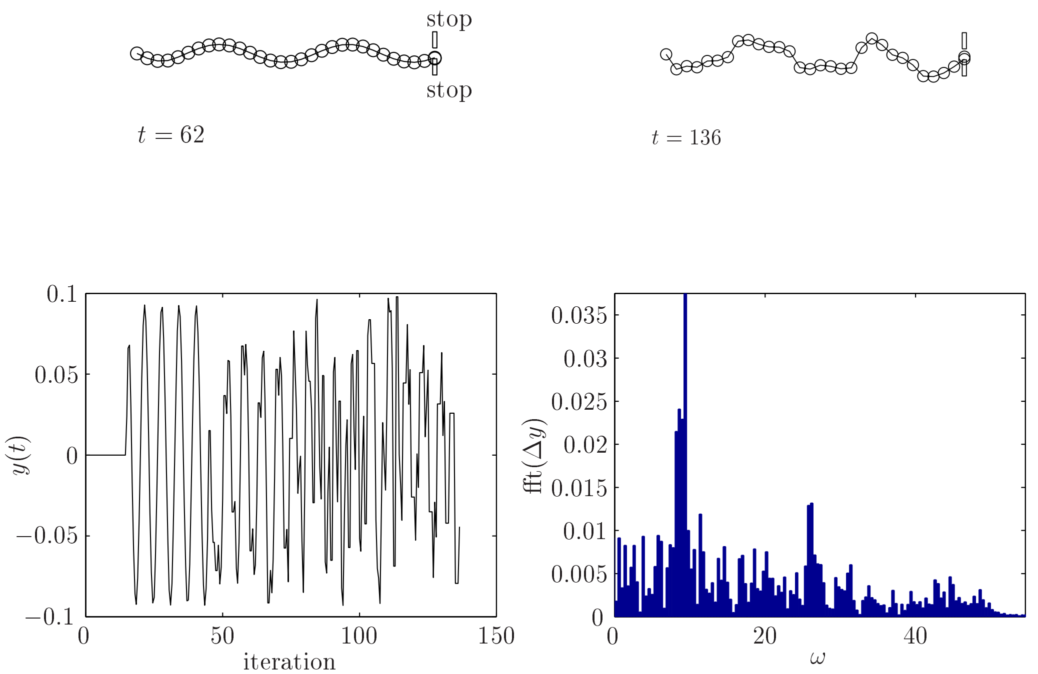

Figure 2.20: The setup of the simulation is illustrated on the top pictures for two different iteration steps. One end of the beam is fix and forced with an oscillating motion while the other end is free to move but constrained by two stops. The bottom plots show the position of the free end as a function of time (left) and the fourier transform of this signal (right).

2.5.3 Energy at the tip of a crack

As a first step towards the modelling of a dynamical fracture, we look at the stress field at the tip of a one dimensional stationary crack. This static problem has the advantage of having a known analytical solution. It also allows us to validate the ability of our model to take arbitrary borders into account.

Consider a solid under mode-I load i.e. the stress applied to the solid is perpendicular to the direction of the crack, see figure 2.21 (left). To obtain a mode-I load with our model, we procede in the following way. The borders parallel to the crack are forced to be fixed by computing the exact force which compensates the motion of particles. Then, the fields f_{2y} and f_{4y} are given an constant initial value $\pm\sigma_0$. The load is then left to evolve until it is equilibrated in the solid. Once this is done, we measure the excess in stress $\sigma = |f_{2y} - f_{4y} - 2\sigma_0|$. The measure of σ is justified by our version of Hooke's law given in section 2.4.4, in particular equation (2.86). The analytical results [16] for an elliptical crack

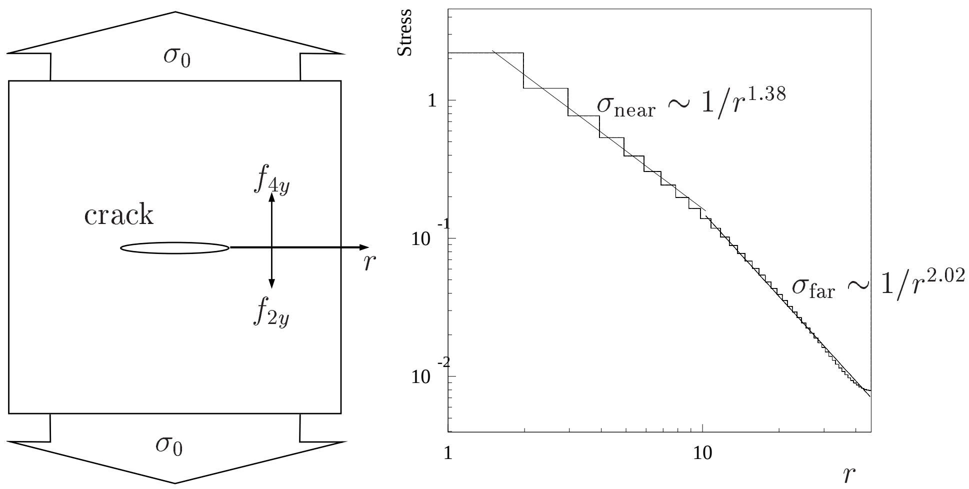

Figure 2.21: The stress field at the tip of a crack. (left) the solid is initiated with a crack in its center and a uniform mode-I load is applied. (right) The stress field in the direction of the load is measured as of the tip of the crack level along the axis parallel to the crack. As expected from theory, the plot fits with a power-law with exponent equal to -2.0 far from the tip while near to the tip the exponent decreases but does not attain the expected value of $-1/2$.

in an infinite elastic medium are that, near to the tip, the field σ_{near} decays like $1/r^{1/2}$ where r is the distance to the crack tip and that, far from the tip, the field σ_{far} is that of a dipole namely it decays like $1/r^2$. Figure 2.21(right) shows in log-log scale, the plot of this measurement. We observe that, as expected, the stress field behaves as that of a dipole far from the tip. Near to the tip, however, we do not recover the theoretical value of $1/2$ for the exponent. The fact that the value is lower than the dipole case indicates, though, that the correct tendency is obtained. These values do not change for larger simulations where a better precision might have completely recovered the exact exponents. The discrepancy may most probably be accounted for by our degenerate elasticity. To conclude, these measurements clearly show that our model has the ability to capture some essential ingredients of static fracture and we will see below that it also manages good results with the dynamic case.

2.5.4 Fracture

The dynamics of fracture mechanics[5] is a vast subject of research with very difficult problems to solve, theoretically and experimentally. The subject was first recognized by Galilee himself in his famous treaties *Two new sciences* and has achieved much less success over the centuries than the kinetic theory of bodies. Even today, the gap between theoretical results and experiments still exists. It

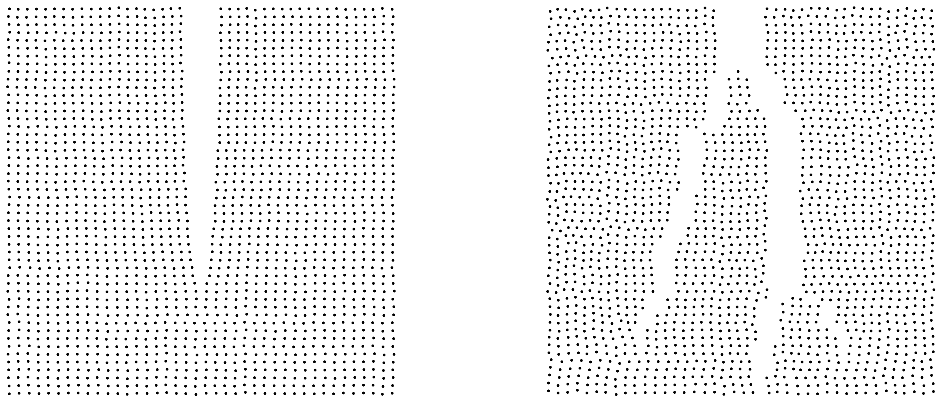

Figure 2.22: A smooth fracture (left) and a branching fracture (right). Both fracture are obtained with an initial notch in a solid under mode-I load. The parameters which distinguish the results of the simulation are the dissipation in the solid and the disorder on the threshold of fracture.

is in the bridging of such a gap that we believe our approach can shed light on the subject. The most comprehensive numerical study on the matter has consisted in modelling the whole physical process at an atomic level via monte-Carlo methods[7]. The results are have yielded possibilities not imagined before such as supersonic crack speeds. This approach however contain two correlated limits: the computer power involved and the short time scale explored. It is at this point that the developments of a time scale free mesoscopic approach may provide an insightful approach to the problem. Indeed, the computer power needed is very low, without speaking of the intrinsic parallelization of the scheme, and there is no typical time-scale. In the following simulations, we show that our model can reproduce the following experimental fact: the transition between branching fracture and smooth fracture occurs at about half the speed of sound [16]. This observation has no theoretical explanation. The fact that our incomplete elasticity model based on simple a wave propagation can reproduce the transition is a indication that the Navier equation contains all the necessary information but that the dynamical border conditions is the main analytical difficulty.

The numerical setup of our simulations is simple. A two dimensional solid is put under mode-I load in an identical way to the case of a stationary crack, see the previous section. The fracture is initiated by introducing a small notch in the direction perpendicular to the load and it is allowed to develop according the dynamic border condition exposed in section 2.4.6. The parameters of the experiments are: the dissipation μ and disorder ϵ on the fracture threshold. The two types of fracture which can be obtained are shown on figure 2.22. The type of fracture results from a correct, but unfortunately not identified, combination

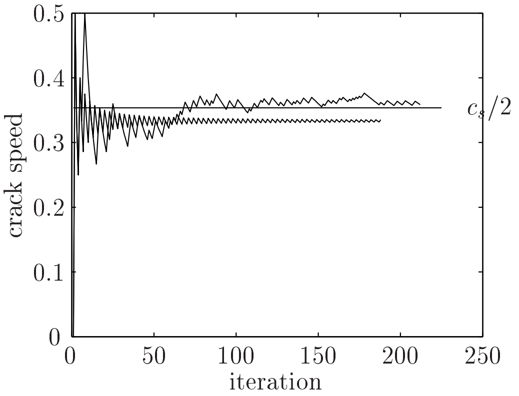

Figure 2.23: The speeds of smooth and branching fractures. As is known experimentally, we see that the transition between the two types of fracture occurs at about half the speed of sound.

of dissipation μ and disorder ϵ. Figure 2.23 shows the speeds of both types of fracture. We observe that the speed of the branching fracture is higher than $c_s/2$ and also more erratic than the speed of the smooth fracture which remains below $c_s/2$. This transition is conserved when changing the value of the speed of sound. The intuitive understanding of this phenomena is as follows: if the fracture advances faster than it is possible for the energy released by the fracture to reach the tip, the energy left behind is able to create branches and hence other tips which eventually will themselves start to grow.

To conclude, let us say that the ability of our model to capture the transition between a smooth and a branching crack is very encouraging. This ability can probably greatly be attributed to the mechanism by which the fracture grows. Indeed, the criteria for removing connections in the solid is essentially based on a energy concept. Our improved scalar wave model, therefore, seems well suited to model the transport of energy in a solid and hence correctly model the growth process of a fracture.

2.5.5 Fragmentation

To complete our study of fracture phenomena, we briefly overview fragmentation simulations. Indeed, in its extreme limit, fracture phenomena results in the destruction of the solid under stress. The question which arises then is to see whether the fragments follow any coherent behavior and whether this may result from the dynamics of the destructive process. Experimental data have shown that the distribution of fragment sizes follow a power-law and several theoretical models have been proposed to understand such distributions [16]. We show that our model and our fracture rule are sufficient to reproduce the main experimental behavior.

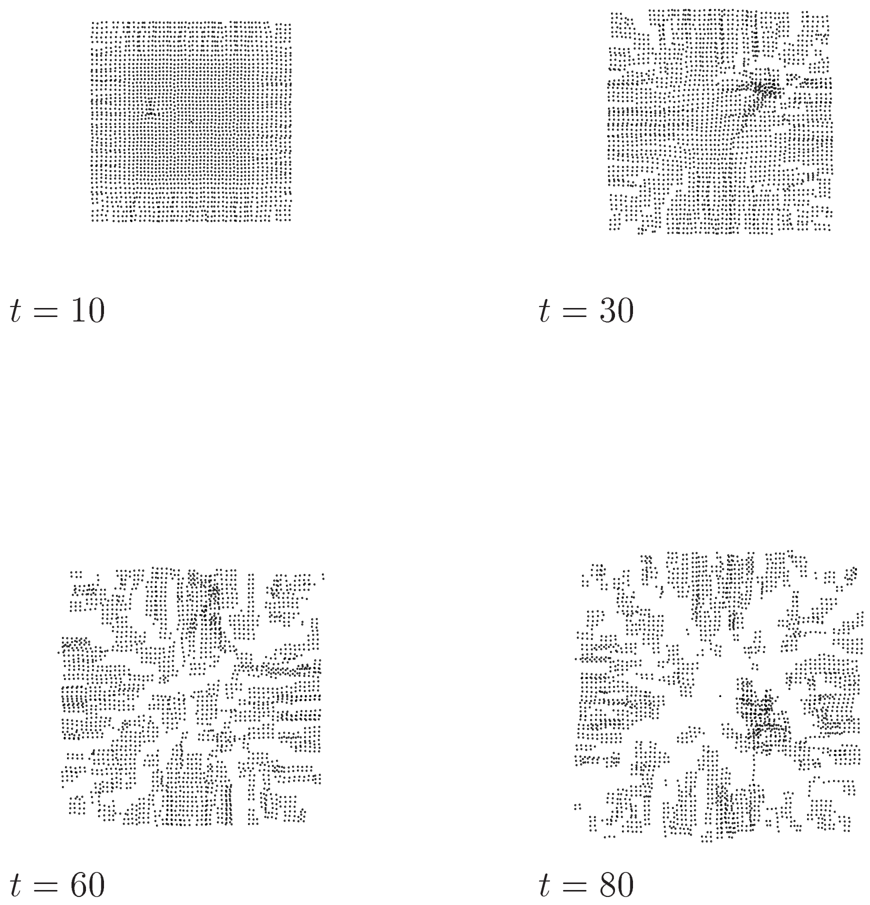

Figure 2.24: The spatial distribution of fragments for several time steps of simulation. The destruction of the solid is achieved by initiating all the $\boldsymbol{f}_i$ at a value near to the fracture threshold. The resulting size distribution of fragments follows a power-law distribution.

In order achieve very high load of the solid, all the $\boldsymbol{f}_i$ in the solid are initiated near the critical threshold E_c. Again, the parameters are the dissipation μ and the disorder ϵ on the threshold. The breaking of the solid is not instantaneous as is shown on figure 2.24 for several time steps of the simulation. Once all the energy in the solid is dissipated, we look at the distribution of fragment sizes[4], see figure 2.25. The exponent of the power-law from our simulation is $\alpha \sim 1$ while experimental data report exponents between 0.5 and 1.0. More

[4]The fragments are identified using a simple color flooding algorithm where all connected particles end up with the same color or number. The size of a fragment is then simply the number of particles with the same color

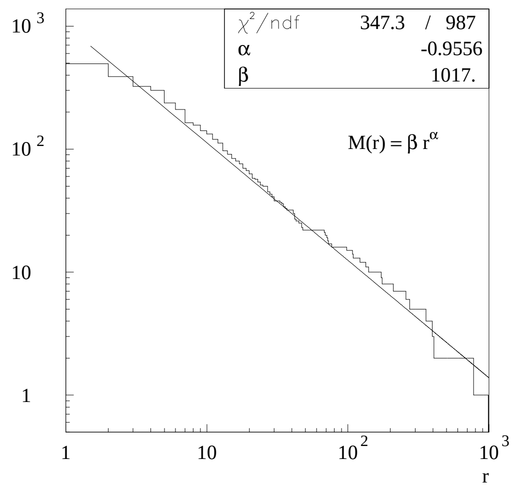

Figure 2.25: The size distribution of fragments in a typical fragmentation experiment. The distribution follows a power law with exponent equal to ~ 1 as has been seen in experimental data where the exponent ranges from 0.5 to 1.0

extensive simulations can obviously be done. First the manner in which the dissipation μ and the threshold disorder ϵ control the resulting distribution may be explored. In our simulation, we were concerned by the existence of a power-law distribution for the size of fragments, but other more trivial distributions do exists. An example is given by the total destruction case, where all fragments have size one, which is obtained with $\epsilon = 0$ and the a solid initiated at E_c. The fragmentation process in this case only takes one iteration which brings us to the second set of possible developments. Indeed, our model allows us to exactly follow the process of destruction as shown on figure 2.24. The difficulty of this direction of simulation, however, is the lack of experimental results to validate any theoretical model or numerical simulations. In conclusion, our model has, with this last example, definitively shown its ability at modelling a diversity of problems by reproducing essential results. This ease at adapting itself to various problems overweighs the theoretical limits which have been exposed in previous sections and can only encourage us to go forwards to improve our approach.

2.6 Further developments

In the previous section, we have presented a lattice Boltzmann model to simulate several different problems related to the dynamics of a solid body and the theory of linear elasticity. Although the model posseses limitations, most notably a degenerate elasticity, it is able to reproduce several important features of solid dynamics. Nonetheless it is not able to fully recover the theory of linear elasticity to the same extent than its equivalent for fluids dynamics can reproduce the Navier-Stokes equation. Therefore, we argue here about the main reason we believe resides behind this limitation and from the argument propose new possibilities for our model. Lets first reconsider the two fundamental equations which lead to the Navier equation namely Newton's law and the stress-strain equation

$$\partial_\beta \sigma_{\alpha\beta} + \rho F_\alpha = \rho \ddot{u}_\alpha \tag{2.120}$$

$$\sigma_{\alpha\beta} = \lambda \varepsilon_{\gamma\gamma} \delta_{\alpha\beta} + 2\mu \varepsilon_{\alpha\beta} \tag{2.121}$$

We also recall the BGK Boltzmann equation

$$f_i(\boldsymbol{r} + \boldsymbol{c}_i \Delta r, t + \Delta t) - f_i(\boldsymbol{r}, t) = \frac{1}{\tau}\left(f_i^{(0)}(\boldsymbol{r}, t) - f_i(\boldsymbol{r}, t)\right) \tag{2.122}$$

the choice for the local equilibrium in the lattice Boltzmann model

$$f_i^{(0)} = a\psi + b\boldsymbol{c}_i \cdot \boldsymbol{J} \tag{2.123}$$

and the two continuity equations

$$\partial_t \psi + \partial_\beta \boldsymbol{J}_\beta = 0 \tag{2.124}$$

$$\partial_t \boldsymbol{J}_\alpha + \partial_\alpha \Pi_{\alpha\beta} = 0 \tag{2.125}$$

In order to have a time reversible scheme, it is necessary to have a relaxation time $\tau = 1/2$ in the Boltzmann equation. In this case, the Chapman-Enskog procedure shows that $\Pi_{\alpha\beta} = \Pi_{\alpha\beta}^{(0)}$ and therefore

$$\begin{aligned}
\Pi_{\alpha\beta}^{(0)} &= \sum_i m_i f_i^{(0)} \boldsymbol{c}_{i\alpha} \boldsymbol{c}_{i\beta} \\
&= \sum_i m_i \big(a\psi + b\boldsymbol{c}_{i\gamma} J_\gamma\big) \boldsymbol{c}_{i\alpha} \boldsymbol{c}_{i\beta} \\
&= a\psi \sum_i m_i \boldsymbol{c}_{i\alpha} \boldsymbol{c}_{i\beta} + 0 \\
&= aC_2 \psi
\end{aligned}$$

and equation (2.125) now can be written as

$$\partial_t \boldsymbol{J}_\alpha + aC_2 \partial_\alpha \psi = 0 \tag{2.126}$$

Finally we obtain the scalar wave equation by combining equation (2.124) and equation (2.126). Suppose now that ψ relates to the variation of displacement $\dot{u}$ and that $\boldsymbol{J}$ relates to the stress σ. Equation (2.124) can then be read as

$$\ddot{u} = \nabla \sigma \tag{2.127}$$

which is Newton's law in the absence of external force and equation (2.125) reads as

$$\dot{\sigma} = \nabla \dot{u} \tag{2.128}$$

or equivalently after integration $\sigma = \nabla u$ which we can compare to the stress-strain equation. These comparisons, however, are not complete because equations (2.120) and (2.121) contain tensor objects while equations (2.124) and (2.125) do not. From this observation, we can now conclude that if the local equilibrium contains tensor objects then it might be possible to recover equations (2.120) and (2.121) completely and hence obtain the Navier equation. In the scalar case, however, we only recover a wave equation which in a sense is a partial Navier equation. Indeed, we have seen that the Navier equation is mathematically identical to a system of wave equations. In other words, we are tempted to say that the Navier equation is a general form of wave equation and that by using the correct mathematical objects, the lattice Boltzmann method could in fact recover it.

In summary then, the lattice Boltzmann model presented in previous section is incomplete because its local equilibrium is too simple and the best way to improve the model is to start with a totally new local equilibrium and not try to generalize from the resulting dynamics. In the rest of this section, we present two possibilities at incorporating tensor objects in the local equilibrium which we have partly explored. The general method is to first propose a tensor local equilibrium, then to verify that the quantities used have the correct conservation properties. This verification gives rise to constraints on the coefficients used in the local equilibrium. An additional constraints comes into play when the conservation of an extra quadratic form is required for numerical stability reasons. All these constraints may or may not be satisfied once a lattice geometry is to be found for the numerical scheme. However, if these constraints are satisfied, the next logical step is to perform a simple numerical check. Indeed, the most important step is to verify through the Chapman-Enskog procedure that the macroscopic equation really is the Navier equation. This is a tedious task and it is always best to have good reasons to embark in it.

2.6.1 Tensor coefficient

The first attempt we have considered is to introduce tensor coefficients in the local equilibrium used in the scalar wave case

$$f_i^{(0)} = a\psi + \bar{a}_{\mu\nu}\psi c_{i\mu} c_{i\nu} + b\boldsymbol{J} \cdot \boldsymbol{c}_i \tag{2.129}$$

The BGK Boltzmann equation then gives then the following dynamics

$$f_i' = 2a\psi + 2\bar{a}_{\mu\nu}\psi c_{i\mu}c_{i\nu} - f_i + 2b\boldsymbol{J}\cdot\boldsymbol{c}_i \quad (2.130)$$
$$f_0' = 2a_0\psi - f_0 \quad (2.131)$$

The conservation of ψ after collision now requires that

$$\psi^{\text{out}} = \sum_{i\geq 0} m_i f_i^{\text{out}} \quad (2.132)$$
$$= m_0(2a_0\psi - f_0) + \sum_{i>0} m_i(2a\psi + 2\bar{a}_{\mu\nu}\psi c_{i\mu}c_{i\nu} - f_i + 2b\boldsymbol{J}\cdot\boldsymbol{c}_i) \quad (2.133)$$
$$= 2a_0m_0\psi - m_0f_0 + 2aC_0\psi + 2\bar{a}_{\mu\nu}C_2\psi\delta_{\mu\nu} - (\psi - m_0f_0) + 0 \quad (2.134)$$
$$= (2m_0a_0 + 2C_0a + 2C_2\bar{a}_{\mu\nu} - 1)\psi \quad (2.135)$$

therefore the following relation must hold

$$a_0m_0 + aC_0 + \bar{a}_{\mu\nu}C_2\delta_{\mu\nu} = 1 \quad (2.136)$$

The conservation of $\boldsymbol{J}$ requires

$$\boldsymbol{J}^{\text{out}} = \sum_{i>0} m_i f_i^{\text{out}}\boldsymbol{c}_i \quad (2.137)$$
$$= \sum_{i>0} m_i(a\psi + \bar{a}_{\mu\nu}\psi c_{i\mu}c_{i\nu} + b\boldsymbol{J}\cdot\boldsymbol{c}_i)\boldsymbol{c}_i \quad (2.138)$$
$$= 0 + 0 + b\boldsymbol{J}\cdot\sum_{i>0} m_i c_{i\mu}c_{i\nu} \quad (2.139)$$
$$= bC_2\boldsymbol{J}\delta_{\mu\nu} \quad (2.140)$$
$$(2.141)$$

therefore the following relation must hold

$$bC_2 = 1 \quad (2.142)$$

The conservation of a quadratic form $E = \gamma m_0 f_0 + \sum_{i>0} m_i f_i^2$ in order to ensure numerical stability requires

$$
\begin{aligned}
E^{\text{out}} &= \gamma m_0 f_0^{\text{out }2} + \sum_{i>0} m_i f_i^{\text{out }2} \\
&= \gamma m_0 (2a_0\psi - f_0)^2 + \sum_{i>0} m_i (2a\psi + 2\bar{a}_{\mu\nu}\psi c_{i\mu} c_{i\nu} - f_i + 2b\boldsymbol{J}\cdot\boldsymbol{c}_i)^2 \\
&= \gamma m_0 (4a_0^2\psi^2 - 4a_0\psi f_0 + f_0^2) \\
&\quad + \sum_{i>0} m_i \big(4a^2\psi^2 + 4\bar{a}_{\mu\nu}\psi^2 c_{i\mu}c_{i\nu}c_{i\gamma}c_{i\delta} + f_i^2 + 4b^2(\boldsymbol{J}\cdot\boldsymbol{c}_i)^2 \\
&\quad + 8a\psi\bar{a}_{\mu\nu}\psi\boldsymbol{c}_{i\mu}c_{i\nu} - 4a\psi f_i + 8a\psi b\boldsymbol{J}\cdot\boldsymbol{c}_i - 4\bar{a}_{\mu\nu}\psi\boldsymbol{c}_{i\mu}\boldsymbol{c}_{i\nu} \\
&\quad + 8\bar{a}_{\mu\nu}\psi\boldsymbol{c}_{i\mu}\boldsymbol{c}_{i\nu} b\boldsymbol{J}\cdot\boldsymbol{c}_i - 4bf_i\boldsymbol{J}\cdot\boldsymbol{c}_i\big) \\
E^{\text{out}} - E &= \gamma m_0 (4a_0^2\psi^2 - 4a_0\psi f_0) + 4a^2\psi^2 C_0 + 4\bar{a}_{\mu\nu}^2\psi^2 C_4 \\
&\quad + 4b^2\sum_{i>0} m_i(\boldsymbol{J}\cdot\boldsymbol{c}_i)^2 + 8a\bar{a}_{\mu\nu}\psi^2 C_2 - 4a\psi(\psi - m_0 f_0) \\
&\quad + 8ab\psi\sum_{i>0} m_i\boldsymbol{J}\cdot\boldsymbol{c}_i - 4\bar{a}_{\mu\nu} m_i f_i c_{i\mu}c_{i\nu} \\
&\quad + 8\bar{a}_{\mu\nu} b\psi\sum_{i>0} m_i c_{i\mu}c_{i\nu}\boldsymbol{J}\cdot\boldsymbol{c}_i - 4b\sum_{i>0} m_i f_i\boldsymbol{J}\cdot\boldsymbol{c}_i \\
&= (4\gamma m_0 a_0^2 + 4a^2 C_0 + 4\bar{a}_{\mu\nu}^2 C_4 + 8a\bar{a}_{\mu\nu} C_2 - 4a)\psi^2 + (4am_0 - 4\gamma m_0 a_0)\psi f_0 \\
&\quad \overbrace{+4b^2\sum_{i>0} m_i(\boldsymbol{J}\cdot\boldsymbol{c}_i)^2 - 4b\sum_{i>0} m_i f_i\boldsymbol{J}\cdot\boldsymbol{c}_i}^{\text{(a)}} + \overbrace{8ab\psi\sum_{i>0} m_i\boldsymbol{J}\cdot\boldsymbol{c}_i}^{\text{(b)}} \\
&\quad -4\bar{a}_{\mu\nu}\psi\sum_{i>0} m_i f_i c_{i\mu}c_{i\nu} + \overbrace{8\bar{a}_{\mu\nu} b\psi\sum_{i>0} m_i c_{i\mu}c_{i\nu}\boldsymbol{J}\cdot\boldsymbol{c}_i}^{\text{(c)}}
\end{aligned}
$$

The (a) term vanishes because

$$
\begin{aligned}
& 4b^2\sum_{i>0} m_i(\boldsymbol{J}\cdot\boldsymbol{c}_i)^2 - 4b\sum_{i>0} m_i f_i\boldsymbol{J}\cdot\boldsymbol{c}_i \\
=\ & 4b^2\sum_{i>0} m_i J_\gamma J_\delta c_{i\gamma}c_{i\delta} - 4b\boldsymbol{J}\sum_{i>0} m_i f_i\boldsymbol{c}_i \\
=\ & 4b^2 J_\gamma J_\delta\sum_{i>0} m_i c_{i\gamma}c_{i\delta} - 4b\boldsymbol{J}\cdot\boldsymbol{J} \\
=\ & 4b^2 J_\gamma J_\delta C_2 - 4b\boldsymbol{J}\cdot\boldsymbol{J} \\
=\ & 4b\boldsymbol{J}\cdot\boldsymbol{J} - 4b\boldsymbol{J}\cdot\boldsymbol{J} \\
=\ & 0
\end{aligned}
\tag{2.143}
$$

and both the (b) and (c) term vanish because they are summations over odd tensors. To suppress the term in ψf_0, we need to fix the value of γ to

$$\gamma = \frac{a}{a_0} \tag{2.144}$$

which also has the effect of killing the term in ψ^2. We are therefore left with the term

$$-4\bar{a}_{\mu\nu}\psi \sum_{i>0} m_i f_i c_{i\mu} c_{i\nu} = -4\bar{a}_{\mu\nu}\psi\Pi_{\mu\nu} \tag{2.145}$$

which if $\bar{a}_{\mu\nu}$ is anti-symmetrical vanishes with the summation effect of $\Pi_{\mu\nu}$. Unfortunately having a anti-symmetrical $\bar{a}_{\mu\nu}$ does not make any sense because the $\bar{a}_{\mu\nu} c_{i\mu} c_{i\nu}$ term in the local equilibrium would also vanish after summation. For this reason, it is necessary to look at another way at creating tensor objects in the local equilibrium

2.6.2 $\boldsymbol{J}$-Π equilibrium

This attempt is more in line with the argument presented at the beginning of the section namely define a local equilibrium where the conserved quantities are a vector and a tensor. The first calculations however show that all moments of the base vectors f_i will appear and we therefore write the most general local equilibrium

$$\begin{aligned} f_i^{(0)} &= a\psi + \bar{a}\mathrm{Tr}\Pi + b\boldsymbol{J}\cdot\boldsymbol{c}_i + e\Pi_{\mu\nu}c_{i\mu}c_{i\nu} && (2.146)\\ f_0^{(0)} &= a_0\psi + \bar{a}_0\mathrm{Tr}\Pi && (2.147)\end{aligned}$$

where $\mathrm{Tr}\Pi = \Pi_{\mu\mu}$. We now show the conservation law in a slightly different way than before. Indeed, a simple algebraic manipulation of the collision dynamics $f_i' = 2(f_i^{(0)} - f_i)$ can show that the conservation of quantity Q consists in showing that is equal to its equilibrium value $Q^{(0)}$. The conservation of ψ therefore requires that

$$\begin{aligned} \psi &= \sum_{i\geq 0} m_i f_i^{(0)} && (2.148)\\ &= m_0 a_0\psi + m_0\bar{a}_0\mathrm{Tr}\Pi + \sum_{i>0} m_i\left[a\psi + \bar{a}\mathrm{Tr}\Pi + bJ_\mu c_{i\mu} + e\Pi_{\mu\nu}c_{i\mu}c_{i\nu}\right] && (2.149)\\ &= m_0 a_0\psi + m_0\bar{a}_0\mathrm{Tr}\Pi + aC_0\psi + \bar{a}C_0\mathrm{Tr}\Pi + 0 + eC_2\Pi_{\mu\nu}\delta_{\mu\nu} && (2.150)\\ &= (m_0 a_0 + aC_0)\psi + (m_0\bar{a}_0 + \bar{a}C_0 + eC_2)\mathrm{Tr}\Pi && (2.151)\end{aligned}$$

which lead to the constraints

$$m_0 a_0 + aC_0 = 1 \tag{2.152}$$
$$m_0 \bar{a}_0 + \bar{a}C_0 + eC_2 = 0 \tag{2.153}$$

The conservation of $\boldsymbol{J}$ requires that

$$J_\mu = \sum_{i>0} m_i f_i^{(0)} c_{i\mu} \tag{2.154}$$
$$= 0 + bC_2 J_\nu \delta_{\mu\nu} + 0 \tag{2.155}$$

which leads to the constraint

$$bC_2 = 1 \tag{2.156}$$

The conservation of Π requires that

$$\Pi_{\mu\nu} = \sum_{i>0} m_i f_i^{(0} c_{i\mu} c_{i\nu} \tag{2.157}$$
$$= \sum_{i>0} m_i \big(a\psi + \bar{a}\mathrm{Tr}\Pi + b\boldsymbol{J} \cdot \boldsymbol{c}_i + e\Pi_{\gamma\delta} c_{i\gamma} c_{i\delta} \big) c_{i\mu} c_{i\nu} \tag{2.158}$$
$$= aC_2 \psi \delta_{\mu\nu} + \bar{a}C_2 \mathrm{Tr}\Pi \delta_{\mu\nu} + 0 + eC_4 \mathrm{Tr}\Pi \delta_{\mu\nu} + 2eC_4 \Pi_{\mu\nu} \tag{2.159}$$

which leads to the constraints

$$a = 0 \tag{2.160}$$
$$\bar{a}C_2 + eC_4 = 0 \tag{2.161}$$
$$2eC_4 = 1 \tag{2.162}$$

The choice of the lattice must therefore have enough symmetry to construct the tensor $C_4 = \sum_i c_{i\alpha} c_{i\beta} c_{i\gamma} c_{i\delta}$. The first possibility happens to be an hexagonal lattice. Finally, to satisfy all the constraints due to the conservation laws, we obtain for the local equilibrium coefficients

$$a = 0 \tag{2.163}$$
$$\bar{a} = -\frac{1}{2C_2} \tag{2.164}$$
$$m_0 a_0 = 1 \tag{2.165}$$
$$m_0 \bar{a}_0 = \frac{C_0}{2C_2} - \frac{C_2}{2C_4} \tag{2.166}$$
$$e = \frac{1}{2C_4} \tag{2.167}$$

The last step consist at looking at the conservation of a quadratic form E which should ensure the numerical stability of the scheme. To facilate the algebra of the verification of the conservation of a quadratic form $E = \gamma m_0 f_0^2 + \sum_{i>0} m_i f_i^2$ given the dynamics $f_i' = 2(f_i^{(0)} - f_i)$, we can first develop the expression

$$\begin{aligned}
\gamma m_0 f_0'^{\,2} + \sum_{i>0} m_i f_i'^{\,2} &= \gamma m_0 (2f_0^{(0)} - f_0)^2 + \sum_{i>0} m_i (2f_i^{(0)} - f_i)^2 && (2.168)\\
&= \gamma m_0 f_0^2 + \sum_{i>0} m_i f_i^2 + 4\gamma m_0 (f_i^{(0)\,2} - f_i^{(0)} f_0) && (2.169)\\
&\quad +4 \sum_{i>0} m_i (f_i^{(0)\,2} - f_i^{(0)} f_i) && (2.170)
\end{aligned}$$

$$\underbrace{\gamma m_0 f_0^{(0)\,2} + \sum_{i>0} m_i f_i^{(0)\,2}}_{A} = \underbrace{\gamma m_0 f_i^{(0)} f_0 + \sum_{i>0} m_i f_i^{(0)} f_i}_{B} \qquad (2.171)$$

and we see that the conservation of E is equivalent to verifying that $A - B = 0$. Hence

$$\begin{aligned}
A &= \gamma m_0 (a_0 \psi + \bar{a}_0 \mathrm{Tr}\Pi)^2 + \sum_{i>0} m_i \left[\bar{a}\mathrm{Tr}\Pi + b J_\mu c_{i\mu} + e \Pi_{\mu\nu} c_{i\mu} c_{i\nu}\right]\\
&= \gamma m_0 a_0^2 \psi^2 + \gamma m_0 \bar{a}_0 (\mathrm{Tr}\Pi)^2 + 2\gamma m_0 a_0 \bar{a}_0 \psi \mathrm{Tr}\Pi + \bar{a}^2 C_0 (\mathrm{Tr}\Pi)^2 + b^2 J_\mu J_\nu C_2 \delta_{\mu\nu}\\
&\quad + e^2 C_4 \Pi_{\mu\nu} \Pi_{\alpha\beta} (\delta_{\mu\nu}\delta_{\alpha\beta} + \delta_{\mu\alpha}\delta_{\nu\beta} + \delta_{\mu\beta}\delta_{\nu\alpha}) + 2\bar{a} e \mathrm{Tr}\Pi\, \Pi_{\mu\nu} C_2 \delta_{\mu\nu}\\
&= \gamma m_0 a_0^2 \psi^2 + 2\gamma m_0 a_0 \bar{a}_0 \psi \mathrm{Tr}\Pi + (\gamma m_0 \bar{a}_0 + \bar{a}^2 C_0 + e^2 C_4 + 2\bar{a} e C_2)(\mathrm{Tr}\Pi)^2\\
&\quad + 2e^2 C_4 (\Pi_{\mu\nu})^2 + b^2 J_\mu J_\nu C_2 \delta_{\mu\nu}
\end{aligned}$$

$$\begin{aligned}
B &= \gamma m_0 (a_0 \psi + \bar{a}_0 \mathrm{Tr}\Pi) f_0 + \sum_{i>0} m_i (\bar{a}\mathrm{Tr}\Pi + b J_\mu c_{i\mu} + e \Pi_{\mu\nu} c_{i\mu} c_{i\nu}) f_i\\
&= \gamma m_0 a_0 \psi f_0 + \gamma m_0 \bar{a}_0 \mathrm{Tr}\Pi f_0 + \bar{a}\mathrm{Tr}\Pi \sum_{i>0} m_i f_i + e\Pi_{\mu\nu} \sum_{i>0} m_i f_i c_{i\mu} c_{i\nu} + b J_\mu \sum_{i>0} m_i f_i c_{i\mu}\\
&= \gamma m_0 a \psi f_0 + \gamma m_0 \bar{a}_0 \mathrm{Tr}\Pi f_0 + \bar{a}\mathrm{Tr}\Pi(\psi - m_0 f_0) + e(\Pi_{\mu\nu})^2 + b(J_\mu)^2
\end{aligned}$$

$$\begin{aligned}
A - B &= \gamma m_0 a_0^2 \psi^2 + 2\gamma m_0 a_0 \bar{a}_0 \psi \mathrm{Tr}\Pi + (\gamma m_0 \bar{a}_0 + \bar{a}^2 C_0 + e^2 C_4 + 2\bar{a} e C_2)(\mathrm{Tr}\Pi)^2\\
&\quad - \gamma m_0 a_0 \psi f_0 - \gamma m_0 \bar{a}_0 \mathrm{Tr}\Pi f_0 - \bar{a}\mathrm{Tr}\Pi + \bar{a} m_0 \mathrm{Tr}\Pi f_0 - e(\Pi_{\mu\nu})^2 - b(J_\mu)^2\\
&= \gamma m_0 a_0^2 \psi^2 + (2\gamma m_0 a_0 \bar{a}_0 - \bar{a})\mathrm{Tr}\Pi \psi + (\gamma m_0 \bar{a}_0 + \bar{a}^2 C_0) + e^2 C_4 + 2\bar{a} e C_2)(\mathrm{Tr}\Pi)^2\\
&\quad - \gamma m_0 a_0 \psi f_0 - (\gamma m_0 \bar{a}_0 - \bar{a} m_0)\mathrm{Tr}\Pi f_0
\end{aligned}$$

In order to suppress unwanted terms, we choose the D2Q7 lattice which possesses the property $\mathrm{Tr}\Pi = \Pi_{\mu\mu} = \sum_i m_i f_i c_{i\mu} c_{i\mu} = \psi - m_0 f_0$ since $|\boldsymbol{c}_i| = 1$

$$\begin{aligned}
A - B &= \gamma m_0 a_0^2 \psi^2 + (2\gamma m_0 a_0 \bar{a}_0 - \bar{a})\mathrm{Tr}\Pi + (...)(\mathrm{Tr}\Pi)^2 \\
&\quad -\gamma a_0 \psi(\psi - \mathrm{Tr}\Pi) - (\gamma \bar{a}_0 - \bar{a} m_0)\mathrm{Tr}\Pi(\psi - \mathrm{Tr}\Pi) \\
&= \underbrace{(\gamma m_0 a_0^2 - \gamma a_0)}_{0}\psi^2 + (2\gamma m_0 a_0 \bar{a}_0 - \bar{a} + \gamma a_0 - \gamma \bar{a}_0 + \bar{a} m_0)\mathrm{Tr}\Pi\psi \\
&\quad +(\gamma \bar{a}_0 - \bar{a} m_0 + \gamma m_0 \bar{a}_0 + \bar{a}^2 C_0 + e^2 C_4 + 2\bar{a} e C_2)(\mathrm{Tr}\Pi)^2
\end{aligned}$$

we therefore would like

$$\begin{aligned}
2\gamma \overbrace{m_0 a_0}^{1} \bar{a}_0 - \bar{a} + \gamma a_0 - \gamma \bar{a}_0 + \bar{a} m_0 &= 0 \\
\gamma \bar{a}_0 + \gamma a_0 - \bar{a} + \bar{a} m_0 &= 0 \\
\gamma(\bar{a}_0 + a_0) &= \bar{a}(1 - m_0) \\
\gamma &= \frac{\bar{a}(1 - m_0)}{\bar{a}_0 + a_0} \\
&= \frac{C_4 m_0 (m_0 - 1)}{C_0 C_4 - C_2^2}
\end{aligned}$$

and this must ensure that the last term is also killed

$$\begin{aligned}
\gamma \bar{a}_0 - \bar{a} m_0 + \gamma m_0 \bar{a}_0 + \bar{a} C_0 + \overbrace{e^2 C_4}^{-2\bar{a} e C_2} + 2\bar{a} e C_2 &= 0 \\
\gamma \bar{a}_0 (1 + m_0) - \bar{a} m_0 + \bar{a} C_0 + \bar{a} e C_2 &= 0 \\
\frac{\bar{a}\bar{a}_0 (1 - m_0^2)}{\bar{a}_0 + a_0} - \bar{a} m_0 + \bar{a} C_0 + \bar{a} e C_2 &= 0
\end{aligned}$$

which unfortunately we have not been able to simplify any further. We therefore step down and try the D2Q6 lattice for which the a_0, $\bar{a}_0$ and m_0 terms do not exist and hence for which $\mathrm{Tr}\Pi = \psi$. We are left with

$$A - B = (-\bar{a} + \bar{a}^2 C_0 + e^2 C_4 + 2\bar{a} e C_2)(\mathrm{Tr}\Pi)^2 \tag{2.172}$$

which vanishes since $\bar{a} = -\frac{1}{2C_2}$, $e = \frac{1}{2C_4}$, $C_0 = 6$, $C_2 = 4$, $C_4 = 3/4$, see [14].

The above local equilibrium has therefore been numerically tested. For an unexplained reason, the scheme is stable only if the dynamics is coded explicitly for each f. Indeed, instead of coding the collision term of the dynamic with $f_i' = 2(f_i^{(0)} - f_i)$ where $f_i^{(0)}$ is computed separately as given in equation (2.146), we have to explicitly develop the collision term for each f_i. In a matrix form this corresponds to

$$\begin{pmatrix} f_1(t+1) \\ f_2(t+1) \\ f_3(t+1) \\ f_4(t+1) \\ f_5(t+1) \\ f_6(t+1) \end{pmatrix} = \frac{1}{3} \begin{pmatrix} 2 & 1 & -1 & 1 & -1 & 1 \\ 1 & 2 & 1 & -1 & 1 & -1 \\ -1 & 1 & 2 & 1 & -1 & 1 \\ 1 & -1 & 1 & 2 & 1 & -1 \\ -1 & 1 & -1 & 1 & 2 & 1 \\ 1 & -1 & 1 & -1 & 1 & 2 \end{pmatrix} \begin{pmatrix} f_1(t+1) \\ f_2(t+1) \\ f_3(t+1) \\ f_4(t+1) \\ f_5(t+1) \\ f_6(t+1) \end{pmatrix} \tag{2.173}$$

At this point, the road to follow consists in checking the exact form of the continuity equations (2.124) and (2.125) through the Chapman-Enskog procedure to then see whether the macroscopic equation which results is the Navier equation. As a concluding remark on the potential of this model, it is possible to say that given the fact that no rest population f_0 exist in the D2Q6 lattice, it seems difficult to obtain a model where the speed of sound is a free parameter and hence also the elastic coefficients. The exact practical limitations would probably show up once a explicit implementation of the scheme to model elasticity is achieved.

2.7 Conclusion

In this chapter, we have presented several studies concerning the development of a lattice Boltzmann scheme to model linear elasticity. The chapter started with presenting the original cellular automata model which have served as an inspiration to push the modelling into the lattice Boltzmann formalism. The first model proposed is based on the use of the lattice Boltzmann wave formalism. Its use, in several contexts, perfectly illustrate the stakes which would be at hand if the same success as the lattice Boltzmann model has had for fluid dynamics were achieved. Indeed, we have seen that the intuitive and numerically efficient approach of the Boltzmann formalism can bring light to subjects as diverse as fracture dynamics, fragmentation and mechanical contact problems, even though certain theoretical limitations yet impede the scheme to be a mature application tool. To overcome these limitations, we have explored two directions which constitute an attempt at directly modelling the Navier equation of linear elasticity. The success of these attempts is partial and there remains certain theoretical validation to be done. Finally, should this latest approach finally yield the expected results, the reward is very clear: the lattice Boltzmann method and community would be able to fully step in the field of classical solid dynamics and henceforth solve very challenging problems.

Chapter 3

Incompressible Fluids

3.1 Introduction

Fluid dynamics is concerned with a range of different problems ranging from hydrostatic to thermal fluids. An important problem though consists in the study of incompressible fluids for the simple reason that many important fluids such as water show negligible compressibility. This assumption simplifies the equation without reducing their complexity and results in the famous Navier-Stokes equation. Therefore, it is expected from any numerical scheme to be able to satisfy this condition. Classical lattice Boltzmann models [17] do have a small residual compressibility which has even been used to model compressible fluids [18]. While this compressibility has always been considered negligible, it yet may be relevant to the numerical precision of unsteady flows and to physical basis when modelling certain processes such as fluids with gravity. It is thus of interest to improve the incompressibility assumption of the classical lattice Boltzmann scheme. The attempts at having a truly incompressible numerical scheme have in the past been either to redefine the physical quantities to be modeled which results in a loss of generality or to make use of some artificial numerical trick without a clear physical basis. We propose here to model incompressibility by introducing in the Boltzmann numerical scheme an additional term based on the microscopic behavior of a fluid namely a repulsive force akin to the repulsive part of the van der Waals potential. By doing so, we are able to tune the compressibility of the fluid and theoretically reach the limit of incompressibility. This technique clearly illustrates the capacity of the Boltzmann modelling to easily and intuitively incorporate additional behaviors in a model by directly introducing the microscopic ingredients to be modeled.

This chapter is divided as follow. First, an overview of the theory of incompressible fluids [19] and a short overview of the lattice Boltzmann model for fluid dynamics is given. Then, two models which improve the incompressible assumption of lattice Boltzmann fluids are reviewed. We then present our model and validate the scheme with the modelling of a Poiseuille flow and a Womersley flow which is an unsteady flow. The model is then applied to the case of a fluid in a gravity field. Finally, we conclude by reassessing the main achievement and the limits of our model.

3.2 Theory

The mathematical study of the motion of fluids is expressed in terms of the velocity field of the fluid

$$\boldsymbol{u} = \boldsymbol{u}(\boldsymbol{r}, t) \tag{3.1}$$

and two of its thermodynamic quantities, usually pressure and density

$$p = p(\boldsymbol{r}, t) \tag{3.2}$$

$$\rho = \rho(\boldsymbol{r}, t) \tag{3.3}$$

The conservation of matter is then expressed through the continuity equation

$$\frac{\partial \rho}{\partial t} + \nabla \cdot \rho \boldsymbol{u} = 0 \tag{3.4}$$

which simply expresses that the variation of matter is given by the flow of momentum. If the fluid is incompressible, then $\rho = \mathrm{const}$ and this equation simplifies to $\nabla \cdot \boldsymbol{u} = 0$. In order to obtain an equation of motion, we now introduce a force on an element of fluid.

3.2.1 The Euler equation

The total force on a volume can be shown to be equal to $-\nabla p$ and thus we can apply Newton's law on an unit element of fluid with mass ρ and obtain

$$\rho \frac{d\boldsymbol{u}}{dt} = -\nabla p \tag{3.5}$$

where $d\boldsymbol{u}/dt$ is the acceleration of an element of fluid. Since the representation of the motion is given for fixed positions in space and time, this acceleration takes the form

$$\frac{d\boldsymbol{u}}{dt} = \frac{\partial \boldsymbol{u}}{\partial t} + (\boldsymbol{u}\nabla)\boldsymbol{u} \tag{3.6}$$

which takes into account the variation in time as well as space. Equation (3.5) now becomes

$$\frac{\partial \boldsymbol{u}}{\partial t} + (\boldsymbol{u}\nabla)\boldsymbol{u} = -\frac{1}{\rho}\nabla p \tag{3.7}$$

which is Euler's equation for a perfect fluid (1755). By perfect, it is meant that there has been no dissipation of energy due to either friction or thermal exchange between elements of fluid. In order to later introduce such terms, it is convenient to reformulate Euler's equation[1] in terms of the momentum of fluid $\rho\boldsymbol{u}$ instead of the velocity field $\boldsymbol{u}$

$$\frac{\partial \rho u_i}{\partial t} = -\frac{\partial \Pi_{ik}}{\partial r_k} \tag{3.8}$$

where

$$\Pi_{ik} = p\delta_{ik} + \rho u_i u_k \tag{3.9}$$

is the momentum tensor flux and represents the flow of momentum in the fluid. The first term thus represents the transport of momentum due to pressure while the second is the transport of momentum due to the direct transport of particles.

3.2.2 The Navier-Stokes equation

In order to study viscous fluids, it is necessary to introduce an additional viscous term in momentum tensor flux. This contribution thus represents the friction of fluid elements in motion. The momentum tensor flux takes the form

$$\Pi_{ik} = p\delta_{ik} + \rho u_i u_k - \sigma'_{ik} \tag{3.10}$$

and considering a linear dependency with regards to the velocity gradients, the most general stress tensor σ'_{ik} which is rotation invariant is

$$\sigma'_{ik} = \eta\left(\frac{\partial u_i}{\partial r_k} + \frac{\partial u_k}{\partial r_i} - \frac{2}{3}\delta_{ik}\frac{\partial u_l}{\partial r_l}\right) + \xi\delta_{ik}\frac{\partial u_l}{\partial r_l} \tag{3.11}$$

where η and ξ are the viscosity coefficients of a fluid. In general, they are functions of pressure and temperature. In practice, however, their variation is negligible and the equation of motion can be written as

$$\frac{\partial \boldsymbol{u}}{\partial t} + (\boldsymbol{u}\nabla)\boldsymbol{u} = -\frac{1}{\rho}\nabla p + \frac{1}{\rho}\eta\nabla^2\boldsymbol{u} + \frac{1}{\rho}(\xi + \frac{\eta}{3})\nabla(\nabla\cdot\boldsymbol{u}) \tag{3.12}$$

which is the compressible equation of motion of a viscous fluid. Now, if one considers an incompressible fluid, i.e. $\nabla\cdot\boldsymbol{u} = 0$, the equation simplifies to

$$\frac{\partial \boldsymbol{u}}{\partial t} + (\boldsymbol{u}\nabla)\boldsymbol{u} = -\frac{1}{\rho}\nabla p + \nu\nabla^2\boldsymbol{u} \tag{3.13}$$

which is the Navier-Stokes equation and $\nu = \eta/\rho$ is the kinematic viscosity.

[1] using Einstein's convention of summation over repeated indices.

3.2.3 Conditions for incompressibility

We have seen that the incompressibility assumption simplifies the equation of motion of a viscous fluid by removing terms in the Navier-Stokes equation of motion and reducing the number of viscosity coefficients from two to one. It is therefore important to consider when exactly this assumption holds true. The main point is to look at the variation of density due to a variation of pressure

$$\Delta\rho = \left(\frac{\partial\rho}{\partial p}\right)\Delta p \tag{3.14}$$

In a fluid, the quantity $(\partial p/\partial\rho)$ can be shown to be equal to the square of the speed of sound waves [19]. Thus, we have

$$\Delta\rho = \frac{1}{c_s^2}\Delta p \tag{3.15}$$

In the case of a steady flow, it follows from Bernouilli's equation[19] that the variation of pressure is of the order of $\Delta p \sim \rho v^2$ and we are therefore left with

$$\Delta\rho \sim \rho\frac{v^2}{c_s^2} \tag{3.16}$$

which means that

$$\frac{\Delta\rho}{\rho} \sim O(M^2) \tag{3.17}$$

where $M = v/c_s$ is the Mach number by definition. Since the fluid can be considered as incompressible if $\Delta\rho/\rho \ll 1$, this therefore corresponds to the low Mach number regime. Physically, this means that the velocity of the fluid is much lower than the speed of sound in the fluid.

We next have to look at the case of an unsteady flow. The velocity field itself is in motion and therefore an additional condition must be satisfied. First, we introduce the characteristic length l and time τ of the changes in the velocity field. Following [19] the Euler equation (3.7) allows to compare the $\partial\boldsymbol{u}/\partial t$ and $\nabla p/\rho$ terms and the pressure variation is then of the order of

$$\Delta p \sim \frac{l}{\tau}\rho v \tag{3.18}$$

Thus, from equation (3.15), the corresponding variation of density is

$$\Delta\rho \sim \frac{l\rho v}{\tau c_s^2} \tag{3.19}$$

For an incompressible fluid, the density change $\partial\rho/\partial t$ can be considered negligible. Considering the continuity equation (3.4), this translates to

$$\frac{\Delta\rho}{\tau} \ll \rho\frac{v}{l} \tag{3.20}$$

which together with equation (3.19) finally yields

$$\tau \gg \frac{l}{c_s} \tag{3.21}$$

This limit means that, in an incompressible fluid, the time needed for a sound wave to travel the distance l is small with regards to the time τ during which the motion of the fluid has sensibly changed. Thus, the propagation of interactions in the fluid can be considered as instantaneous.

In conclusion, it is important to say that the above conditions (3.17) and (3.21) are in fact only limits of incompressibility and hence the simplification, $\nabla\cdot\boldsymbol{u} = 0$, which leads to the the Navier-Stokes equation must not be considered exact. The notion of incompressibility is therefore sometimes abusing and the model presented in this section will precisely illustrate a mechanism which show how to reach for the asymptotic behavior. In addition, there is the notable fact that all this discussion is valid when no external force is present in the fluid. Indeed, a perfect example of fluid which obeys the Navier-Stokes equation and is nevertheless compressible is given by the atmosphere which is a fluid under gravity.

3.2.4 Lattice Boltzmann model of a fluid

Lattice Boltzmann models are the discrete and numerical equivalent of the Boltzmann equation of transport from the continuum theory of statistical mechanics [20]. We briefly summarize here the essential notions of such a model when modelling fluids dynamics. The discrete Boltzmann equation of transport is given as

$$f_i(\boldsymbol{r} + \Delta_t\boldsymbol{v}_i, t + \Delta_t) - f_i(\boldsymbol{r}, t) = \Omega(f_i) \tag{3.22}$$

where f_i is the density distribution of particles in direction i and Ω is the collision operator. Space and time are discrete. Space points are connected together through a geometry or lattice whose direction vectors form the set $\{\boldsymbol{v}_i\}$ as illustrated on figure 3.1.

The dynamics of the discrete Boltzmann equation can be seen as a series of collisions and propagation where the collision computes the new values of the f_i through the collision operator Ω_i and the propagation consist in streaming of the new quantities to the neighboring lattice positions. The physics of the process under study is then completely contained in the collision term. This constitutes

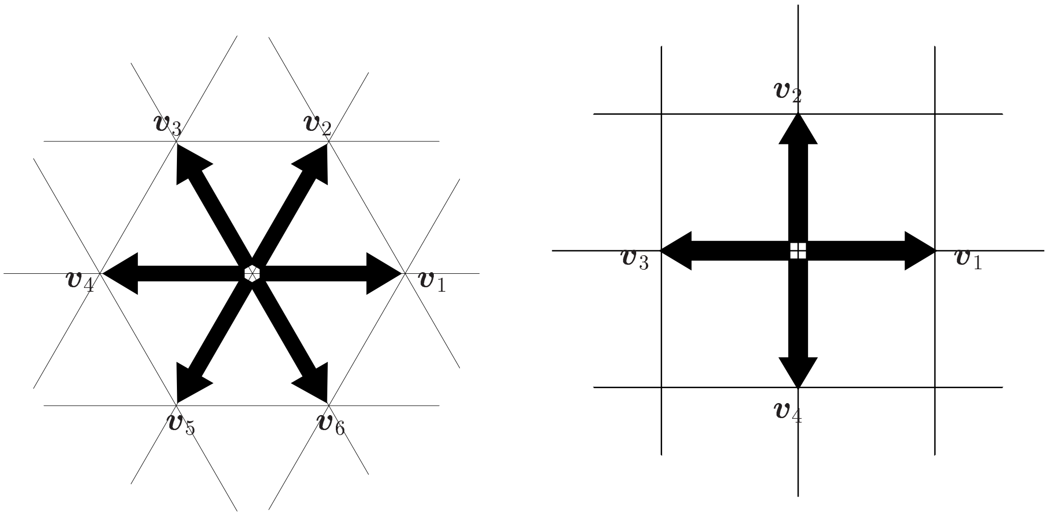

Figure 3.1: The base vectors of a D2Q7 or hexagonal lattice. The population of rest particles, i.e. the particles which do not propagate, are associated with direction $\boldsymbol{v}_0 = 0$ which is the label for the site itself.

the microscopical modelling and in order to validate the microscopical rules it is necessary to show that at a scale where $T \gg \Delta_t$ and $\text{Ł} \gg \Delta_r$, the correct macroscopic equation is recovered. This validation is usually obtained through the Chapman-Enskog procedure [21].

A popular way of giving the collision term Ω_i is actually to write it as a relaxation to a local equilibrium distribution function $f_i^{(0)}$

$$f_i(\boldsymbol{r} + \Delta_t \boldsymbol{v}_i, t + \Delta_t) - f_i(\boldsymbol{r}, t) = \frac{1}{\tau}\left(f_i^{(0)} - f_i(\boldsymbol{r}, t)\right) \tag{3.23}$$

which hence contains the appropriate physics. This is the BGK-formulation [15] [22] of the lattice Boltzmann equation. The equilibrium function $\boldsymbol{f}_i^{(0)}$ describing an incompressible fluid with the lattice Boltzmann formalism is

$$f_i^{(0)} = \rho\left[\frac{1}{C_2}\frac{c_s^2}{v^2} + \frac{1}{C_2}\frac{\boldsymbol{v}_i \cdot \boldsymbol{u}}{v^2} + \frac{1}{2}\frac{1}{C_4 v^4}\left(v_{i\alpha}v_{i\beta} - v^2\frac{C_4}{C_2}\delta_{\alpha\beta}\right)u_\alpha u_\beta\right] \tag{3.24}$$

$$m_0 f_0^{(0)} = \rho\left[1 - \frac{C_0}{c_2}\frac{c_s^2}{v^2} + \left(\frac{C_0}{2C_2} - \frac{C_2}{2C_4}\right)\frac{u^2}{v^2}\right] \tag{3.25}$$

where

$$\rho = \sum_{i \geq 0} m_i f_i \tag{3.26}$$

Models	i	$\vert\boldsymbol{v}_i\vert$	m_i	C_0	C_2	C_4	c_s^2
D2Q7	0..7	v_l	1	6	3	3/4	1/4
D2Q9	0..4	v_l	4	20	12	4	1/3
	5..8	$\sqrt{2}v_l$	1				

Table 3.1: Constants of the most common $DdQ(z+1)$ lattices where d is the spatial dimension and z is the number of link, v_i is the velocity on link i and m_i are the weights associated to each link.

is the density of the fluid and

$$\rho\boldsymbol{u} = \sum_{i>0} m_i f_i \boldsymbol{v}_i \tag{3.27}$$

is the momentum of the fluid at site $\boldsymbol{r}$. These quantities are the collision invariants and are the direct expression of conservation of mass and momentum. The m_i quantities are lattice weights whose values depend on the choice of the lattice topology in order to obtain the correct macroscopic equation. The constant C_0, C_2, C_4 are also lattice dependent and are defined as

$$C_0 = \sum_{i>0} m_i \tag{3.28}$$

$$C_2 v^2 \delta_{\alpha\beta} = \sum_{i>0} m_i v_{i\alpha} v_{i\beta} \tag{3.29}$$

$$C_4 v^2 \delta_{\alpha\beta\gamma\delta} = \sum_{i>0} m_i v_{i\alpha} v_{i\beta} v_{i\gamma} v_{i\delta} \tag{3.30}$$

Additionally, c_s^2 is an adjustable parameter corresponding to the speed of sound wave in the fluid. The Chapman-Enskog procedure [14] then leads to the following macroscopic equation

$$\begin{aligned}\partial_t \rho u_\alpha + \rho u_\beta \partial_\beta u_\alpha + u_\alpha \mathrm{div}\rho\boldsymbol{u} = &- c_s^2 \partial_\alpha \rho + \Delta_t v^2 \frac{C_4}{C_2}\left(\tau - \frac{1}{2}\right) \\ &+ \Delta_t v^2 \left(\tau - \frac{1}{2}\right)\left[2\frac{C_4}{C_2} - \frac{c_s^2}{c^2}\right] \partial_\alpha \mathrm{div}\rho\boldsymbol{u}\end{aligned} \tag{3.31}$$

which in the case of an incompressible fluid where $\mathrm{div}\rho\boldsymbol{u} = 0$ (at low Mach number for instance) reduces to the usual Navier-Stokes equation

$$\partial_t \boldsymbol{u} + (\boldsymbol{u}\cdot\nabla)\boldsymbol{u} = -\frac{1}{\rho}\nabla P + \nu\nabla^2\boldsymbol{u} \tag{3.32}$$

where $\nu = C_4/C_2(\tau - \frac{1}{2})$ is the viscosity of the fluid. It is adjustable through the relaxation time with a singularity at $\tau = 1/2$ which corresponds to zero viscosity and is numerically unstable. The various constant values for popular lattice topology illustrated in figure 3.1 are given in table 3.1.

With respect to the subject of this chapter, let us conclude by saying that numerically speaking the assumption of incompressibility is not completely verified, although the density gradient is small. The lattice Boltzmann scheme can then be considered as a model for compressible flows and such has been the case in the past [18]. The study of the incompressibility of the lattice Boltzmann scheme therefore remains a subject for research and justifies the work presented in this chapter.

3.3 State of the Art

3.3.1 The lattice Boltzmann pressure model

This model [17] proposes to directly model the pressure as the dynamical quantity of the Boltzmann equation. It first starts by noting that if one takes the equilibrium function for fluids

$$f_i^{(0)} = w_i \rho \left(1 + 3\frac{(\boldsymbol{v}_i \cdot \boldsymbol{u})}{c_s^2} + \frac{9}{2}\frac{(\boldsymbol{v}_i \cdot \boldsymbol{u})^2}{c_s^4} - \frac{3}{2}\frac{\boldsymbol{u}^2}{c_s^2} \right) \tag{3.33}$$

where $w_0 = 4/9$, $w_{1,2,3,4} = 1/9$ and $w_{5,6,7,8} = 1/36$ and which is an equivalent formulation of equation (3.24). Since the fluid is considered incompressible, by explicitly replacing the density with $\rho = \bar{\rho} + \delta\rho$, then one can neglect terms in $\delta\rho(\boldsymbol{u}/c_s)$ and $\delta\rho(\boldsymbol{u}/c_s)^2$ which are of the order $O(M^3)$ or higher in the Mach number ($\delta\rho$ should be of the order $O(M^2)$ in an incompressible fluid). The equilibrium density distribution thus becomes

$$f_i^{(0)} = w_i \left[\rho + \bar{\rho} \left(3\frac{(\boldsymbol{v}_i \cdot \boldsymbol{u})}{c_s^2} + \frac{9}{2}\frac{(\boldsymbol{v}_i \cdot \boldsymbol{u})^2}{c_s^4} - \frac{3}{2}\frac{\boldsymbol{u}^2}{c_s^2} \right) \right] \tag{3.34}$$

The model then changes of representation by introducing the variables

$$p_i = c_s^2 f_i \tag{3.35}$$

since it is common to use the pressure as the independent variable in the incompressible Navier-Stokes equation. The lattice Boltzmann BGK equation thus becomes

$$p_i(\boldsymbol{r} + \Delta_t \boldsymbol{v}_i, t + \Delta_t) - p_i(\boldsymbol{r}, t) = \frac{1}{\tau}\left(p_i^{(0)}(\boldsymbol{r}, t) - p_i(\boldsymbol{r}, t) \right) \tag{3.36}$$

and together with

$$p_i^{(0)} = w_i \left[p + \bar{p} \left(3\frac{(\boldsymbol{v}_i \cdot \boldsymbol{u})}{c_s^2} + \frac{9}{2}\frac{(\boldsymbol{v}_i \cdot \boldsymbol{u})^2}{c_s^4} - \frac{3}{2}\frac{\boldsymbol{u}^2}{c_s^2} \right) \right] \tag{3.37}$$

they constitute the incompressible lattice Boltzmann model. In this representation, the pressure and velocity are now given by

$$p = \sum_i p_i \tag{3.38}$$

$$p\boldsymbol{u} = \sum_i \boldsymbol{v}_i p_i \tag{3.39}$$

Given all the above definitions, one can go through the Chapman-Enskog procedure and finally obtain the incompressible Navier-Stokes equations

$$\frac{1}{c_s^2}\frac{\partial P}{\partial t} + \nabla \cdot \boldsymbol{u} = 0 \tag{3.40}$$

$$\frac{\partial \boldsymbol{u}}{\partial t} + \boldsymbol{u} \cdot \nabla \boldsymbol{u} = -\nabla P + \nu \nabla^2 \boldsymbol{u} \tag{3.41}$$

with $P = p/\bar{\rho}$ and the kinetic viscosity is given by

$$\nu = \frac{(2\tau - 1)}{6}\frac{\Delta_r^2}{\Delta_t} \tag{3.42}$$

Equation (3.41) is the incompressible Navier-Stokes equation while the physical meaning of equation (3.40) is not clear. Writing it in dimensionless form, though, yields

$$\frac{1}{T}\frac{\partial P'}{\partial t'} + \frac{c_s}{L}\nabla' \cdot \boldsymbol{u}' = 0 \tag{3.43}$$

where $P' = P/c_s^2$, $t' = t/T$, $\nabla' = L\nabla$, $\boldsymbol{u}' = \boldsymbol{u}/c_s$ and L and T are respectively the characteristic length and time, which leads to the incompressible condition for a steady flow $\partial P/\partial t = 0$

$$\nabla \cdot \boldsymbol{u} = 0 \tag{3.44}$$

which is therefore exactly satisfied by the numerical scheme. Physically then, this means that the condition $M \ll 1$ is sufficient to obtain an incompressible scheme for a steady flow and such is considered the case in most simulations. For an unsteady flow, we have seen that the following condition must also be satisfied

$$T \gg L/c_s \tag{3.45}$$

which therefore give a limit on the characteristic time, T, for the fluid to undergo a macroscopic change and henceforth also on any force driving the flow.

The numerical simulations performed are a steady flow, the plane Poiseuille flow, and an unsteady flow, the Womersley flow, and are shown to achieve machine precision. We can then consider that this method is able to correctly simulate the equation of motion of an incompressible fluid by redefining velocity. By doing so however, the scheme losses any reference to the density of the fluid which in many applications, such as immiscible fluids, is necessary. Furthermore, the microscopic interpretation of the p_i fields is somehow left behind. For these reasons, we believe it is therefore still necessary to try to propose a more physical mechanism to achieve incompressibility of the original lattice Boltzmann scheme.

3.3.2 The sound speed feedback technique

This method, which in the original paper [23] is described in slightly different terms, is based on the observation that current lattice Boltzmann models produce pressure gradients through density gradients. Indeed, the pressure of a lattice Boltzmann scheme is given by

$$p = c_s^2 \rho \tag{3.46}$$

and therefore any change in pressure directly produces a change in density. Since, in the lattice Boltzmann model, the speed of sound c_s^2 is in fact a free parameter, the authors suggest to use it absorb the change in density due to a change in pressure. In practical terms, this is best understood by rewriting the local equilibrium (3.24) in the following form

$$f_i^{(0)} = a\rho + \frac{b}{v^2}\rho \boldsymbol{v}_i \cdot \boldsymbol{u} + e\frac{u^2}{v^2}\rho + \frac{h}{v^2}\rho v_{i\alpha} v_{i\beta} u_\alpha u_\beta \qquad i \geq 1 \tag{3.47}$$

$$f_0^{(0)} = a_0\rho + e_0\frac{u^2}{v^2}\rho \tag{3.48}$$

where a, b, e, h, a_0, e_0 are constants to be determined by the conservation laws and the Chapman-Enskog procedure. The local equilibrium (3.24), in fact, is the expression where these constants have been determined. Thus, the conservation of mass and momentum, for instance, respectively lead to the following constraints

$$m_0 a_0 + C_0 a = 1 \tag{3.49}$$

and

$$c_s^2 = a C_2 v^2 \tag{3.50}$$

This means that by locally perturbing, through equation (3.49), the ratio a_0/a which controls the ratio between rest particles and moving particles, we in fact change, through equation (3.50), the value of the speed of sound and consequently control the pressure without changing the density. The authors thus propose to obtain a zero density gradient by using a feedback loop technique on the value of the speed of sound. The value of a and hence the speed of sound is given by

$$a = a_0 + s(\rho, \tau) \tag{3.51}$$

where the function $s(\rho, \tau)$ is

$$s(\rho, \tau) = -b(\tau)\left(1 - \frac{\rho}{\rho_0}\right) \tag{3.52}$$

with $b(\tau)$ a well chosen constant and ρ_0 the target density. This feedback loop technique thus adjusts at each time step the ratio of rest and moving particles until the target density is reached while having imposed a given velocity, thus a pressure. The choice of the constant $b(\tau)$ is done so as to not introduce numerical instabilities. The critical value b_c is established numerically by the authors. The model is validated for the cases of both a steady flow, Poiseuille flow, and an unsteady flow, Womersley flow. Velocity fields for both flows are completely recovered and the density gradient is seen to decrease exponentially after a few time steps.

This numerical model thus achieves nearly constant density with the lattice Boltzmann method. The question, however, is whether the technique is acceptable from a physical point of view. Indeed, real fluids do not locally adjust their speed of sound in order to be incompressible. The scheme does not therefore give a better understanding of the physics involved in an incompressible fluid.

3.4 The repulsive force model

We use the traditional D2Q9 model with body force. Thus, the lattice Boltzmann equation with the BGK formulation is

$$f_i(\boldsymbol{r} + \Delta_t \boldsymbol{v}_i, t + \Delta_t) - f(\boldsymbol{r}, t) = \frac{1}{\tau}\left(f_i^{(0)}(\boldsymbol{r}, t) - f_i(\boldsymbol{r}, t)\right) + \frac{\Delta_t}{v^2 C_2}\boldsymbol{F} \cdot \boldsymbol{v}_i \tag{3.53}$$

and the local equilibrium is

$$f_i^{(0)} = \rho\left[\frac{1}{C_2}\frac{c_s^2}{v^2} + \frac{1}{C_2}\frac{\boldsymbol{v}_i \cdot \boldsymbol{u}}{v^2} + \frac{1}{2}\frac{1}{C_4 v^4}\left(v_{i\alpha}v_{i\beta} - v^2\frac{C_4}{C_2}\delta_{\alpha\beta}\right)u_\alpha u_\beta\right] \tag{3.54}$$

$$m_0 f_0^{(0)} = \rho\left[1 - \frac{C_0}{C_2}\frac{c_s^2}{v^2} + \left(\frac{C_0}{2C_2} - \frac{C_2}{2C_4}\right)\frac{u^2}{v^2}\right] \tag{3.55}$$

which following the Chapman-Enskog procedure [14] and granted the incompressibility assumption $\nabla \cdot \boldsymbol{u} = 0$ results in the Navier-Stokes equation

$$\partial_t \boldsymbol{u} + (\boldsymbol{u} \cdot \nabla)\boldsymbol{u} = -\frac{1}{\rho}\nabla P + \nu_{lb}\nabla^2 \boldsymbol{u} + \frac{\boldsymbol{F}}{\rho} \tag{3.56}$$

Numerically however, the relation $\nabla \cdot \boldsymbol{u} = 0$ is not verified by the lattice Boltzmann model even though the density gradient is often considered negligible. We propose below to improve the incompressibility of the lattice Boltzmann model by introducing a repulsive force between lattice sites. The physical reason is to be found in the repulsive part of the van der Waals potential existing between the molecules forming the fluid.

3.4.1 Repulsive body force, pressure and compressibility

In order to simulate an incompressible fluid, we introduce a body force which represents the repulsive part of the traditional Van der Waals potential between fluids particles. We thus define a non-local body force between neighboring lattice sites. The force must be symmetric between sites and following the techniques used in [24] we write

$$\boldsymbol{F} = -W\rho(\boldsymbol{r})\sum_k \rho(\boldsymbol{r}+\Delta_t\boldsymbol{v}_k)\Delta_t\boldsymbol{v}_k \tag{3.57}$$

where W is a positive constant and therefore the interaction force is repulsive which is not the original purpose of the model proposed in [24]. Since at first order[2]

$$\begin{aligned}
\boldsymbol{F} &= -W\rho(\boldsymbol{r})\sum_k \rho(\boldsymbol{r}+\Delta_t\boldsymbol{v}_k)\Delta_t\boldsymbol{v}_k \\
&= -W\rho(\boldsymbol{r})\sum_k \left[\rho(\boldsymbol{r})+\Delta_t\boldsymbol{v}_k\cdot\nabla\rho(\boldsymbol{r})\right]\Delta_t\boldsymbol{v}_k \\
&= -W\rho(\boldsymbol{r})\sum_k \left[\Delta_t\boldsymbol{v}_k\cdot\nabla\rho(\boldsymbol{r})\right]\Delta_t\boldsymbol{v}_k \qquad \left(\sum_k \rho(\boldsymbol{r})\Delta_t\boldsymbol{v}_k = 0\right) \\
&= -W\Delta_t^2 C_2' v^2\rho(\boldsymbol{r})\nabla\rho(\boldsymbol{r}) \\
&= -\frac{1}{2}W\Delta_t^2 C_2' v^2\nabla\rho(\boldsymbol{r})^2
\end{aligned}$$

the body force term can be absorbed in the pressure term of the Navier-Stokes equation (3.56) and thus the state equation can be written as

$$p = c_s^2\rho + \frac{1}{2}W\Delta_t^2 C_2'\rho(\boldsymbol{r})^2 \tag{3.58}$$

We therefore expect the density gradient to behave as

$$\nabla\rho = \frac{\nabla p}{(c_s^2 + W\Delta_t C_2'\rho)} \tag{3.59}$$

[2]The C_2' factor arises from the fact that the force contains the tensor $\sum_i v_{i\alpha}v_{i\beta}$ instead of the usual $\sum_i m_i v_{i\alpha}v_{i\beta}$. A simple calculation shows that $C_2' = 6$

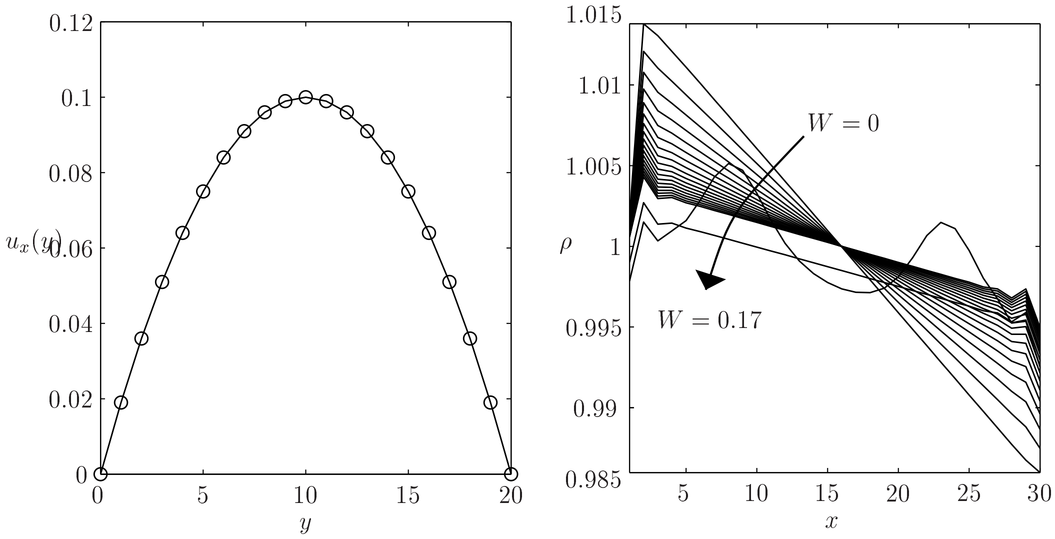

Figure 3.2: The Poiseuille flow velocity profile with repulsive force coupling constant $W = 0.17$. The velocity is unaffected by the addition of the repulsive force (left). The evolution of the mean density profile along the longitudinal direction (right); as the value of the coupling constant W of the repulsive body force between lattice sites increases, the gradient of the density profile decreases thus illustrating the convergence to incompressibility achieved by the scheme, see figure 3.3.

which for $W \to \infty$ converges to zero. Furthermore, we now obtain an expression for the compressibility

$$K = \left(\frac{\partial p}{\partial \rho}\right)^{-1} = \left(c_s^2 + W \Delta_t^2 C_2' \rho(\boldsymbol{r})\right)^{-1} \tag{3.60}$$

and see that the compressibility arbitrarily goes to zero when $W \to \infty$, namely any small variation in density ρ will produce a significantly larger change in pressure p. This theoretical result will have to be reconsidered in the light of the simulations where numerical instabilities will impose a practical limit to the method.

3.5 Numerical experiments

In order to validate our approach, we look at a steady flow, Poiseuille flow, and an unsteady flow, Womersley flow. We then apply the model to a fluid at rest under gravity. All simulations are effectuated with a 30×21 D2Q9 lattice and $\tau = 1.0$. The fluid is initiated with zero velocity $\boldsymbol{u} = 0$ and initial density $\rho_0 = 1.0$. Unless otherwise specified, the measurements are all done after 2000 iterations. At wall,

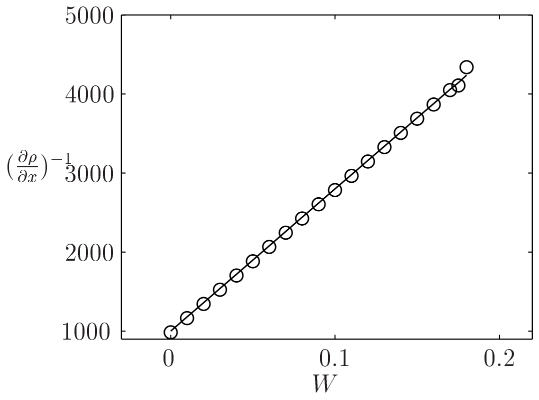

Figure 3.3: The density gradient along the longitudinal direction of a Poiseuille flow as a function of the coupling constant W of the repulsive force between sites. We see that the artificial density gradient is reduced by a factor 3 of the original value. Higher values of W are not reachable for numerical instability reasons.

we apply the Inamuro border conditions [25] and do not apply the repulsive body force.

3.5.1 Poiseuille flow.

In order to drive the flow, we make use of a constant body force $F = 10^{-2}$ at the inlet. It is shown [26] that this technique creates a pressure gradient $\nabla p = F/L$ where L is the length of the pipe. The flow is therefore not driven by a change in density. However, since the lattice Boltzmann scheme is not completely incompressible, the flow resulting from this technique has a density gradient. To validate our modelling of the incompressibility of the fluid, we thus look at the effect of the repulsive force on this residual density gradient. The velocity profiles are unaffected by the repulsive force as can be seen on figure 3.2 (left). The various density profiles for increased values of W are shown on figure 3.2 (right). We see that the density profile converges to a zero gradient situation as W increases. The oscillating profile, for which $W_{\max} = 0.17$, is the last profile before numerical instabilities appear. The agreement between density gradient $\nabla\rho$ and coupling constant W given by equation (3.59) is shown on figure 3.3. The plot is obtained by measuring the density gradient along the channel put apart for the values at the inlet. We see that except for the value at $W_{\max}$ the agreement is very good. The global residual gradient $\partial_x\rho/\rho$ is thus reduced from 0.1% to 0.03%. The scheme thus achieves a reduction of the residual density gradient by roughly a factor 3.

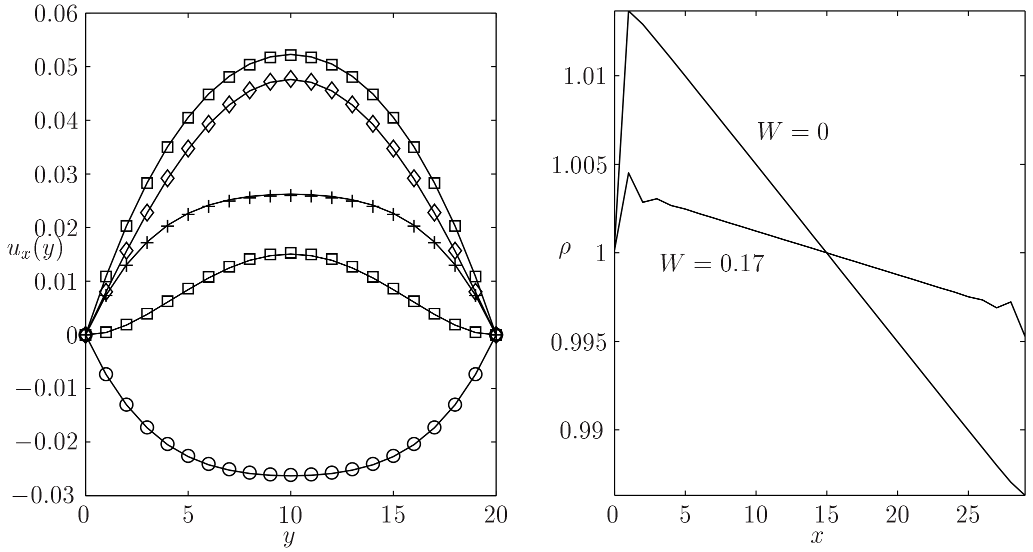

Figure 3.4: (left) The Womersley flow velocity profile $u_x(y,t)$ across the channel at times $T/8$, $T/4$, $3T/8$ and $T/2$. The frequency of the drive is $\omega = 2\pi/T$ with $T = 1000$ and the Womersley number is thus $\alpha = 0.7$ (right) The residual density gradient along the channel for $W = 0.0$ and $W_{\max} = .017$.

3.5.2 Womersley flow

The setup of the Womersley flow is identical to a Poiseuille flow except that the flow is now driven with a time periodic pressure gradient at the inlet of the channel. Assuming that the flow is laminar, i.e. $\boldsymbol{u} = (u_x, 0)$ and $\partial_x u_x = 0$, the Navier-Stokes equation reduces to

$$\frac{\partial u_x}{\partial t} = -\frac{\partial P}{\partial x} + \nu \frac{\partial^2 u_x}{\partial y^2} \tag{3.61}$$

where the pressure gradient is given by

$$\frac{\partial P}{\partial t} = \mathrm{Re}(Ae^{i\omega t}) \tag{3.62}$$

and A and ω are respectively the amplitude and frequency. The solution [27] [17] of the above equation is

$$u_x(y,t) = \mathrm{Re}[i\frac{A}{\omega}\left(1 - \frac{\cos(\lambda(2y/L_y - 1))}{\cos(\lambda)}\right)e^{i\omega t}] \tag{3.63}$$

where λ is given in terms of the Womersley number α

$$\lambda^2 = -i\alpha^2 \qquad \alpha^2 = \frac{D^2\omega}{4\nu} \tag{3.64}$$

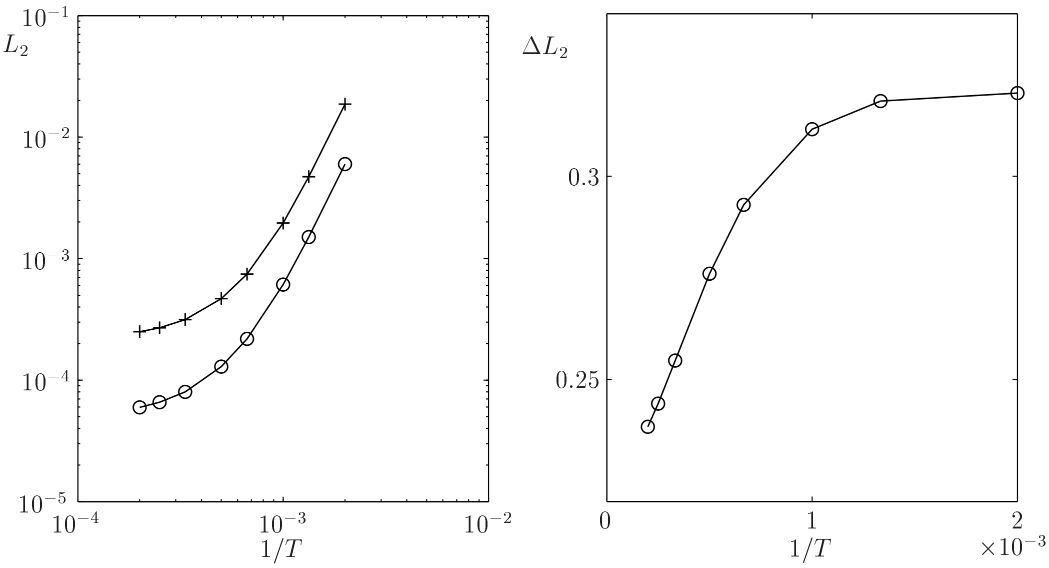

Figure 3.5: (left) The relative global error as a function of frequency of the pressure gradient. The upper curve is obtained with $W = 0.0$ while the lower curve is for $W_{\max} = 0.17$. The value of the error mostly due to the value at the inlet. Therefore, the ratio of the errors (right) shows the improvement due to the incompressible scheme. At low frequencies, the error is thus reduced down to 25% of its original value.

where D is the channel width. As for the Poiseuille flow, the pressure gradient is achieved with the use of a body force at the inlet of amplitude $F = 10^{-2}$ and frequency $\omega = 2\pi/T$ and $T = 1000$ resulting in a pressure gradient with amplitude $A = F/L$. All measurements are done after $10T$ iterations in order for the scheme to converge. The agreement between measured velocity profiles and the theoretical expression given by equation (3.63) is shown on figure 3.4 (left). The residual density gradients for $W = 0.0$ and $W_{\max} = 0.17$ are shown on figure 3.4 (right). The density variation along the channel for the conventional model, i.e. $W = 0$, is around $\approx 0.1\%$ while for $W_{\max}$ we improve the variation down to 0.02% namely a factor of 5.

To further analyse the impact of the scheme on the flow, we look at the relative global error L_2 of the flow

$$\parallel \delta \boldsymbol{u} \parallel^2 = \frac{\sum_i \parallel \boldsymbol{u}(\boldsymbol{r}_i, t) - \boldsymbol{u}_0(\boldsymbol{r}_i, t) \parallel^2}{\sum_i \parallel \boldsymbol{u}_0(\boldsymbol{r}_i, t) \parallel^2} \tag{3.65}$$

where $\boldsymbol{u}_0(\boldsymbol{r}, t)$ is the analytical solution given by equation (3.63). The global error is shown figure 3.5 (left) as a function of the frequency of the driving pressure gradient for $W = 0.0$ and $W_{\max} = 0.17$. Although as good as [17], the absolute value of the error is largely due to the values at the inlet which are caused by

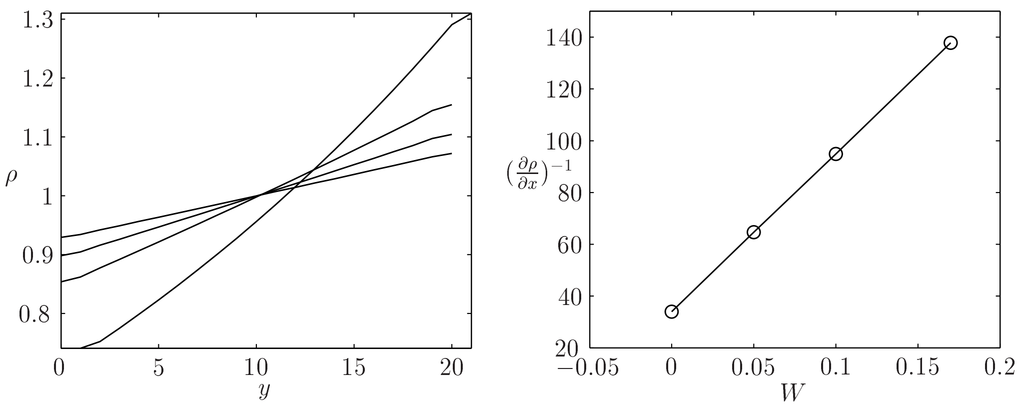

Figure 3.6: Fluid at rest with gravity field.(left) Density profiles for various W. (right) Inverse of the density gradient. The plot behaves as $\approx W^{-1}$ as expected from equation (3.59).

the method we choose to impose a pressure in the channel. In order, to suppress the effect of this boundary condition and weigh the real impact of the repulsive contribution to the flow, we look at the ratio of the errors $\delta u_{W=0}/\delta u_W$ between the curves. This is shown on figure 3.5 (right). We see that for low frequencies, the global error has reduced down to 25% of its original value while at higher frequencies the reduction stabilizes around 30%. Note that, the limit on the higher frequencies where the analytical solution of the Womersley flow is valid is given when the time variation of the pressure field is negligible. This condition holds when $L/c_sT \ll 1$. In our numerical setup, with $c_s^2 = 1/3$ and $L = 30$, this limit is around $T = 500$. Our scheme therefore clearly improves the global error of a factor between 3 and 4.

3.5.3 Barometric fluid

We have just shown applications of our scheme to a steady and unsteady flow. We would here like to apply our ideas to the case of a fluid with external force. In order to show that our idea applies to general situations, it is indeed interesting to see whether our scheme still applies to a case where, although the incompressible conditions exposed in section 3.2.3 are valid, the fluid is in a compressible situation. The distinction between incompressible and compressible situation is best understood by considering the difference between air and water. The pressure in oceans does increase with the height of the water column but the density doesn't change while the density and the pressure do change in the case of air in the atmosphere. In this section, we show that our scheme can produce a pressure gradient in a fluid without a producing a density gradient. This result is generally obtained with the lattice Boltzmann model by the use of a constant external force. Although numerically achieving the correct behavior, the use of such a force is not physical since the real gravity force does depend on the density of the fluid. It is in that respect that our model is physically more satisfying.

We consider a fluid at rest with a gravity force $\boldsymbol{G} = (0, G_y)$.

$$\boldsymbol{F} = \rho \boldsymbol{G} \tag{3.66}$$

A bounce-back scheme is applied at the borders. In the stationary regime, the velocity field can be considered at rest $\boldsymbol{u} = 0$ and the symmetry of the problem imposes that $\rho = \rho(y)$. The Navier-Stokes equation with the expression (3.58) for pressure therefore reduces to

$$\partial_y (cs^2 \rho + \frac{1}{2} W \Delta_t C_2' \rho^2) \;\; = \;\; \rho G_y \tag{3.67}$$

Considering the boundary conditions $\int_0^L \rho(y) dy = L\rho_0$, the solution of this equation in the limit $W \to 0$ is

$$p(y) = c_s^2 \rho(y) = \rho_0 L G_y \frac{\exp[-\frac{G_y}{c_s^2}(L-y)]}{1 - \exp[-\frac{G_y}{c_s^2} L]} \tag{3.68}$$

whereas in the limit $W \to \infty$, we can neglect the term in c_s^2 and the solution for density simply is

$$\rho(y) = \rho_0 + \frac{G_y}{W C_2'}(y - \frac{L}{2}) \tag{3.69}$$

Therefore, by neglecting terms in $O(W^{-1})$, we obtain the following expression for the pressure

$$p(y) = \frac{1}{2} W C_2' \rho^2(y) = \rho_0 G_y (y - \frac{L}{2}) + \frac{1}{2} W C_2' \rho_0^2 \tag{3.70}$$

Finally, with a sufficiently large W, we are thus able to produce a linear pressure gradient while still imposing a gravity proportional to the local density. Again, it is common to obtain a linear pressure gradient by the use of a constant gravity force. This numerical technique, however, has no physical basis and however leaves the density gradient problem unsolved.

Figure 3.6 shows the improvement in the density profile for various values of W (left) and the mean density gradient as a function of W (right) whose behavior in $\nabla \rho \approx W^{-1}$ is in agreement with equation (3.58). In our simulation, the density gradient is thus further reduced down to 25% of its original value. Figure 3.7 shows the pressure (left) and the pressure gradient (right) in the fluid for $W = 0.0$ and $W_{\max} = 0.17$. From these plots, we observe that indeed the pressure gradient converges to a linear expression and the same pressure drop results in a density gradient 4 times smaller.

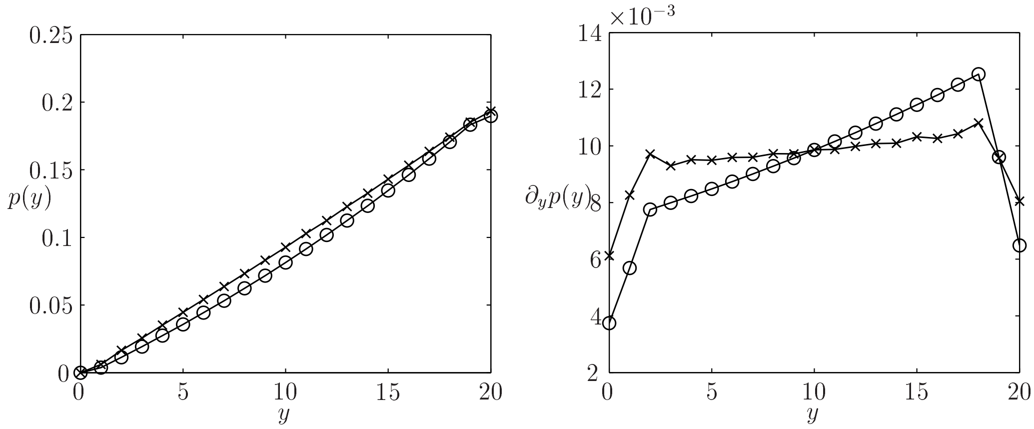

Figure 3.7: (left) Pressure p(y) in the fluid for $W = 0.0$ (circles) and $W_{\max} = 0.17$ (crosses). We see that the pressure tends to be almost linear only for the value $W_{\max}$ which is confirmed by the plot of the pressure gradient(right).

3.6 Conclusion

In order to diminish the numerical compressibility of the traditional lattice Boltzmann model, we introduce a repulsive force between sites of the fluid. The motivation for this additional force is the fact that the incompressibility of real fluids is due to the repulsive part of the Van der Waals potential. The simplicity with which this additional force is added clearly illustrates how the microscopic approach of the Boltzmann scheme allows for an intuitive understanding of the numerical scheme. We validate our approach by looking a two flows whose analytical solution are known and show that the scheme obtains good results: correct velocities and reduced density gradients. We further apply the model to a fluid at rest under gravity field and show that a nearly constant density fluid with linear pressure gradient is achieved. The only observed limit have been numerical instabilities on which linear analysis has not been able to yield any understanding on how and why they appear. To check whether these are caused by numerical precision, we have also looked at how the instability threshold scales with the grid size. The result is that no significant scaling is present or in other words the instability threshold value is constant. This indicates that the instability may in fact be of physical origin. This issues thus remains open.

The motivation behind this work is to reduce the compressibility of lattice Boltzmann fluid while keeping the standard interpretation of the fundamental quantities such as the density and the velocity field. Indeed, we believe that to develop complex applications such as surface waves due to a gravity field requires a model with as much physical meaning as possible. The lattice Boltzmann model is a perfect paradigm as the ideas presented in this chapter have demonstrated.

Chapter 4

Solid-Fluid interface

4.1 Introduction

The subject of this chapter is a particular approach to simulation of fluid systems which are in contact with solid objects. These objects may either be free inside the fluid or serve as boundaries to the physical domain of the fluid. In fact, any physical experiment involving fluids will have also to deal with the contact of a solid which are always present through the border conditions. In the case of static and rigid objects, the lattice Boltzmann modelling of a fluid generally makes use of boundary rules on fixed computation domain. The boundary rule must be a physically sound modification of the numerical scheme used for the bulk of the fluid. Examples of such rules are the bounce-back rule, Inamuro's rule [25] or the mass conserving rule [28]. In this chapter, however, the intention is to deal with dynamic and possibly deformable objects. Therefore, the boundary rule will really be an interaction rule with the solid itself subject to its own dynamics. To fulfill this objective, we propose to model both the fluid and the solid with lattice Boltzmann models. By keeping the same level of description, we believe a better intuitive modelling is possible. The lattice Boltzmann model for the solid which we will use, see chapter 2, does have limitations such as a degenerate elasticity. Nevertheless, the potential ability of the lattice Boltzmann paradigm to model complicated system in a intuitive and computationally very effective way is a strong motivation to push the limits as far as possible. Indeed, any future developments of either the fluid and solid model need incentive leads and hopefully the numerical simulations of this chapter constitute such contributions.

The solid-fluid interface problem can be found for many physical applications such as the transport and deformation of suspensions in a fluid present in many industrial processes. The modification of the behavior of the fluid due to the presence of solid objects also falls within the solid-fluid interface problem and constitutes the modelling of viscoelastic fluids and it is the subject of this chapter. Also of interest are the effects of dynamic boundaries on the flow of a fluid such as the flow of blood in arteries or aeroelasticity problems such as the deformation of buildings under wind pressure.

There are two parts to the modelling the solid-fluid interface. The first part is to incorporate the fluid-solid interaction in the numerical scheme. Fortunately, it is fairly easy to do so within the Boltzmann paradigm since it easily allows the addition of sensible microscopical physics. In particular, the solid model of chapter 2 has shown how contact conditions can be modeled. This step then only requires a numerical validation through a benchmark problem. The second part consists of the permeability problem. Once a fluid-solid interaction is introduced, this does not usually prevent the fluid and the solid from occupying the same physical location. The effect of permeability is generally a posteriori justified as being either negligible or trivial. This problem, however, is clearly of interest in itself as recent papers indicate [29].

The chapter is organized as follow. The first section is a brief review of existing models which deal with the fluid-solid interface where the fluid is modeled with the Boltzmann method. The second section describes our interaction model where both the fluid and the solid are modeled with a Boltzmann model. The third section presents the numerical validation of our model through a drag experiment and Poiseuille flow. In the same section, we make a qualitative attempt at modelling the flow of a fluid contained in a deformable membrane. Finally, we conclude on the perspective of our model.

4.2 Summary of the lattice Boltzmann modelling of a Solid

We briefly summarize here the essential notions of the lattice Boltzmann model for a solid, the full details of which can be found in chapter 2. For a short review of the lattice Boltzmann of fluid dynamics, we refer the reader to chapter 3.

The lattice Boltzmann model of a solid makes use of the BGK formulation

$$f_i(\boldsymbol{r} + \Delta_t \boldsymbol{v}_i, t + \Delta_t) - f_i(\boldsymbol{r}, t) = \frac{1}{\tau}\left(f_i^{(0)} - f_i(\boldsymbol{r}, t)\right) \tag{4.1}$$

where the collision term of the transport equation is expressed as a relaxation to a local equilibrium function $f_i^{(0)}$ which hence contains the appropriate physics. The equilibrium function $f_i^{(0)}$ describing the wave propagation of longitudinal displacements in an elastic solid with the lattice Boltzmann formalism is

$$f_i^{(0)} = \frac{1}{C_2 M}\psi + \frac{1}{C_2}\boldsymbol{v}_i \cdot \boldsymbol{J} \tag{4.2}$$

$$m_0 f_0^{(0)} = \frac{m_0}{C_2 M}\psi \tag{4.3}$$

where

$$\psi = \sum_i m_i f_i \tag{4.4}$$

is the momentum of a particle making up the solid and

$$\boldsymbol{J} = \sum_i m_i f_i \boldsymbol{v}_i \tag{4.5}$$

is the flux of momentum. These quantities are the collision invariants. The quantity $M = (C_0 + m_0^2)/2$ is the mass of the particle. The constant C_0, C_2 are defined as

$$C_0 = \sum_{i>0} m_i \tag{4.6}$$

$$C_2 v^2 \delta_{\alpha\beta} = \sum_{i>0} m_i v_{i\alpha} v_{i\beta} \tag{4.7}$$

and are lattice dependent. In our model, the lattice in use is a D2Q5 lattice and thus the above constants take the values $C_0 = 4$ and $C_2 = 2$ in the bulk. From the definition of mass, however, we see that th model is able to take into account a varying number of neighbors C_0 which on the borders is lower than in the bulk.

The Chapman-Enskog procedure on the above local equilibrium with the special value $\tau = 1/2$ leads to a wave equation for ψ

$$\partial_t^2 \psi - c_s^2 \nabla^2 \psi = 0 \tag{4.8}$$

which shows that transport of momentum in the solid travels at speed $c_s^2 = 1/M$. In fluid dynamics, the value $\tau = 1/2$ is a numerically unstable limit. However, our local equilibrium being linear, ensures that a quadratic form

$$E = \sum_i f_i^2 \tag{4.9}$$

is also conserved and is identified with the total energy at a lattice site. This property therefore numerically bounds the values of the f fields since $|f_i^2|$ cannot diverge. The value $\tau = 1/2$ also ensures the time reversal invariance as can be check in equation (4.2) with $\boldsymbol{J} \to -\boldsymbol{J}$ and $\psi \to \psi$.

The displacements in the solid are then calculated with the following rule

$$\boldsymbol{q}(\boldsymbol{r}, t+\tau) = \boldsymbol{q}(\boldsymbol{r}, t) + \frac{\boldsymbol{\psi}(\boldsymbol{r}, t)}{M} + \frac{\boldsymbol{F}(\boldsymbol{r}, t)}{2M} \tag{4.10}$$

where $\boldsymbol{\psi}$ is formed with two independent wave $\boldsymbol{\psi} = (\psi_x, \psi_y)$ and $\boldsymbol{F} = (F_x, F_y)$ is an external force. The connection between momentum and position and the fact that momentum is conserved by the dynamics yields and extra conserved quantity

$$\boldsymbol{q}(\boldsymbol{r}+\boldsymbol{v}_i,t)-\boldsymbol{q}(\boldsymbol{r},t)+\boldsymbol{f}_i(\boldsymbol{r}+\boldsymbol{v}_i,t)-\boldsymbol{f}_{i+2}(\boldsymbol{r},t)=\Delta_i^0(\boldsymbol{r}) \tag{4.11}$$

where $\Delta_i^0(\boldsymbol{r})$ is the equilibrium separation between two adjacent particles. This is in fact the equivalent of Hooke's law $F = k\Delta x$ with a elastic constant $k = 1$ as long as the solid is modeled alone. Indeed, any re-normalization of $\Delta_i^0(\boldsymbol{r})$ is possible and corresponds to an arbitrary scale. On the other hand, when modelling the interaction with another body such as a fluid, the choice of the scale of $\Delta_i^0(\boldsymbol{r})$ gives rise to the possibility of adjusting the elastic constant with regards to the spatial scale. Therefore by incorporating an extra scale parameter α to equation (4.10) such that $\boldsymbol{q}(t+\tau) = \boldsymbol{q}(t) + \alpha\,(\boldsymbol{\psi}(t)/M + \boldsymbol{F}(t)/2M)$, the effect on equation (4.11) is to produce an elastic constant $k = \frac{1}{\alpha}$.

Finally, it can be shown that the following relation

$$E(t+1) = E(t) + (\boldsymbol{q}(\boldsymbol{r},t+\tau)-\boldsymbol{q}(\boldsymbol{r},t))\cdot\boldsymbol{F}(t) \tag{4.12}$$

holds true when an external force $\boldsymbol{F}$ is exerted on a particle. Therefore, the work done by the force can satisfyingly be put in direct relation with the increase in energy of a particle.

4.3 Example of lattice Boltzmann models

4.3.1 Ladd's model

The model proposed by Ladd [30] deals with a rigid body free to move in a lattice Boltzmann fluid using the BGK scheme. Classical Newtonian mechanics is applied to the body which has a pre-assigned mass and moment of inertia. The interface of the solid and fluid defines a set of fluid nodes, termed particles, where the update rule of the fluid models an exchange of momentum such as to enforce an non-slip condition. The local velocity $\boldsymbol{u}_b$ of particle at position $\boldsymbol{r}_b$ of the solid is computed from the velocity $\boldsymbol{U}$ of the solid's center of mass, its angular momentum Ω and center of mass $\boldsymbol{R}$

$$\boldsymbol{u}_b = \boldsymbol{U} + \Omega\times(\boldsymbol{r}_b-\boldsymbol{R}) \tag{4.13}$$

The momentum exchange causes a local force $\boldsymbol{f}(\boldsymbol{r}_b)$ to be exerted on the particle and the total force $\boldsymbol{F} = \sum_{\boldsymbol{r}_b}\boldsymbol{f}(\boldsymbol{r}_b)$ and torque $\boldsymbol{M} = \sum_{\boldsymbol{r}_b}(\boldsymbol{r}_b-\boldsymbol{R})\times\boldsymbol{f}(\boldsymbol{r}_b)$ on the solid body is obtained by summation over all particles.

The exchange of momentum on the fluid consists in a generalization of the simple bounce-back rule whereby the incoming fields in direction $\boldsymbol{c}_i$ are redirected in the opposite direction $\boldsymbol{c}_{-i}$. The generalization for a moving boundary consist in correcting the bounce-back to take into account the flow which is possible because of the motion of the boundary. The authors achieves this with the following correction

$$f_i(\boldsymbol{r}_b + \boldsymbol{c}_i, t+1) = f_{-i}(\boldsymbol{r}_b, t) + \frac{2}{C_2 v^2}\rho \boldsymbol{u}_b \cdot \boldsymbol{c}_i \tag{4.14}$$

$$f_{-i}(\boldsymbol{r}_b - \boldsymbol{c}_i, t+1) = f_i(\boldsymbol{r}_b, t) - \frac{2}{C_2 v^2}\rho \boldsymbol{u}_b \cdot \boldsymbol{c}_i \tag{4.15}$$

Thus if the particle is fixed $\boldsymbol{u}_b = 0$, the above rule is equivalent to the bounce-back rule. As for the permeability problem, even though the solid is only modelled by its boundary, the fluid inside the solid only contributes to an additional mass and moment of inertia [30]. This method and other variations [30][31] have be shown to be satisfying in order to model the transport of particle suspensions in a fluid. The solid body however is not deformable.

4.3.2 Aidun's deformable membrane

The model proposed by Aidun [32] is a construction based on Ladd's model in order to model a deformable membrane. This purpose of this problem is to better understand the transport and the deformation of polymer-fluid systems such as belts, tapes and films. The objects in the the fluid, i.e. the polymers, being one dimensional, the question of permeability does not arise. On the other hand, the interest of this model is that the objects are now deformable and the deformation w propagates along the membrane according to a wave equation

$$m\partial_t^2 w - T\partial_x^2 w = F(x,t) \tag{4.16}$$

where $F(x,t)$ is the force acting on the membrane due to the fluid and T is the tension in the membrane.

The fluid is a classical lattice Boltzmann model and the interaction of the fluid with the membrane is identical to the model proposed by Ladd [30]. The dynamics of the membrane is obtained, after discretization, with a classical molecular dynamics technique namely the leap-frog scheme

$$\boldsymbol{v}(t + \frac{1}{2}\Delta t) = \boldsymbol{v}(t - \frac{1}{2}\Delta t) + \boldsymbol{a}(t)\Delta t \tag{4.17}$$

$$\boldsymbol{r}(t + \Delta t) = \boldsymbol{r}(t) + \boldsymbol{v}(t + \frac{1}{2}\Delta t)\Delta t \tag{4.18}$$

where the acceleration $\boldsymbol{a}(t)$ at each time step is calculated from the hydrodynamic forces acting on the membrane and the tensions inside the membrane. The algorithm to compute the tension in each segment of the membrane takes into account the angular orientation of each segment, the details of which, more or less intricate, are accountable in the original paper [32]. The model is then used to study the fluttering properties of membranes in a flow and show that the properties of the simulations are in agreement with tunnel experiments.

4.4 The solid-fluid lattice Boltzmann interface

We propose to model the solid-fluid interface using lattice Boltzmann models both for the fluid and the solid. We believe that by using the same level of description for both phases, a better intuitive understanding is possible. The object of the modelling simply resides in defining the interaction between the two models. The simplest mechanism is to implemented an exchange of momentum between the solid and the fluid as would be expected at a microscopic level. This exchange of momentum is such that a non-slip condition is obtained at the interface. In contrast to what was developed in chapter 2, this microscopic collision is non-elastic. The non-slip condition, however, is what is physically expected in fluid and simply means that the fluid and the solid have the same velocity at the interface.

The fluid particles live on a regular lattice while the solid particles are typically off lattice. Therefore, in the present model, we choose that each solid particle exchange its momentum with the fluid element located on the nearest lattice site. The fact that theoretically several solid particles may happen to be interacting with the same fluid site and should hence require a special treatment in order to impose the same velocity to all particles is not taken into account. Each particle interacts independently with the fluid whose momentum is actualised after each interaction. The conservation of momentum, therefore, is naturally guaranteed. We consider that such cases are negligible for well-initialized simulations.

With these consideration in mind, the interaction simply consists of an additional term in the collision stage of the dynamics. Let $\Delta\boldsymbol{P}$ represent the amount of momentum exchanged between a pair of solid-fluid particles. This quantity, computed with the pre-collision fields, can be introduced in the dynamical equation (4.1) in the following way

$$f_i(\boldsymbol{r} + \Delta_t \boldsymbol{v}_i, t + \Delta_t) - f_i(\boldsymbol{r}, t) = \frac{1}{\tau}\left(f_i^{(0)} - f_i(\boldsymbol{r}, t)\right) + \frac{1}{C_2}\boldsymbol{v}_i \cdot \Delta\boldsymbol{P} \tag{4.19}$$

for the fluid and

$$g_k(\boldsymbol{r} + \Delta_t \boldsymbol{v}_k, t + \Delta_t) - g_k(\boldsymbol{r}, t) = \frac{1}{\tau}\left(g_k^{(0)} - g_k(\boldsymbol{r}, t)\right) - \frac{1}{4}\Delta\boldsymbol{P} \tag{4.20}$$

for the solid where we have renamed the fields and the indices so as not to create any confusion. This additional term is justified by looking at the increase of

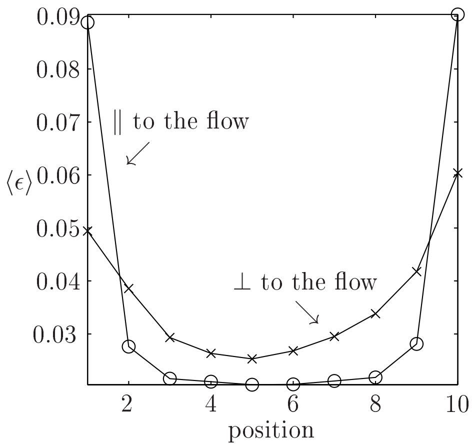

Figure 4.1: The speed of fluid inside a solid. For a 10x10 square solid under traction in the x direction, we measure the normalized difference $\epsilon_{x,y} = |\frac{u_s - u_f}{u_s}|_{x,y}$ of velocity between a solid and a fluid site. The plot is that of the mean difference $<\epsilon>$ in both directions. We observe that apart for a thin layer on the boundaries facing the flow,the fluid inside a moving solid has the same velocity.

momentum after collision. Indeed, it is easy to check that with these relations, the fluid momentum $\rho\boldsymbol{u} = \sum_i m_i \boldsymbol{v}_i f_i$ increases by an amount $\Delta\boldsymbol{P}$ while the solid momentum $\boldsymbol{\psi} = \sum_k g_k$ decreases by the same quantity. The value of $\Delta\boldsymbol{P}$ which satisfies the non-slip condition is

$$\Delta\boldsymbol{P} = Z(\boldsymbol{u}_s - \boldsymbol{u}_f) \tag{4.21}$$

where

$$\frac{1}{Z} = (\frac{1}{\beta\rho} + \frac{1}{M}) \tag{4.22}$$

and $\boldsymbol{u}_s$ and $\boldsymbol{u}_f$ are respectively the speeds of the solid and fluid particles before interaction. Since for the fluid only the density ρ is modeled, the β parameter allows for a scaling of mass between the solid and the fluid. The justification of equation (4.21) can be checked as follows: the fluid momentum after interaction is $\beta\rho\boldsymbol{u}_f + Z(\boldsymbol{u}_s - \boldsymbol{u}_f)$ and, thus its velocity is

$$\boldsymbol{u}'_f = \boldsymbol{u}_f + \frac{M}{M+\beta\rho}(\boldsymbol{u}_s - \boldsymbol{u}_f) \tag{4.23}$$

Similarly, the momentum of the corresponding solid particle is, after interaction, $M\boldsymbol{u}_s - Z(\boldsymbol{u}_s - \boldsymbol{u}_f)$. Therefore, its speed is

$$\boldsymbol{u}'_s = \boldsymbol{u}_s - \frac{\beta\rho}{M+\beta\rho}(\boldsymbol{u}_s - \boldsymbol{u}_f) \tag{4.24}$$

and thus $\boldsymbol{u}'_s - \boldsymbol{u}'_f = 0$.

As for other models, the solid of our model is permeable. As a preliminary test to weigh the consequences of this permeability, we have checked that the velocity of the fluid trapped inside a square solid moving in the solid is identical to that of the solid. This is illustrated on figure 4.1 for a solid with a elasticity constant $k = 1$ which means that the deformations in the solid are small with respect to the spacing of the fluid lattice. We measure the fluid velocity field inside a square object relatively to the velocity of the solid. The result is that the velocity of the fluid is less than 10% different from that of the solid and decreases sharply after the interface. We therefore consider that the permeability question will appear at the interface itself. However, we will see that the size of this boundary layer will also highly depend on the relative elasticity of the solid.

4.5 Numerical Simulations

In this section, we first validate the interaction we have introduced in order to couple the fluid and the solid by looking at a drag experiment of a cylinder moving in a channel. Then, we perform a Poiseuille flow experiment by using the solid as the boundary of a channel. Finally, by allowing the solid to deform at a scale comparable to the flow in a channel, we look at the qualitative behavior of such a system having in mind the possible modelling of the flow of blood in arteries. In the following simulation, we model the fluid with a D2Q7 lattice and the solid with a D2Q4 lattice.

4.5.1 Drag experiment

Consider a two dimensional cylinder of diameter D in a channel of length L. The solid particles forming the cylinder are subject to a constant external force $\boldsymbol{F}$ and their elasticity coefficient is $k = 1$ which corresponds to a quasi-rigid body with regards to the scale of the fluid. The force applied on the body force accelerates the object in the channel filled with a lattice Boltzmann fluid whose viscosity is $\nu = C_4/C_2(\tau - 1/2)$. As the solid moves in the channel, each of its particles exchanges momentum with the surrounding fluid according to the rule explained in the previous section. The mass scaling parameter of the fluid is $\beta = 1$. The channel is periodic along the horizontal direction and has a no-slip boundary conditions at the upper and lower walls obtained with a bounce-back scheme.

In a drag experiment, it is common to consider the so-called drag coefficient [33] [34]

$$C_d = \frac{F}{\rho u_\infty^2 D} \tag{4.25}$$

where u_∞ is the cylinder's velocity in the stationary regime. It is well known

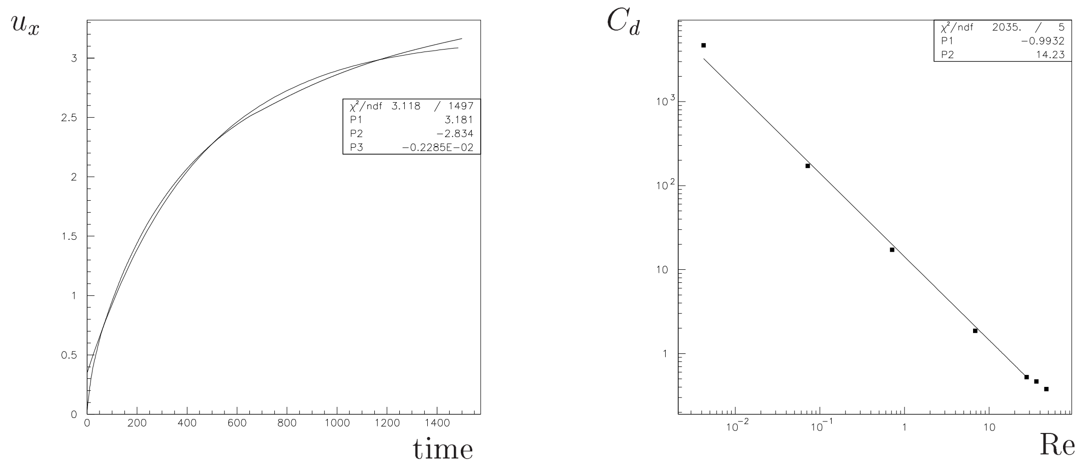

Figure 4.2: (left) the evolution of the velocity of the cylinder follows $u(t) = \frac{F}{a}(1 - e^{-at})$. (right) Stokes law for a cylinder; as expected we have $Cd \propto Re^{-1}$ up to Reynolds number of a 100.

from Stokes law [33] [34] if the Reynolds number is lower than a 100, then the drag force for a cylinder is proportional to the velocity of the cylinder and

$$C_d \propto \frac{1}{\mathrm{Re}} \tag{4.26}$$

is a good approximation where $\mathrm{Re} = u_\infty L/\nu$. In our simulations, we compute the cylinder's velocity u_∞ by considering that at small velocities the velocity of the cylinder obeys

$$\dot{u}(t) = -au(t) + F \tag{4.27}$$

in agreement with (4.26) and whose solution is

$$u(t) = \frac{F}{a}(1 - e^{-at}) \tag{4.28}$$

Figure 4.2 (left) illustrates such a fit for the velocity of the cylinder. It is important to note that since we are really dragging the cylinder inside the channel, the problem due to the border conditions are irrelevant. Indeed, the measurements shown on figure 4.2 (left) are taken while the fluid is at rest and therefore still unperturbed by the motion of the cylinder. The drag force F is the only parameter we use to adjust the value of our Reynolds number. Figure 4.2 (right) shows the results of our drag experiments. The correct relation between the drag coefficient and the Reynolds number as expected by Stokes law is observed and corresponds to experimental results reported in textbook [33]. In addition, as the Reynolds number approaches the value of 10^2 where Stokes law is in fact no longer valid, a small deviation can effectively be seen.

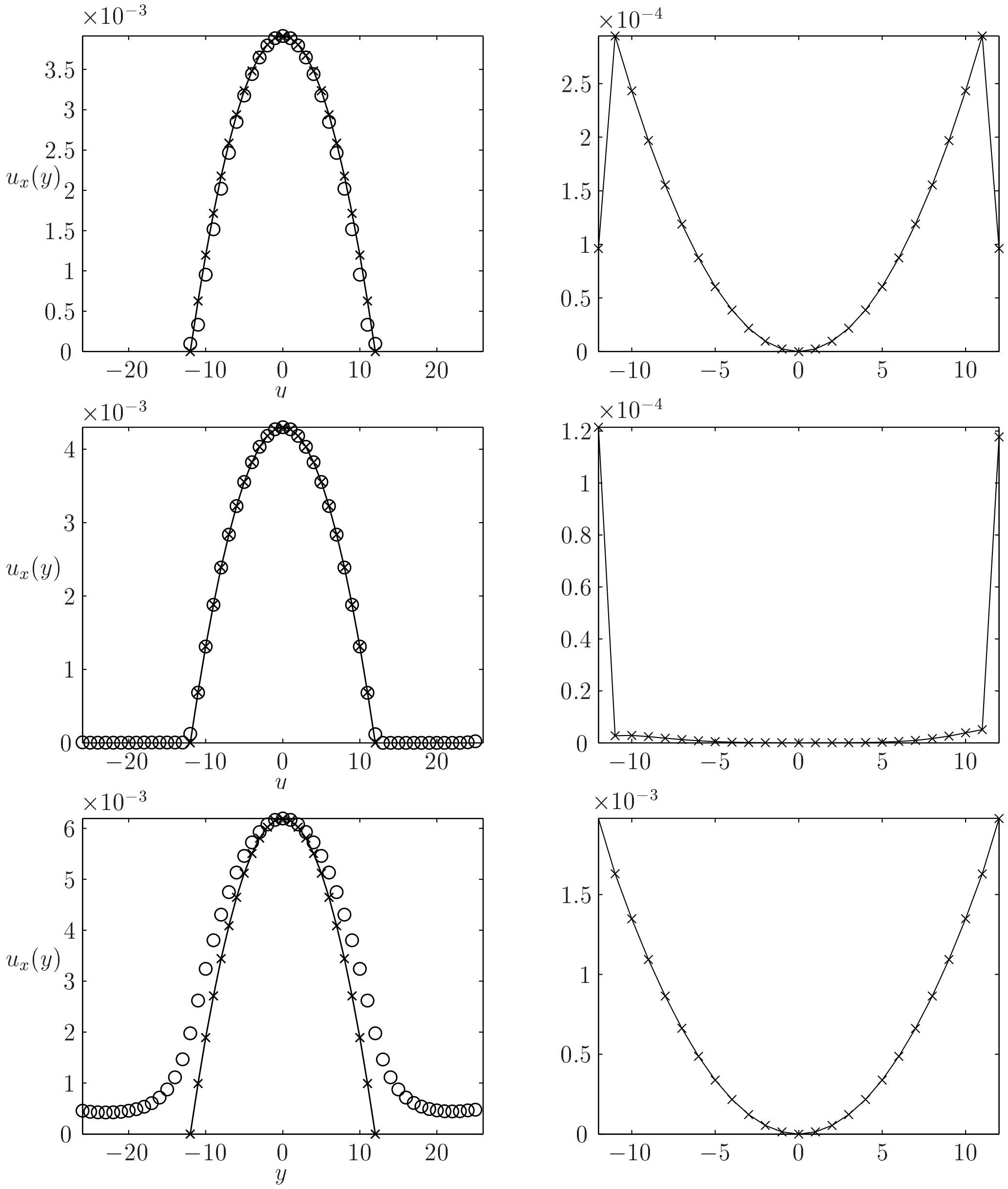

Figure 4.3: The left plots are the velocity profiles of a uniformly accelerated fluid contained within a solid at $t = 2000$ where the circles are the numerical experiments values and the crosses are the theoretical values. The viscosity of the fluid is $\nu = 0.125$. The right-hand plots are the error to the theoretical expression of the velocity. The top plots are a obtained with classical bounce-back scheme on walls and no solid and serve as reference. The middle plots are obtained with a rigid solid body $k = 10$. The bottom plots are with an elastic solid $k = 1/150$ and this causes the fluid contained in the solid to flow inside the solid whose permeability is now clearly observable.

4.5.2 Poiseuille flow

To further validate our model and as a first step towards modelling a deformable membrane in a fluid, we study a Poiseuille flow where the channel of diameter D is contained within a solid. Apart for the interaction between solid and fluid there is therefore no boundary rule for the fluid phase and the fluid is subject to a constant body force. We study two situations and compare them with a classical bounce back rule for the channel. The first is an effectively rigid solid where the elasticity constant of the solid is low $k = 10$ while the second is taken to be very elastic $k = 1/150$. The solid is completely free to move except for two central rows of particles parallel of the flow of the fluid which are considered far from the solid-fluid interface. This prevents the motion of the solid to be periodic in the fluid lattice and serves as the momentum absorbing element in the fluid. Indeed, since the fluid is driving by a constant force, the whole system would accelerate indefinitively. The interaction rule being essentially a velocity condition on both phase, we expect to correctly reproduce the velocity profile of a Poiseuille flow even though the solid is permeable. The flow is obtained after 2000 time steps with a body force of 10^{-5} acting in the channel. The viscosity of the fluid is $\nu = 0.125$ obtained by choosing a value of $\tau = 1.0$. The result are shown on figure 4.3. The left-hand plots show the velocity profiles and the right-hand plots show the error with regards to the theoretical expression for the velocity

$$u_x(y) = 4u_{\max}D^2(\frac{y}{D} - \frac{1}{2})(\frac{1}{2} - \frac{y}{D}) \tag{4.29}$$

The first observation is that the interacting solid-fluid behaves better than the bounce-back scheme. Indeed, the relative global error

$$\parallel \delta \boldsymbol{u} \parallel^2 = \frac{\sum_i \parallel \boldsymbol{u}(\boldsymbol{r}_i, t) - \boldsymbol{u}_0(\boldsymbol{r}_i, t) \parallel^2}{\sum_i \parallel \boldsymbol{u}_0(\boldsymbol{r}_i, t) \parallel^2} \tag{4.30}$$

normalized to the maximum velocity $u_{\max}$ is equal to 0.008 against 0.036 for the bounce-back scheme. Second, when the elasticity of the solid is high, the fluid is able to create an evanescent boundary layer. This clearly illustrates the fact the our solid is permeable and that it may not be acceptable to model a real membrane. The following experiment will show however that qualitatively the correct behavior for the system is achieved with our model.

4.5.3 Flexible membrane

In this experiment we qualitatively look at the behavior of our model when a flow is imposed on the fluid with a pressure gradient. The solid being permeable there is a difficulty at performing quantitative measurements. Indeed these might lead to the necessity of entirely reconsidering the whole interaction rule in order to have a strict impermeable membrane. However, we will now show that the

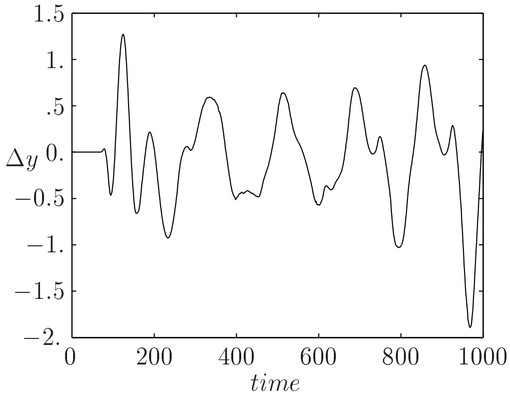

Figure 4.4: The motion of a test particle in solid forming the boundary of a fluid driven by a pressure gradient.

present rule is able to reproduce the behavior we expect from a real system in promising way.

The numerical setup is as follow. A pressure at the inlet of a fluid with $\tau = 1.0$ is used to set a flow and a gradient of pressure. The value of the body force used at the inlet is $1e-3$. The solid body is made to be particularly elastic by a choice of $k = 1/950$. This causes the whole system to oscillates strongly as the vertical displacement of a test particle in the solid clearly illustrates, see figure 4.4. We study the system at two moments in time: $t = 1000$ and $t = 1200$.

First, we look at the shape of the solid and the norm $\| \boldsymbol{u} \| = \sqrt{u_x^2 + u_y^2}$ of the fluid velocity field. These measurements are illustrated on figures 4.5 and 4.6. We clearly see that the solid is highly deformed and that the velocity field strongly follows the shape of the solid while being quasi zero inside the solid. This properties of the velocity field is confirmed by the measurements of the components of velocity (u_x, u_y) as shown on figure 4.7. Indeed, the component u_y normal to the flow is one order of magnitude lower than the component u_x parallel to the flow.

Second, we compare the shape of the solid with the gradient of the pressure in the direction normal to the flow. Figure 4.8 shows the contour-line of the pressure gradient with regards to the shape of the solid. We observe that the gradient of pressure follows the interface of the solid and fluid and that it peaks where the solid is most strained. We therefore qualitatively see that the pressure in the fluid does produce a deformation in the membrane.

From these observations, we conclude that the model behaves in a way which is physically reasonable. We yet have to quantitatively validate this numerical setup with data from experimental examples.

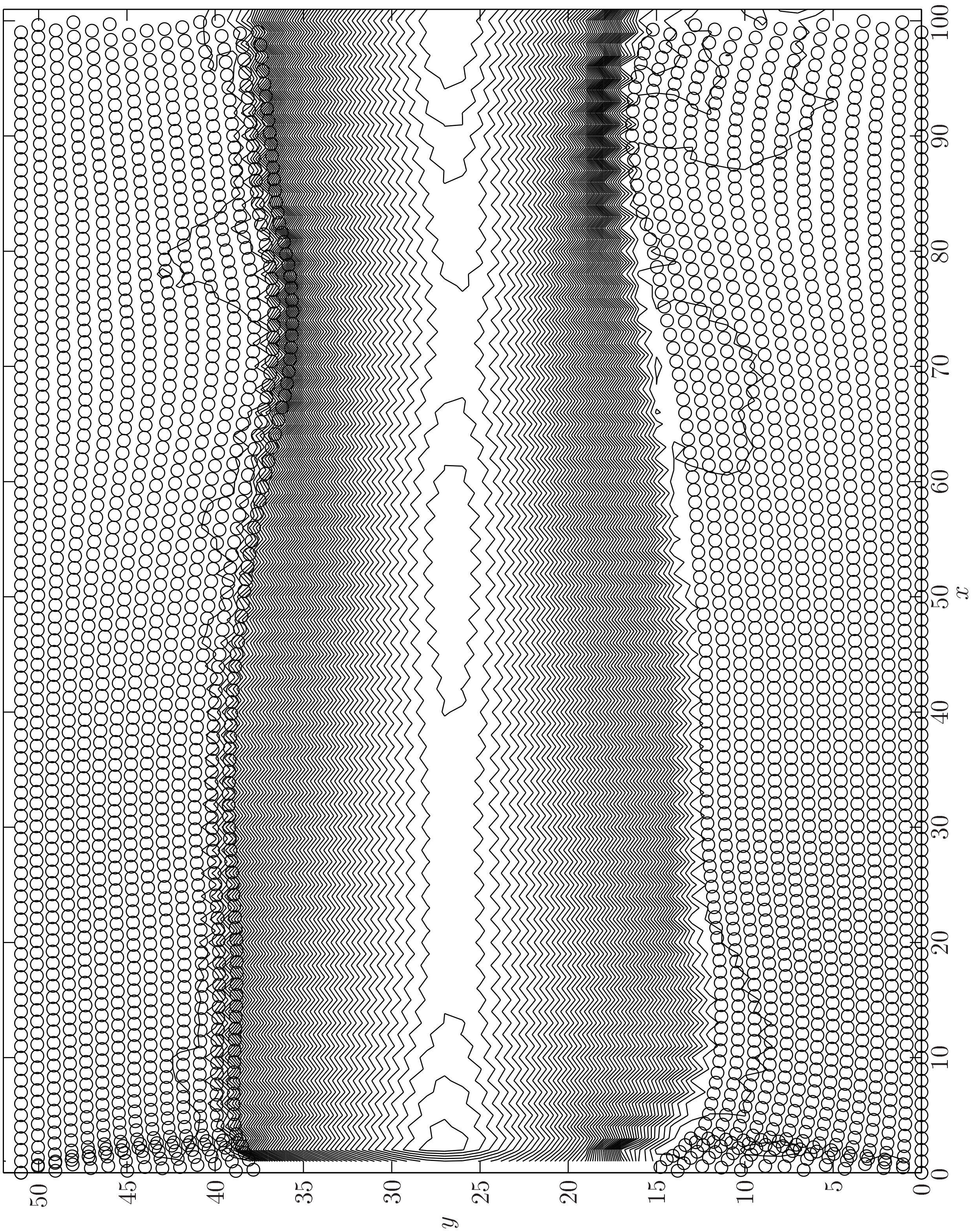

Figure 4.5: Flow of a lattice Boltzmann fluid contained within a lattice Boltzmann solid at $t = 1000$. The solid is represented by circles and the fluids velocity field is represented by the contour lines of the norm of the velocity $\parallel \boldsymbol{u} \parallel = \sqrt{u_x^2 + u_y^2}$.

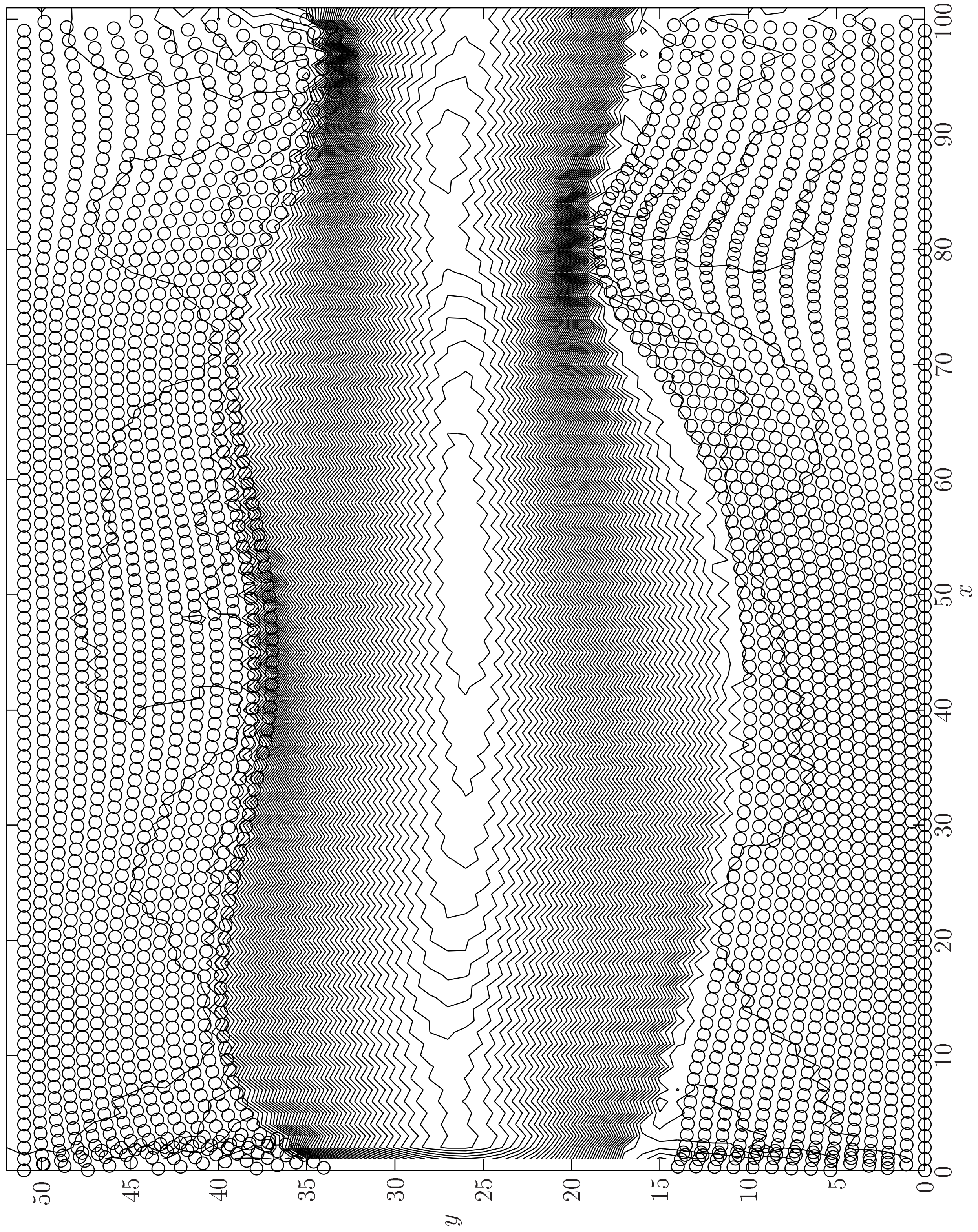

Figure 4.6: Flow of a lattice Boltzmann fluid contained within a lattice Boltzmann solid at $t = 1200$. The solid is represented by circles and the fluids velocity field is represented by the contour lines of the norm of the velocity $\parallel \boldsymbol{u} \parallel = \sqrt{u_x^2 + u_y^2}$.

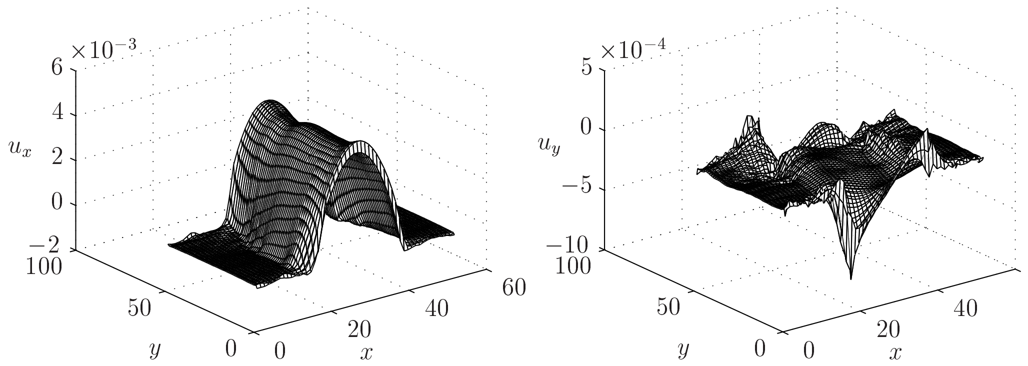

Figure 4.7: The velocities of a lattice Boltzmann flow contained within a lattice Boltzmann solid. We observe that u_x is one order of magnitude larger than u_y demonstrating that although the solid is permeable most of the flow is in the direction parallel to the channel.

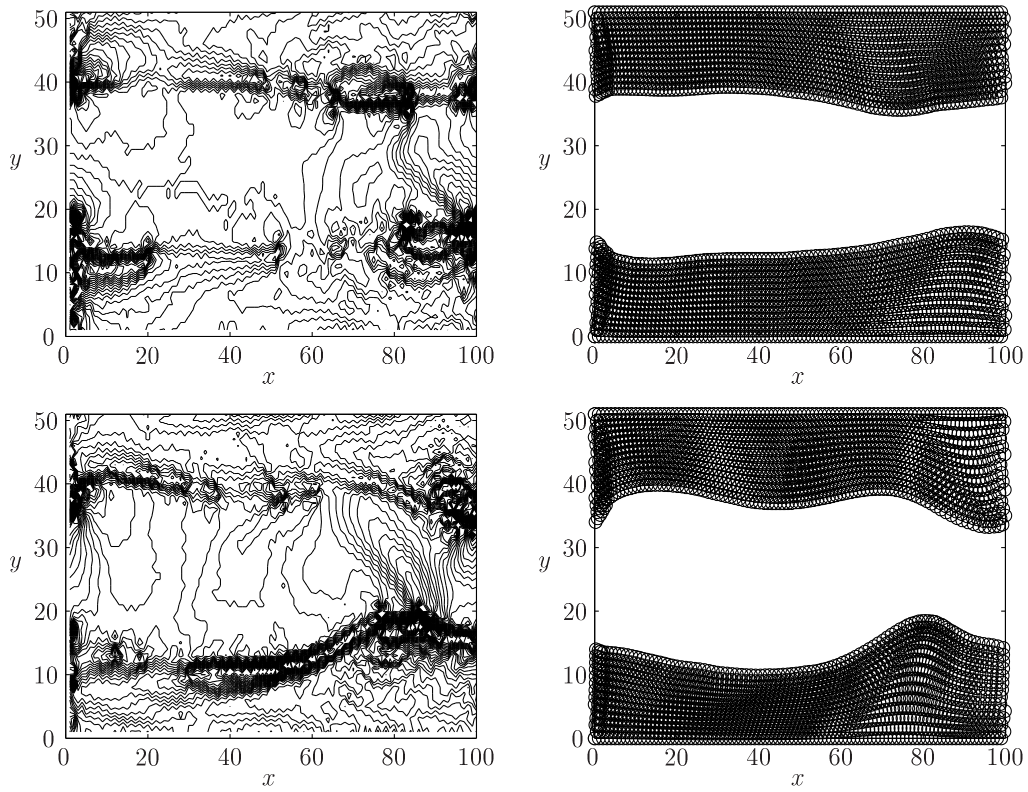

Figure 4.8: (left) The gradient of pressure in the direction normal to flow and (right) the shape of the solid serving as boundary. We see that the gradient peaks where the solid is most strained by the flow.

4.6 Conclusion

This chapter has presented a lattice Boltzmann model for the interface of a fluid and a solid. The novelty with regards to other models is that both the solid and the fluid are modeled with a lattice Boltzmann model. The same level of modelling is therefore kept and it is thus very intuitive. To couple the two lattice Boltzmann models, we simply model an exchange of momentum between the solid and the fluid to obtain a no-slip condition. As for other models, the solid is permeable. This permeability is mostly visible at the interface and this interface is dependent on the elasticity of the solid. For a low elasticity, the permeability can a posteriori be shown to have little effect on the resulting simulations. Although the model for the solid is known to be have an incomplete elasticity, numerical validation of our model through a drag experiment of a cylinder in a channel and Poiseuille flow shows that it behaves remarkably well. The model is further used to study the behavior of a flexible membrane in a flow with a slight pressure gradient. The results shows that qualitatively the model behaves well namely that the velocity field and the pressure field follow the shape of the solid. These results are sufficiently encouraging so as to further improve the solid and interface model. A promising application we have in mind for this model is the simulation of blood flow in arteries [35].

Chapter 5

Viscoelasticity

5.1 Introduction

The study of classical fluid dynamics is mostly concerned with fluids which common people will easily identify either as a liquid or as a gas. These same people will have difficulties, though, saying whether yogurt or honey are solid or liquid. Similarly, science has difficulties finding a formal theory for these substances which are defined as viscoelastic since they may exhibit both the behavior of solids and liquids. A lot of products of everyday life from foods to all kinds of petrol derivatives are in fact viscoelastic. Engineers therefore have developed phenomenological models to describe the behavior of these kinds of fluids. However, it is a fundamental subject of research to understand these systems from a more microscopical point of view since a lot of viscoelastic system are in fact obtained by the mixture of a liquid with microscopic constituents such as particles or polymers. The theoretical framework for such microscopical studies is statistical physics and the favored numerical tool of simulation is molecular dynamics techniques. The computation limits of molecular dynamics are a powerful motivation to attempt the modelling of viscoelasticity through models inspired by statistical physics itself such as the lattice Boltzmann method. Indeed, the computation power involved in molecular dynamics requires expensive supercomputers and the time scale accessible is often quite short. In this chapter, we look at the perspective of simulating a viscoelastic liquid using both the lattice Boltzmann model for a fluid, see chapter 3 and the lattice Boltzmann model for a solid even though the latter is known to be present incomplete elasticity, see chapter 2. Nevertheless, the clear numerical advantages of such models is a strong enough reason to look at the possibilities arising and get a better understanding on the real limits and the necessary improvements.

The chapter is organized as follow. First, we provide a short theoretical summary of what viscoelasticity is. Second, we present two models using the lattice Boltzmann method: the first is a phenomenological variation of the classical

Boltzmann in order to reproduce viscoelastic effects; the second is a combination of the lattice Boltzmann method with molecular dynamics techniques. We then present simulations which we have performed in order to to model viscoelasticity where the fluid and solid models interact with by local exchange of momentum as described in chapter 4. First, we look at the qualitative behavior of a single chain of solid in a fluid. Then we study the behavior of a polymerised fluid. Finally, we conclude on the limits and further developments needed in order to improve the model.

5.2 Theory

Rheology is the science of the flow of matter, be it solid or fluid. In fact, rheology classifies matter in three categories[36]:

1. **elastic materials**: in a purely elastic material all energy added is stored in the material. These materials, commonly named solids, are described by the theory of linear elasticity.

2. **viscous materials**: in a purely viscous material all energy added is dissipated into heat. These materials, named fluids, are described by the theory of hydrodynamics.

3. **viscoelastic materials**: material which exhibits both viscous and elastic behaviour.

A general theory of rheology should therefore be able to describe all of the above categories. In such a theory, all matter would be viscoelastic and the fluid and solid states would correspond to specific limiting behaviors. Often, however, viscoelastic models are obtained by modifying the constitutive equations of either the fluid or solid theories thereby yielding only one of the two limits[1]. This constitutes the phenomenological modelling approach. Another approach consists in deriving the constitutive equations, i.e. the relation between strain and stress, by modelling the microscopical constituents of matter and using the tools of statistical physics. This approach is mostly focused on the modelling of fluids such as polymer solutions or melts.

In order to better understand the viscoelastic state, let us thus first look at the equations which are the foundations of both the fluid and solid theories. The measurable quantities of both systems are respectively the velocity field $\boldsymbol{v}[ms^{-1}] = \boldsymbol{v}(\boldsymbol{r}, t)$ for the fluid and the displacement field $\boldsymbol{u}[m] = \boldsymbol{u}(\boldsymbol{r}, t)$ for the

[1] depending on the case, we therefore speak of a viscoelastic fluid or a viscoelastic solid.

solid. The first principle we expect to be valid is the conservation of mass $\rho[kg]$ given in the form of the continuity equation

$$\frac{\partial \rho}{\partial t} + \nabla \cdot (\rho \boldsymbol{v}) = 0 \tag{5.1}$$

which simply states that the variation of mass in time for any volume is equal to the flow of mass through the surface of the volume. The second principle, Newton's law, is expressed through the balance of momentum for any volume

$$\rho \dot{\boldsymbol{v}} = \rho \boldsymbol{F} + \nabla \cdot \sigma \tag{5.2}$$

where $\boldsymbol{F}$ is an external bulk force and σ is the stress tensor on the surface of the volume.

Now, the first distinction between fluid and solid arises in the fact that fluids flow while solids don't and therefore the mathematical expression of the stress tensor exerted on a volume of matter differs. For solids, it is experimentally observed that small stresses generates deformation $\boldsymbol{u}$ or the related quantity strain ε

$$\varepsilon_{ij} = \frac{1}{2}(\frac{\partial u_i}{\partial x_j} + \frac{\partial u_j}{\partial x_i}) \tag{5.3}$$

without affecting the integrity of the solid. This ability to withhold strain is called elasticity. The linear theory of elasticity thus relates the stress tensor σ_{ij} and the strain tensor ε_{kl} through

$$\sigma_{ij} = C_{ijkl}\varepsilon_{kl} \tag{5.4}$$

where C_{ijkl} is the elasticity tensor. For a homogeneous isotropic solid, this relation reduces to

$$\sigma = \lambda \mathrm{Tr}(\varepsilon) + 2\mu\varepsilon \tag{5.5}$$

where λ and $\mu[km^{-1}s^{-2}]$ are the only two remaining degrees of freedom: the Lamé constants. This expression together with the balance of momentum equation (5.2) and the explicit expression (5.3) for the strain ε in terms of the displacements field $\boldsymbol{u}$ leads to the Navier equation of motion, see chapter 2 and [5].

On the other hand, a fluid does not keep its integrity and any stress exerted on it will result in the flow of the fluid. The stress tensor therefore relates to the strain rate $\dot{\varepsilon}$ instead of the strain. The ability to flow is called viscosity[2]. The classical theory of hydrodynamics assumes a linear relation between the stress σ and strain rate $\dot{\varepsilon}$. These fluids are Newtonian fluids and non-Newtonian fluids are

[2]although the term fluidity would be more appropriate.

Name	constitutive equation	behavior
Solid	$\sigma = C\varepsilon$	linear elasticity
Newtonian	$\sigma = \eta\dot{\varepsilon}$	linear viscosity
Bingham	$\sigma - \sigma_Y = U\dot{\varepsilon}$	yielding effect
Power-law	$\sigma = k\dot{\varepsilon}^n$	shear-thickening or shear-thinning
Herschel-Bulkley	$\sigma - \sigma_Y = k\dot{\varepsilon}^n$	shear-thickening or shear-thinning and yielding
viscoelastic solid	$\sigma = \int_0^t G_E(t-s)d\varepsilon$	solid with memory effect
Maxwell	$\sigma + \lambda\dot{\sigma} = -\eta\dot{\varepsilon}$	
Oldroyd-B	$\sigma + \lambda\frac{D}{Dt}\sigma = -(\eta_s + \eta_p)\left(\dot{\varepsilon} + \frac{\lambda\eta_s}{\eta_s+\eta_p}\dot{\varepsilon}\right)$	

Table 5.1: Rheological models describing various behaviors of matter submitted to a shear stress. The models consists in giving the constitutive equation i.e. relation between the stress σ and the shear strain ε. The quantities $C, \eta, \sigma_Y, U, k, n, \lambda, \eta_P, \eta_s$ are all model constants. The Maxwell and Oldroyd-B models are based on a theoretical approach while all other models are based on observations.

simply fluids for which this relation is not linear. For a homogeneous isotropic Newtonian fluid, the relation is

$$\sigma = \eta\dot{\varepsilon} + (\xi - \frac{2}{3}\eta)\mathrm{Tr}(\dot{\varepsilon}) \tag{5.6}$$

where η and $\xi[km^{-1}s^{-1}]$ are the viscosity coefficients. For a perfect fluid, the stress tensor reduces to a pressure term $\sigma_{ij} = p\delta_{ij}$ and equation (5.2) leads to the usual Euler equation while for an incompressible flow, i.e. $\mathrm{div}\boldsymbol{v} = 0$, the constitutive equation reduces to

$$\sigma = \eta\dot{\varepsilon} \tag{5.7}$$

and the only viscosity constant to contribute is η. This equation together with equation (5.2) lead to the Navier-Stokes equation of motion.

Having explained how a fluid and a solid differ in terms of the balance equations in consideration, we now come to difficulty encountered when trying to model the viscoelastic phase which possesses both solid and fluids properties. Indeed, the question is how do we mathematically combine the models of fluids which flow and solid who do not flow. The problem here is that the frame of reference is changing with time in a fluid and not in the solid. In practice, one constructs a model by extending or combining constitutive equations such as equation (5.5) and equation (5.6). The problem is that the time derivative in equation (5.6) is not valid or permitted in a moving frame of reference. The permissible way of extension is itself subject to discussion [37]. A widely used set of admissibility criteria for constitutive equations was suggested by Oldroyd [38]. It states that a constitutive equation may contain components of stress and strain tensors as well as time integrals and derivatives as long as causality is unaffected. It also must be independent of: the frame of reference, the translational and rotational motion of an element, the strain and stress in neighboring elements. In the examples we will describe below, the Oldroyd criteria essentially corresponds to using the correct expression for time derivatives.

5.2.1 Phenomenological Models

To model matter which does not follow a linear theory, the simplest approach consists in changing the constitutive equation in order to reproduce observed behaviors. Table 5.1 gives a overview of some models, mostly non-Newtonian fluids [36]. Example of rheological behavior are shear-thickening or thinning where a fluid becomes more or less viscous with motion. Another effect is the yielding of matter which will behave as a elastic solid up to a given threshold and then start to flow like a fluid. Viscoelasticity of solids is often best understood in the form a memory effect where the strain on a solid not only depends on the present magnitude of the stress but also on the history of the load process. Most models are essentially based on observations except for the Maxwell and Oldroyd-B fluid which are based on a theoretical modelling and which we will now discuss.

Maxwell model

The Maxwell model (1867) [39] is a useful model to start with since it is about the simplest model exhibiting viscoelastic effect. The basic idea is to couple a spring with a viscous component as shown on figure 5.1. If the spring is deformed on a short time scale, the viscous element does not have the time to react and the whole system acts as an elastic spring. On the other hand, if a force is exerted on a longer time scale, we essentially have the response of the viscous element and the system acts as a fluid. This model better applies to viscoelastic solids than fluids because of its limitations to infinitesimal deformations.

In the serial arrangement of an elastic spring $\sigma = -E\varepsilon$ with elastic modulus E and a viscous component $\sigma = -\eta\dot{\varepsilon}$, the stress in both elements are identical and the strains add to give the total strain ε, we can therefore differentiate the expression of strain for the spring and obtain after summation

$$\frac{\sigma}{\eta} + \frac{\dot{\sigma}}{E} = -\dot{\varepsilon} \tag{5.8}$$

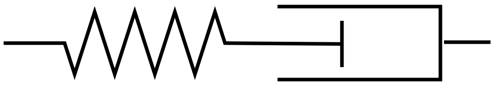

Figure 5.1: The Maxwell model for viscoelastic solid (1867). Viscoelastic behavior is obtained by arranging an elastic spring and a viscous irreversible component in series. In the same spirit, other models are therefore possible such as the Kelvin-Voigt model where the components are mounted in parallel.

which can be rewritten

$$\sigma + \lambda\dot{\sigma} = -\eta\dot{\varepsilon} \tag{5.9}$$

where $\lambda = \eta/E$ is now a relaxation time. The time derivative is a simple partial derivative. This is possible since strain is taken to be infinitesimal and therefore non-linear terms are negligible. The model however does not fulfill Oldroyds criteria since the time derivative does not take into account the fact the reference frame is in motion. The interesting point however is that, by construction, it both recovers the solid ($\lambda \to 0$) and the fluid ($\lambda \to \infty$) limits.

Oldroyd-B model

The admissible form of the Maxwell model with regards to Oldroyd's criteria is obtained by replacing the partial time derivative of the latter into a upper convected derivative [40].

$$\sigma + \lambda\frac{D}{Dt}\sigma = -\eta_p\varepsilon \tag{5.10}$$

where D/Dt allows for terms due to the transport of matter to appear. The use of such an equation for polymers in a solution with a Newtonian solvent of viscosity η_s constitutes Oldroyd's fluid of type B. An equation for the total stress $\sigma = \sigma_{\text{solvent}} + \sigma_{\text{polymer}}$ is derived from equation (5.7) and equation (5.10)

$$\sigma + \lambda\frac{D}{Dt}\sigma = -(\eta_s + \eta_p)\left(\dot{\varepsilon} + \frac{\lambda\eta_s}{\eta_s + \eta_p}\dot{\varepsilon}\right) \tag{5.11}$$

In the limit $\lambda \to 0$ where Newton's law of viscosity is recovered, it is easily shown that the polymer part simply adds a contribution $s = \eta_p/\eta_s$ to the stress tensor. The Oldroyd-B model can also be derived using concepts from statistical mechanics as shall be presented in the following section.

The Deborah number

The relaxation time constant λ which appears in the constitutive equation of the Maxwell model (linear or upper convected form) gives rise to a non-dimensional parameter, the Deborah number[3]

$$\mathrm{De} = \frac{\lambda}{T} \tag{5.12}$$

where T is the characteristic time scale of the flow. The difference between λ and T is that λ can be considered as the microscopic time scale of the constituents of the system while T belong to the macroscopic time scale of the system itself. A similar number, the Weissenberg number $\mathrm{We} = \lambda\dot{\varepsilon}$, relates the relaxation time to the typical shear rate of the flow. Experimentally, either numbers are used; from a theoretical point of view, however, the two definitions are redundant.

5.2.2 Microscopical Models

The microscopical approach to viscoelastic modelling consists in describing the solid microscopical constituents which are present in a fluid solvent and then in calculating the contribution to the stress tensor of the constitutive equation using statistical mechanics. This approach essentially deals with viscoelastic fluids such as polymers melts (high density of polymers in solvent) or solutions (low density of polymers in solvent). The first and obviously the simplest model to describe a polymer consists in using an elastic spring connecting two masses. This method is usually referred to as the dumbbell model. The aim of this section is only to give a brief overview of the microscopical approach. For a complete discussion of the problem, we refer the reader to [41]

The main problem of the microscopical modelling is to compute the contribution arising from the dumbbells to the stress tensor of the macroscopic constitutive equation. This contribution has two origins. Consider an arbitrary plane in the fluid. The first contribution arises from the transport of dumbbells through the plane. It has been shown [42] that this contribution is $\sigma = -nkT\mathbb{1}$ where n is the characteristic density of dumbbells, i.e. the mean number of dumbbells with center of mass in a unit volume around the plane, and kT is the temperature dependence. The second contribution is due to the transmission of stress along the dumbbell. This contribution takes the form $\sigma = n\langle \boldsymbol{RF} \rangle$ where $\boldsymbol{F}$ is the force in the dumbbell and $\boldsymbol{R}$ is the end-to-end vector of a dumbbell

$$\boldsymbol{R} = \boldsymbol{r}_2 - \boldsymbol{r}_1 \tag{5.13}$$

where $\boldsymbol{r}_2$ and $\boldsymbol{r}_1$ are the position of masses m_1 and m_2. The $\langle \boldsymbol{RF} \rangle$ operator gives the statistical average of the quantity $\boldsymbol{RF}$ in the fluid. The total stress tensor

[3]The origin of this name are the words attributed to the old testament prophetess Deborah: *The mountains flowed before the Lord.* Judges 4:4-5

can therefore be written as

$$\sigma = \eta\dot{\varepsilon} - nkT\boldsymbol{I} + n\langle \boldsymbol{R} \cdot \boldsymbol{F} \rangle \tag{5.14}$$

which is called Kramers expression. For a Hookean dumbbell, the force in the spring is linear with the end-to-end vector $\boldsymbol{F} = \alpha\boldsymbol{R}$ and it can be shown [41] that Kramers expression yields the constitutive equation of an Oldroyd-B fluid.

$$\sigma + \lambda \frac{D}{Dt}\sigma = (\eta_p + \eta_s)\left(\dot{\varepsilon} + \frac{\lambda\eta_s}{\eta_s + \eta_p}\frac{D}{Dt}\varepsilon\right) \tag{5.15}$$

The derivation of Oldroyd's equation also leads to a microscopical expression for the relaxation time

$$\lambda = \frac{1}{2\alpha\xi_{12}} \tag{5.16}$$

where $\xi_{12} = 1/\xi_1 + 1/\xi_2$ and ξ_i are the friction coefficients arising from Stokes law. For a spherical mass of radius r, this coefficient is $\xi = 6\pi\eta r$.

A further study of the properties of the Oldroyd-B model shows that it is limited to a type of fluid named Boger fluid submitted to a shear stress. The fundamental reason for the limits is due to the fact that dumbbells have infinite extensibility. In order to suppress the effects due this, models with finite extensibility or FENE (finite extensibility nonlinear elastic) models have been proposed [39] [41].

5.3 Lattice Boltzmann models for viscoelasticity: short review

We briefly present here two approaches making use of the lattice Boltzmann fluid model to produce viscoelastic effects. The first is a phenomenological approach which consists in introducing a stress dependent viscosity in the model. The second is a combination of molecular dynamics for the polymer and lattice Boltzmann model for the fluid.

5.3.1 Viscosity redefinition

The lattice Boltzmann model first proposed by Aharonov [43] and then adapted to the BGK form by Rakotomalala [44] can be considered as the simplest approach to modelling a non-Newtonian fluid since it simply consists in a slight modification of the existing lattice Boltzmann model. Indeed, to obtain a viscoelastic behavior it simply introduces time and spatial dependency on the viscosity which is usually constant in the classical Boltzmann scheme. For instance, in order to model a power-law fluid under shear stress for which the stress-strain rate relation is

$$\sigma = \eta \left(\frac{\partial u_x}{\partial y} \right)^n \tag{5.17}$$

where n is the power-law exponent, we can use the fact that the kinematic viscosity ν can be adjusted with the relaxation time τ to the local equilibrium through[4]

$$\nu = \frac{C_4}{C_2}(\tau - \frac{1}{2}) \tag{5.18}$$

which is a free parameter of the lattice Boltzmann model. Therefore, the apparent viscosity $\eta = \sigma/\dot{\varepsilon}$ we want to impose can be computed at each time step with

$$\eta = \left(\frac{\partial u_x}{\partial y} \right)^{n-1} \tag{5.19}$$

and the relaxation time τ set accordingly with equation (5.18) and remembering that kinematic viscosity is the viscosity divided by the density $\nu = \eta/\rho$. The value of n can then be used to model either a shear-thinning or shear-thickening fluid. In lattice Boltzmann models, the stress-strain relation results from the choice of the local equilibrium. Therefore, a more fundamental approach would consists at re-mastering the equilibrium function in order to obtain sufficient richness to model equation (5.17). This approach can be found in [45].

5.3.2 Lattice Boltzmann and molecular dynamics

This model [46] proposes to couple a lattice Boltzmann model for the fluid with a classical molecular dynamics for a suspension in the fluid. The suspension or chain of monomer is modeled through a bead-spring model which consists of repulsive Lennard-Jones monomers which are connected with non-harmonic springs (the FENE potential [41]). The repulsive potential acts between all monomers. The equations of motion are solved using the Verlet algorithm [47]. Considering that the hydrodynamic evolutions happens on time scales faster than the motion of the monomer chain, the model considers that the chain can be viewed as a point-like particle when interacting with the fluid. In analogy to Stokes formula, the force $\boldsymbol{F}$ acting on the chain is therefore proportional to the difference in velocity between the fluid $\boldsymbol{u}$ and the monomer $\boldsymbol{v}$

$$\boldsymbol{F} = -\xi(\boldsymbol{v} - \boldsymbol{u}(\boldsymbol{r}, t)) + \boldsymbol{f} \tag{5.20}$$

where $\boldsymbol{u}(r, t)$ is the result of an interpolation from the fluids lattice points nearest to the monomers position. The opposite force is then applied to each lattice site

[4] C_2 and C_4 are constants depending on the lattice topology, see chapter 3

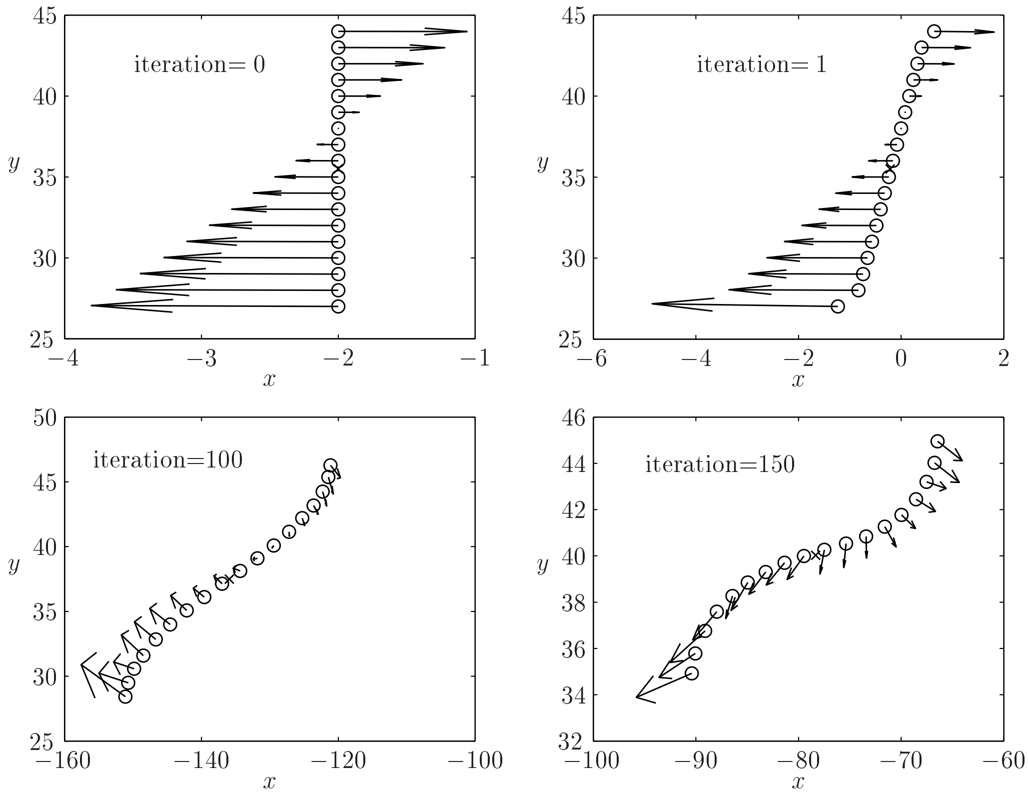

Figure 5.2: The shape of the polymer placed in a shear flow at four different time steps. The polymer is initially orientated in the direction normal to the flow as the velocity (arrows) of the fluid at the particles positions shows. The chain then deforms in the flow while still keeping its integrity. Note however that the extension in the x direction is largely affected as the scale of the x axis shows. This is due to the fact that the polymer is chosen with elastic constant $k = 1/100$ which corresponds to a relatively high elasticity.

in correct proportions with regards to the interpolation. The friction parameter ξ is a parameter containing a Stokes-like contribution. The driving force of the system are thermal fluctuations and are modeled through the $\boldsymbol{f}$ term of the above equation which is a stochastic force of mean zero.

The authors then go on to study the diffusion properties of the chain in the fluid and compare them with other molecular dynamics results. They conclude by saying that the efficiency is greatly increased.

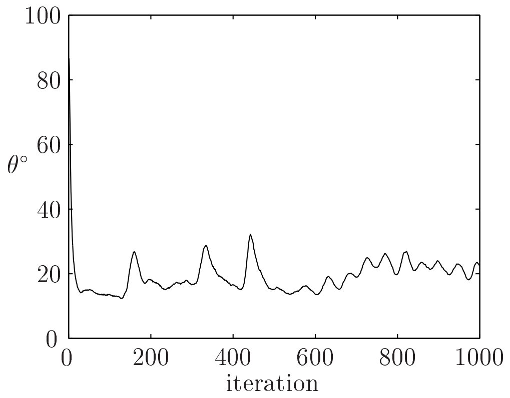

Figure 5.3: The orientation of a single polymer during time. The angle $\theta° = \arctan(ly/lx)$ is obtained by computing the ratio of the horizontal extension lx and vertical extension ly. We clearly evolve from a polymer normal to the flow towards a polymer with an angle of 20°. The fact that the polymer does not orientate is either due to the lack of rotational invariance at the end particles or to some more sophisticated physical effect.

5.4 Multiple Lattice Boltzmann model for viscoelasticity

In this chapter, we make use of the lattice Boltzmann models for fluid and solid and their interaction in order to model viscoelasticity. For a full description of the solid model, we refer the reader to chapter 2 and chapter 3 for the fluid model. The interaction between the fluid and solid models is described in chapter 4. We first present some simulations of a single polymer in a fluid and then perform simulations of a polymerised fluid.

5.4.1 A single polymer

The limitations of the solid model have been discussed in chapter 2. The most notable fact is that the transverse and longitudinal motion are decoupled which also prevents the possibility for rotations. Nevertheless, we first look at the qualitative behavior of a single polymer chain in a fluid. To do so, we place a chain of length $L = 18$ with elastic constant $k = 1/100$ in a shear flow in the direction normal to the flow such that the chain overlaps two regions with opposite velocity. The fluid is obtained by a classical D2Q7 lattice Boltzmann model with $\tau = 1.0$ which corresponds to a viscosity of $\nu = 0.125$. The velocity gradient produces a stress on the chain which first deform and then moves within the fluid. The deformation of the chain for several time steps is shown on figure 5.2 together with the fluid velocity at the chains position. The initial deformation corresponds to the attempt of the chain to orientate in the direction of the flow.

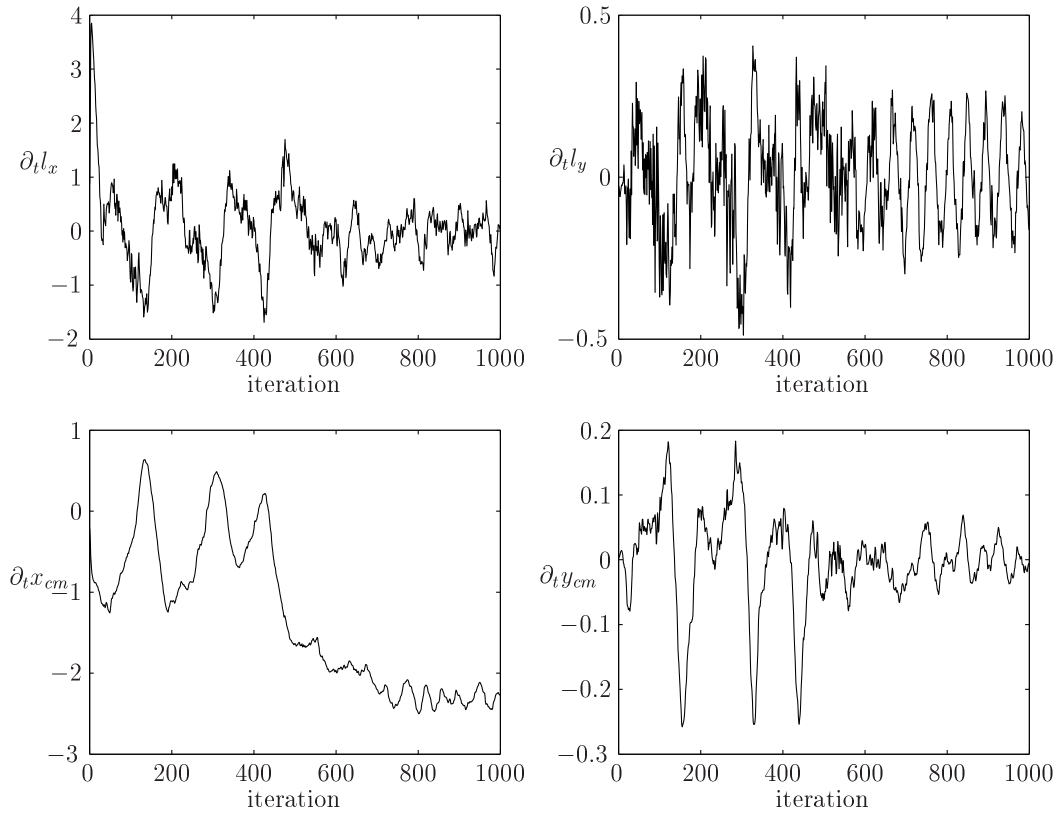

Figure 5.4: The upper plots are the variation of horizontal and vertical extension of a single polymer in a shear flow. The oscillating nature of this variation shows how the polymer reacts to the extension imposed by the flow and demonstrates the finite extensibility of the model. The lower plots show the speed of the center of mass of the polymer. The overall motion is thus a complex combination of forward and backward movements in the flow.

This is clear from the figure 5.3 where the angle $\theta^\circ = \arctan(ly/lx)$ produced by the horizontal extension lx and vertical extension ly of the chain is shown as a function of iteration time. The plots shows that in the initial time steps the polymer relaxes from a 90° angle towards a 0° angle but finally stabilizes at about an angle of 20°. Two observations are to be made. First, the residual angle of a chain in a shear flow is not necessarily expected to be zero due to the fact the chain is also in motion [48]. Second, the tendency of this angle to oscillates is due to the lack of rotational invariance of our solid model which causes the polymer to want to relax to its original orientation. Remarkably though, the chain keeps its integrity and reacts to the extension imposed by the fluid with an oscillating length. The variation of length during time clearly illustrates this as shown on figure 5.4. The chain thus exhibits a natural finite extensibility. On the same figure is also shown the overall motion of the chain and we observe that

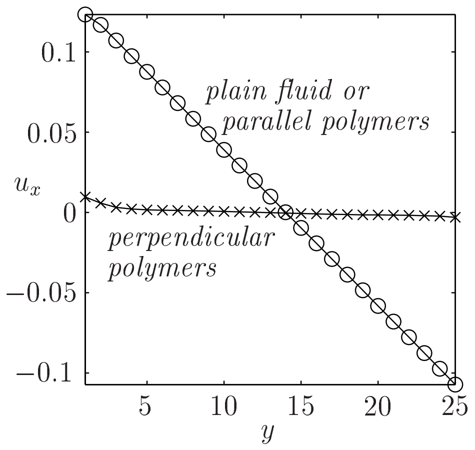

Figure 5.5: Velocity profiles for a plain fluid and a fluid with 2000 polymers perpendicular to the flow. The flat profiles is however still a linear shear flow profile. The gradient differs of almost two orders of magnitude: the plain case exhibits a slope of 0.01 while for the perpendicular case it is worth 0.00022 leading to a apparent viscosity 45 times higher.

it is a complex combination of forward and backward movements within the flow depending on what portion of the chain overlaps a given direction of the flow.

From these small observations, we conclude that although the motion is artificially constrained by the lack of rotational invariance it possesses remarkable properties such as the tendency to orientate, a finite extensibility with a numerically efficient[5] and stable scheme.

5.4.2 A polymerised fluid

We next study a polymerised fluid where a 50×100 D2Q7 lattice Boltzmann model is used for the fluid and a D2Q4 lattice Boltzmann for one dimensional chains in interaction with the fluid. The size of the solid lattice is such as to have about 2000 solid particles in the fluid except for the Deborah number experiment where the number of particles is variable. The average density of solid particles in the fluid sites is thus 0.40 which is sufficient and on average does not allow for more than one solid particle to interact with one fluid site. In the previous section, we have shown that the chains do have a sensible behavior in the fluid and are thus encouraged by the overall possibilities. We do expect the population of polymers to have global non trivial behavior on the flow. The question is obviously whether this behavior will be physically satisfying.

The experiment we perform consists in placing a set of one-dimensional solids (i.e. chains of particles, or pseudo-polymer) in a shear flow $\boldsymbol{u} = (u_x(y), 0)$ with

[5]it is worth mentioning that the simulation can be viewed online on a laptop.

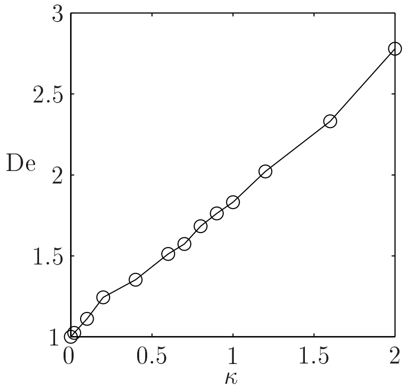

Figure 5.6: The Deborah number De as a function of the density κ of particles in a fluid under shear stress. The characteristic time scale used to calculate the Deborah number is the time needed for a plain fluid to establish a shear flow. This explains why the Deborah number starts at 1. We see that for the given elasticity constant $k = 1$ of the polymers, we are able to obtain a range of Deborah numbers by tuning the density of polymers in the flow.

$\partial_y u_x(y) \neq 0$. We consider the following three situations : first the chains are oriented perpendicular to the flow and extend over several fluid layers; second, the chains are parallel to the flow; finally a mixed system of parallel and perpendicular polymer is investigated. In all cases, we study the properties of the mean velocity profile of the fluid along the channel which for a Newtonian fluid under shear stress follows

$$\tau_{xy} \sim \eta \frac{\partial u_x}{\partial y}$$

where τ_{xy} is the shear stress imposed on the fluid. Indeed, any departure from this law would be the indication that the fluid possesses a non-Newtonian behavior. The shear flow is typically obtained by imposing a constant body force $\boldsymbol{F}$ on all sites with vertical position $y = 0$ and the opposite force $-\boldsymbol{F}$ on all sites at $y = n_y/2$ where n_y is the vertical domain size.

We now discuss the results. In the perpendicular case, see figure 5.5, the velocity profile appears to have been completely suppressed compared to the case with no polymers. The profile is in fact still that of a Newtonian shear flow but with a proportionality constant nearly two orders of magnitude lower. The apparent viscosity of the fluid is therefore strongly increased by the presence of perpendicular polymers. This can be understood from the fact that the perpendicular chains couple layers of fluids with different velocities and tend to force them to have the same speed.

In the parallel case, we start with a fluid at rest and a given density of parallel polymers also at rest. We observe that the stationary velocity gradient is identical

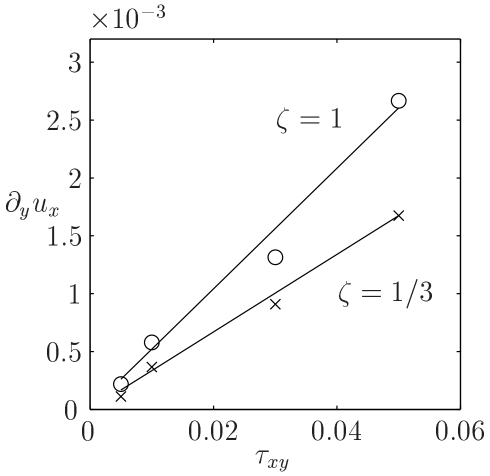

Figure 5.7: The dependency of the gradient of u_x as a function of shear stress. The relation is linear, however the linearity constant and hence the viscosity depends on the ratio ζ between parallel and perpendicular polymers. The two plots are for a total of 2000 polymers and $\zeta = 1$ and $\zeta = 1/3$

to the case of the plain fluid. This is expected since the polymers are now aligned with the fluid layers and do not prevent a velocity gradient to set up. However, the time it takes for the fluid to relax to this stationary velocity profile is dependent of the parallel polymer concentration. To measure the characteristic relaxation time, we simply fit the velocity profile with a first order polynomial, in agreement with the linear relation between stress and velocity in a Newtonian fluid, and look at the evolution of the chi-square χ_2 coefficient during time. The more the profile is linear, the lower the χ_2 coefficient. Since the fluid is initially at rest, the profile takes some time to become linear. Therefore, the time evolution of χ_2 can itself be fitted with an exponential $e^{-\gamma t}$ and the time constant $\gamma = 1/T$ we associate with characteristic time scale of the fluid. Indeed, the solution of Maxwell's equation (5.9) is of the form

$$\sigma = const \cdot e^{-\frac{1}{\lambda}t} - \eta\dot{\varepsilon} \tag{5.21}$$

where $\dot{\varepsilon}$ is a constant strain which we impose on the borders in order to obtain the shear flow in the fluid. Considering that the microscopic characteristic time scale λ of our mixed system is that of a plain fluid T_0, the Deborah number of a fluid with polymers is thus $\mathrm{De} = T_0/T$. The measure of the Deborah number as a function of the density κ of polymers in the fluid which is simply defined as

$$\kappa = \frac{\#solid\ particles}{\#fluid\ sites}$$

is illustrated on figure 5.6 for various values of the number of polymers in the system. Therefore, the presence of parallel chains of particles slows down the response of the fluid to an external stress and from the plot of figure 5.6, it seems we are theoretically unlimited in the value of the Deborah number attainable.

Finally, we study a mixed system of parallel and perpendicular polymers. Given a constant number of polymers, we look at the influence of the shear stress on the velocity profile for two different ratios ζ of parallel and perpendicular polymer densities. As expected from the purely perpendicular case, the velocity profile is several order of magnitude lower than the plain case. However, it does depend linearly with the shear stress as expected from a Newtonian fluid, see figure 5.7. The proportionality constant, i.e the effective viscosity, nevertheless does depend on the ratio of parallel and perpendicular chains. Therefore, by introducing a mechanism enabling a rotation of the polymers, which is not yet the case in this model, we expect to be able to dynamically change the local viscosity and thus introduce a non-Newtonian behavior for the fluid.

It is important to remember that an important issue of this model is to keep all components at the same level of description. At this point, introducing rotations, i.e. angular momentum, in the lattice Boltzmann model of the solid has not yet been possible and may not be for theoretical reasons. We might therefore consider the possibility to put an ad hoc mechanism, similar to that used by Ladd [30], in which the total torque on a object is considered to compute a global rotation of the object.

5.5 Conclusion

In an attempt at modelling a viscoelastic fluid, we have modeled the interaction of a fluid with polymer chains using lattice Boltzmann models for both the solid and fluid. By using the same level of description, we believe a better intuitive modelling is possible. The interaction between the solid and the fluid has been validated in chapter 4. In this chapter, we have first looked at the qualitative behavior of a single chain in a shear flow and observed that the lack of rotational invariance of the solid model mainly introduces an artificial force on the chain which tries to relax to its original orientation. The chain nevertheless does orientate with an additional oscillating motion and does keep its integrity thus exhibiting finite extensibility. The global motion of the chain is non-trivial and the scheme is stable and efficient. Further studies should eventually look at the diffusion properties of the chain and compare these with other models [30] [46].

Next, we have produced a complex fluid by putting a population of chains in a shear flow. We studied properties of the fluid with regards to the orientation of the chains. The apparent viscosity is dependent on the orientation of the polymers. This confirms the needs to introduce the possibility for the chain to rotate, thus given rise to a dynamical variation of viscosity which should eventually lead to non-Newtonian effects in the fluid. Also, the density of the polymers affects the Deborah number of the fluid. A further study could look at the dependence of the Deborah number with the elasticity of the polymer. The model could then be directly put in relation with the Maxwell model of viscoelasticity.

The main limit of this combined model is fact that the solid model does not incorporate the possibility for rotation. There are two solutions to this problem. Either one introduces rotations in a global way with an ad-hoc Newtonian technique without taking into account that our solid is subject to deformation or one has the ambition to model the rotation with a local mechanism. The former approach is a simple technique and is probably the way to go about on a short term basis. The cost would be a slight loss in performance and elegance because the locality of the computation which is inherent to the actual model would be lost. Indeed, since mutual interactions between solid particles are not considered, the computational complexity of the combined fluid and solid model is completely linear with respect to the size of the fluid domain and the number of solid particles. On the other hand, the ad-hoc method may well be the only plausible approach since for the moment there is still no simple way of modelling rotation with a local mechanism. The attempt presented in chapter 2 shows that there is no physical quantities identified for automata which exhibit rotation and the numerical stability is far from clear. Nevertheless, we believe the simulations presented above are very encouraging and that any further developments would grandly serve the emergence of a very efficient tool for simulating and modelling complex fluids.

Chapter 6

A Lattice Gas Model of a Crowd

6.1 Introduction

Crowds or the collective behaviour of pedestrians are of interest for several reasons. The most obvious one is the need from architects and engineers to have tools in order to design buildings, road, subways, etc... with to the least sufficient security and to the most enjoyable urbanistic qualities. From a modelling or theoretical point of view, the motivation arises from the study of the complex phenomena which emerges from the collection of persons. This challenge is highly enhanced from the fact that individuals in a crowd do not make up a deterministic entity such as an electrically charged particle in an electrical field, but are just as much of interest to a psychologist [49] and possibly a riot police officer [1]. There is in fact no clear guiding principle, such as the least action principle in physics, underlying the attempt to model a crowd. It is however observable that crowds demonstrate systematic behaviors for a given situation. Lane formations in crowd moving in opposite directions is such a behavior. The challenge therefore consists in clearly identifying the lowest level of description needed for modelling a pedestrian and still obtain the correct global behavior of a crowd. Systems where the constituents have an apparent free choice in their behavior can legitimately be qualified as autonomous. Autonomous systems can easily be recognized as directly in relation with living organisms. The degree of autonomy may vary. Traffic flow for example has less autonomy than crowds since the behavior of a car is fundamentally governed by law. The modelling is hence simplified as the already wide existing literature testifies [50]. On a conceptual basis, however, the question remains: is there an underlying general principle to autonomous systems which provide more than an empirical frame of work? The answer may still be way ahead of us although the model presented in this chapter and other attempts [51] indicate that most probably a variation of the least principle action is at work. At the moment, thus, the modelling remains

[1] just type "crowd control police" in a search engine!

empirical. In the case of a crowd, fortunately, there exists experimental data to guide and validate the modelling. Therefore, if the level of description and the rules of behavior of a pedestrian in a crowd are identified, the ambition is to be able to simulate large or complex crowds thus yielding practical solutions to engineers.

In the past, the problem of crowd movement has been studied using various approaches ranging from fluid dynamics [52] to coupled Langevin equations [53]. The former approach consists mainly in analytical investigations and for applications a direct simulation of the latter approach is favoured. In the past decade, the use of cellular automata have been introduced as a simple, intuitive yet powerful tool for simulating complex systems and such has been the case for the modelling of a crowd [2]. This latest approach reduces the problem to a local set of rules which describes the motion of pedestrians on a discrete representation of space. The local rules are simple to understand yet still allowing a complex collective behavior to emerge. Apart from being a modelling paradigm in itself, the motivation for using a local set of rules is to highly reduce the computational complexity of a problem and eventually rendering it easily implemented on a parallel computer. Not all problems may be thought of in terms of a local rule and in the case of a crowd, for instance, should the long range interaction of pedestrians be considered as necessary to the model, it will therefore need to be mimicked through a local mechanism in order to keep all the computing advantages.

We propose a new model using a mesoscopic approach inspired by the so-called lattice gas techniques [14] which are in the same stream of thought as cellular automata. This family of models have been successfully used to model fluid dynamics which indirectly hints to the first attempts at crowd modelling [52]. The main novelty of our model consists in relaxing the exclusion principle, by which pedestrians in a crowd cannot occupy the same physical location, to a probabilistic view where pedestrians are in fact allowed to superpose albeit an influence on their movement. The exclusion principle, or what others name *private sphere* [52], is not only the fact that people may not physically occupy the same space but also their tendency to avoid each other. The result of this behavior is to influence the flow of pedestrian and eventually also cause them to be momentarily at rest. In the case of the cellular automata model [54], this principle has a definite influence on the algorithm since any conflict of space will have to be resolved. The main motivation for relaxing this principle, however, arises from the fact that the discretization of space on a lattice does not yield any specific scale. Thus, in the case of a fine scale, i.e. a scale where a lattice site represents the exact area which a pedestrian can occupy, it might be true that two pedestrians may not be on the same site. In the case of a larger scale, however, there is no reason for such a limitation. The details of how pedestrians avoid each other is of little interest since we are finally only interested in their flow. It is therefore natural to consider a critical density ρ_0 below which all pedestrians have free movement and are able to leave a lattice site and above which their mutual interaction will constrain a number of them to slow down and thus remain in the same lattice site.

The chapter is organized in two parts. First, we give a state of the art consisting in the summary of two representative models of past approaches: coupled Langevin equations and a cellular automata model. In the second part, we describe our lattice gas model and validate the approach with classical experiments namely lane formation, oscillation of flow at a door and room evacuation.

6.2 State of the art

6.2.1 The social force model.

The social force model [53] starts with the premise that the behaviour of pedestrians in a crowd are usually automatic and well predictable. This is due to the fact that pedestrians are used to the situation they are confronted with. From this observation, the phenomenological behaviour of one pedestrian can be put into an equation of motion of the Langevin form where changes of speed of pedestrian $\boldsymbol{\alpha}$ are given by

$$\frac{d\boldsymbol{v}_\alpha}{dt} = \boldsymbol{f}_\alpha(t) + \text{fluctuations} \tag{6.1}$$

where $\boldsymbol{f}_\alpha(t)$ is the social force due to the influence of the environment and other pedestrians. The fluctuations take into account any variations of behaviour such as indetermination in front of multiple choice. It is important to note that these forces do not obey classical physics. There is no action-reaction law for instance, energy and momentum are not conserved since the pedestrians are active and can produce internal forces. This particularity is the reason for the “social” qualitative in the name of the model.

At this stage, the model simply consists in considering the various components of the social force. First, given that a pedestrian has a desired direction of motion $\boldsymbol{v}_\alpha^0$, any deviations from this direction in direction $\boldsymbol{v}_\alpha$ are suppressed by a relaxation force with relaxation time τ_α

$$\boldsymbol{f}_\alpha^0(\boldsymbol{v}_\alpha, \boldsymbol{v}_\alpha^0) = \frac{1}{\tau_\alpha}(\boldsymbol{v}_\alpha^0 - \boldsymbol{v}_\alpha) \tag{6.2}$$

Second, pedestrians keep at distance of borders such as building or walls. This is modelled by a repulsive, exponentially decreasing, potential V_B

$$\boldsymbol{f}_{\alpha B}(\boldsymbol{r}_\alpha - \boldsymbol{r}_B^\alpha) = -\nabla_{\boldsymbol{r}_\alpha} V_B(\| \boldsymbol{r}_\alpha - \boldsymbol{r}_B^\alpha \|) \tag{6.3}$$

where $\boldsymbol{r}_B^\alpha$ is the nearest point of border B to the location of pedestrian $\boldsymbol{\alpha}$. Third, pedestrians are considered to keep at a distances from each other and this interaction is thus modelled with a repulsive potential V_β

$$\boldsymbol{f}_{\alpha\beta}(\boldsymbol{r}_\alpha - \boldsymbol{r}_\beta) = -\nabla_{\boldsymbol{r}_\alpha} V_\beta(\| \boldsymbol{r}_\alpha - \boldsymbol{r}_\beta \|) \tag{6.4}$$

which can result in avoidance manoeuvres, deviations, etc. The potential V_β has an elliptical form in the direction of movement since pedestrians require space for their next step. The overall potential felt by one pedestrian is then

$$V_{\text{int}}(\boldsymbol{r}_\alpha, t) = \sum_{\beta \neq \alpha} V_\beta(\boldsymbol{r} - \boldsymbol{r}_\beta(t)) \tag{6.5}$$

The total finally force is

$$\boldsymbol{f}_\alpha = \boldsymbol{f}^0_\alpha + \boldsymbol{f}_{\alpha B} + \sum_{\beta \neq \alpha} \boldsymbol{f}_{\alpha\beta}(\boldsymbol{r}_\alpha - \boldsymbol{r}_\beta) \tag{6.6}$$

and together with

$$\frac{d\boldsymbol{r}_\alpha}{dt} = \boldsymbol{v}_\alpha(t) \tag{6.7}$$

the above equations form a set of non-linearly coupled stochastic differential equations. This set of equations can be simulated on computer using molecular dynamics techniques [55]. The results realistically reproduce observed phenomena such as the formations of lanes of pedestrians moving in the same direction and the alternate flow at narrow passages such as doors. As an illustration, figure 6.1 shows the two phases of the bottleneck situation which can occur at door.

The model is perfectly capable of reproducing sophisticated crowd behaviour. The need to further investigated other approaches is motivated by the fact that very large crowds will require increasing computation power. Indeed, typical molecular dynamics simulation problem have a computational complexity which scales as $O(N^2)$ where N is the number of interacting elements. If the problem under study allows to neglect long range interactions, this complexity can reduce to $O(N)$ albeit the use of sophisticated algorithmic techniques. Therefore approaches which focus on local rules have the potential of naturally reducing the computational complexity to $O(N)$, keeping the simulation algorithm simple and intrinsically adapted to parallel computing.

6.2.2 The cellular automata model.

A cellular automata can be viewed as a two dimensional array where the state of each cell is binary and the evolution of the state depends on the value of the neighboring cells. Cellular automata are generally considered to be simple and intuitive to understand and the locality of their evolution rule makes them naturally adapted to parallel computing. In the case of a crowd [2] [54], the

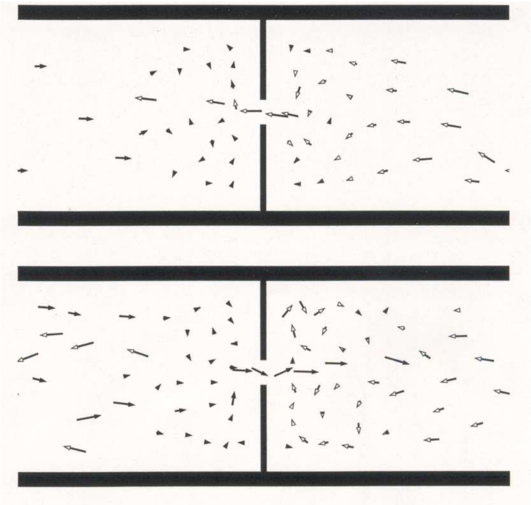

Figure 6.1: Flow oscillation of pedestrians at a door serving as a bottleneck, taken from [1]. The arrows represent the speed $\boldsymbol{v}_\alpha$ of each pedestrian. The top situation shows the right population having gained passage through the door while in the bottom situation the flow is inversed. Both population act as pressure on each other and it is the fluctuations which allow for one pedestrian to pass through the door. Once the first pedestrian gains access, it is easier for the others to follow until the situation inverses again.

automata models the absence or the presence of a pedestrian and the evolution rule describes the movement across the array. A so-called *matrix of preference* M_{ij} encodes the preferred direction of movement and the speed of each pedestrian. It is a 3×3 matrix where the indices ij label the von Neumann neighborhood of a cell. The rule for movement takes into account two considerations: each cell can only be occupied by one pedestrian at once and long range interactions between pedestrians which reflect the ability of a pedestrian to see further ahead are modeled through a local mechanism. The first consideration results in a step of conflict resolution when two pedestrians intend to occupy the same cell. The second consideration is dealt with the use of so-called *floor fields*. These field are described in terms of "bosons" i.e. the field simply has an integer value at each cell. A static floor field S models the properties of the surroundings while a dynamics floor field D models the interaction between pedestrians. The dynamic floor field therefore has an evolution rule of its own. The floor fields are then used with the matrix of preference to compute the probability of transition p_{ij} from one cell to another in the von Neumann neighborhood

$$p_{ij} = N e^{k_D D_{ij}} e^{k_S S_{ij}} M_{ij}(1 - n_{ij})\xi_{ij} \tag{6.8}$$

where N is normalization factor such that $\sum_{ij} p_{ij} = 1$, n_{ij} is the occupation number of the possible target cell and ensures that transitions to occupied cells

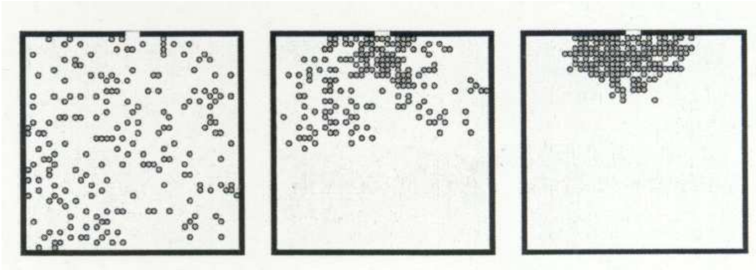

Figure 6.2: Jamming at a door of pedestrian while evacuating a room, taken from [2]. The evacuation problem shows the interesting phenomena of "faster-is-slower". If the crowd moves to the door too quickly, interaction between pedestrians is higher and the total evacuation time is larger. This result has direct implications in evacuations procedures or more precisely in preventive education of pedestrians behavior.

are forbidden, and ξ_{ij} is a geometry factor which is 0 for forbidden cells such as walls.

The dynamic floor field is able to represent the long range interaction of pedestrians by introducing a memory effect. Each pedestrian is considered to momentarily leave a trace of their movement in space and this trace will influence the movement of other pedestrians. The dynamic floor field value increase with the presence of a pedestrian and then obeys a dynamics of decay and diffusion. The advantage of this method is that the long range interaction of pedestrians is modelled through a local mechanism and thus computational complexity remains linear with the number of pedestrians.

Given these definitions, the algorithm for the cellular automata of [2] [54] is the following:

1. update the dynamic field. Each boson of the field decays with probability δ and diffuses with probability α to a neighboring cell.
2. compute the transition probabilities p_{ij}.
3. each pedestrian chooses a target cell.
4. conflicts are resolved.
5. pedestrians which are allowed to move execute their step.
6. the pedestrians alter the dynamic field they occupied $D_{ij} \to D_{ij} + 1$.

This model has been shown to reproduce several collective phenomena of crowd motion [2][54], an example of which is shown on figure 6.2. The main behaviors are lane formation, oscillations at a door and room evacuation. The most interesting result being the observation of a "faster-is-slower" effect in the evacuation time of a room. As the name indicates, the system of pedestrians may produce jamming at the door if the motion to the door of the crowd is too fast. It is shown that with a slower evacuation speed the jamming is reduced and the total evacuation time is lower. This effect directly illustrates the necessity of preventive crowd education when security procedure for buildings and public places are to be elaborated.

6.2.3 Conclusion

The necessity of direct simulation for practical understanding of crowd movement motivates the need to elaborate efficient algorithm. By efficient we mean in accordance with common observations and at low computational cost. Indeed crowds are by definition a collection of numerous pedestrians. With these two aspects in mind, the coupled Langevin equations model clearly shows a very good modelling of the phenomena. The numerical implementation however scales as the square of the number of pedestrians and can be reduced if only short range interaction are considered at the cost of highly complicating the numerical algorithm. This motivates the research in other directions. The cellular automata model thus proposes a local modelling whose complexity is linear and which is easily parallelized. Although capable of reproducing most known emergent behavior, the algorithm however is constrained by the fact that conflicts may arise and that a specific scale is given. In the following section, we propose a lattice gas model for a crowd where in complete adherence to the philosophy of cellular automata we shall model the crowd with local rules. The relaxation of the exclusion principle which we propose does not yield any specific scale of simulation and does not require the model to solve conflicts between pedestrians. This approach is thus nearer to the statistical modelling of a gas.

6.3 The Multiparticle Lattice Gas Automata Model

Lattice gas automata models are a natural extension of cellular automata [14]. As for cellular automata, the evolution rules are local and thus the computational complexity is linear with the number of pedestrians. With complete analogy to the statistical approach of transport phenomena in fluids, more specifically the Boltzmann equation, the dynamics of a lattice gas model consists of a succession of collisions and propagations where the emerging behavior of the system is essentially governed by the collision term [56]. The novelty of adopting such a point of view is that the collision term, suitably chosen, can intrinsically deal with the conflicts arising from pedestrians competing for the same physical location. The exclusion principle generally adopted can thus be relaxed and in principle the scale of the problem can then be arbitrary chosen. Therefore, given a fixed amount of computation power, the precision or granularity of the simula-

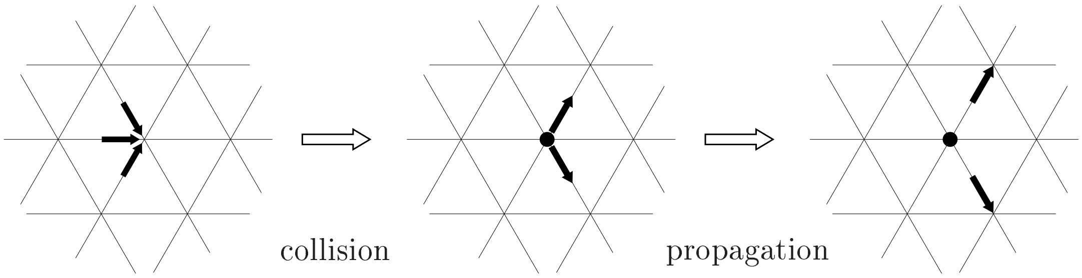

Figure 6.3: The two phases of a lattice gas algorithm. Pedestrians coming from neighboring sites interact in the central site. This results in a redistribution of the pedestrians among possible directions including the rest direction which means a pedestrian will not move during this time step. The propagation step merely consists in moving a pedestrian to the site pointed at by the direction resulting from the collision term.

tion can be chosen so as to take an equivalent amount of time whether one wants to simulate a single corridor or a whole quarter of a town.

The crowd is modeled by the collection of a number N of pedestrians distributed on a 2-dimensional regular lattice with $z+1$ directions $\boldsymbol{c}_i$, $i = 0..z$. The total number of pedestrians $\rho = \sum_{i=0}^{z} n_i(\boldsymbol{r}, t)$ at each lattice site $\boldsymbol{r}$ is arbitrary. In agreement with multiparticle lattice gas formalism, $n_i(\boldsymbol{r}, t)$ denotes the number of pedestrians entering site $\boldsymbol{r}$ at time t along direction $\boldsymbol{c}_i$. Each pedestrian is locally characterized by its favorite direction of motion $\boldsymbol{c}_F$. The movement of a pedestrian is considered to be at $v_{\max} = |\boldsymbol{c}_i|$ towards the site pointed at by the lattice direction $\boldsymbol{c}_i$. The direction labelled $\boldsymbol{c}_0 = 0$ is used to point onto the site itself. It is used to model the rest direction i.e the case when there is no actual movement. The lattice is a D2Q7 hexagonal lattice. This choice is motivated by the fact that all directions have equal norm and it offers a sufficient choice of directions for the movement of a pedestrian.

As is the case in lattice gas systems, the dynamics of the crowd movement is described by two steps: collision and propagation, see figure 6.3. The propagation consists in nothing more than moving a pedestrian to the site pointed at by the lattice direction determined during the collision process. The collision, which unlike physical systems does not conserve any particular quantity but the number of individuals, consists in determining the direction imposed on each pedestrian due to the interaction with other pedestrians occupying the same site. Depending on the strength of the interaction, this imposed direction may or may not correspond to the favorite direction $\boldsymbol{c}_F$ of a pedestrian. The favorite direction is typically a constant or the lattice direction which best corresponds to the shortest path to a given final position. It is part of the autonomy of the pedestrian and is be modelled separately from the dynamics of movement.

In a real crowd, there is no first principle which dictates how the pedestrians

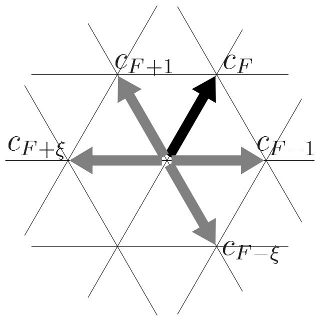

Figure 6.4: A pedestrian may consider several directions in order to find alternate routes. The parameter ξ determines the number of directions neighboring his favored direction $\boldsymbol{c}_F$ that are to be taken into account

are going to interact when they meet. In what follows we propose a new set of rules which are based on common observations. First we assume that the crowd motion is subject to some friction which occurs when density is too high. This will slow down the local average velocity of the crowd by reducing the number of pedestrians allowed to move out of the lattice site. Second, the pedestrians are confronted with the choices of moving in their favorite direction or to move in the direction where flow exists. Finally, each pedestrian can consider only a reduced number ξ of optional directions $\boldsymbol{c}_i$ around its favorite choice $\boldsymbol{c}_F$ when selecting its actual way out of the cell, see figure 6.4

Thus, the factors taken into account in the collision are: the favorite direction $\boldsymbol{c}_F$ of each pedestrian, the local density ρ, i.e. the number of pedestrians per site, and a quantity termed the mobility $\boldsymbol{\mu}(\boldsymbol{r}+\boldsymbol{c}_k, t)$ at all the neighboring cells $\boldsymbol{r}+\boldsymbol{c}_k$. The mobility is normalized measure of the local flow and is simply defined as

$$\boldsymbol{\mu} \quad = \quad \frac{1}{\rho}\sum_{i=0}^{z} n_i \boldsymbol{c}_i \tag{6.9}$$

Parameters of the model are: (1) the critical density ρ_0, i.e. the number of pedestrians per site after which free movement is hindered; (2) a disorder term $\xi \in \{0, z/2\}$; and (3) $\eta \in [0, 1]$ a term describing the will of pedestrians to prefer cells with high mobility. Given these definitions, the collision algorithm is

1. choose the target cell $\boldsymbol{r} + \boldsymbol{c}_t$ among the neighboring cells $\boldsymbol{r} + \boldsymbol{c}_j$ which maximize the quantity

$$2\eta\boldsymbol{c}_j \cdot \boldsymbol{\mu}(\boldsymbol{r} + \boldsymbol{c}_j, t) + 2(1 - \eta)\boldsymbol{c}_j \cdot \boldsymbol{c}_F \tag{6.10}$$

where F labels the favorite direction and $j = F, F \pm 1, .., F \pm \xi$. Directions $F + i$ and $F - i$ are considered in random order to avoid a systematic bias in case of an equal score.

2. move to target cell $\boldsymbol{r} + \boldsymbol{c}_t$ with probability

$$P = \begin{cases} 1 & \text{if } \rho \leq \rho_0 \\ \rho_0/\rho & \text{if } \rho > \rho_0 \end{cases} \tag{6.11}$$

   otherwise stay in current cell $\boldsymbol{r}$ (i.e. pick direction $\boldsymbol{c}_0$).

Lets first consider the probability of moving: it is constructed such that in a densely occupied cell, the number of people allowed to move is on average ρ_0. A possible interpretation for this rule is that only people at the boundary of the area of the cell are able to move.

Second, once a pedestrian is allowed to move, the choice of the destination cell is mainly governed by the agreement between the mobility at a given cell $\boldsymbol{\mu}(\boldsymbol{r} + \boldsymbol{c}_j, t)$ and the direction $\boldsymbol{c}_j$ needed to reached the cell which is given by the first term of equation (6.10). This reflects the need to find mobility in a dense crowd. On the other hand, the mobility found at $\boldsymbol{r} + \boldsymbol{c}_j$ should not completely outweigh the fact that an pedestrian possesses a favorite direction $\boldsymbol{c}_F$. Hence the presence of the second term in equation (6.10) which measures the agreement between the considered direction $\boldsymbol{c}_j$ and the favorite direction $\boldsymbol{c}_F$. Therefore, movement towards a cell which opposes $\boldsymbol{c}_F$ is only possible if high mobility compensates the backtracking.

The η factor is a parameter which determines whether the crowd will generally prefer mobility or its favorite direction. A value of $\eta = 1/2$ means both scalar products have equal weight. In the present model this is a free parameter. However, it is more probable that in reality this should dynamically depend on the situation of a pedestrian e.g. even in a dense crowd backtracking just before reaching an exit door is never considered while it might be an issue long before reaching the exit.

The disorder parameter ξ represents the ability to keep focused on the favorite direction($\xi = 0$) or to consider neighboring cells i.e. directions($\xi > 0$). Therefore the effect of ξ can be viewed as the ability to explore the environment with the side effect of diffusing the pedestrian. Among other, we consider this as a way of modelling panic. The definition of panic is however situation dependent: a stressed pedestrian with a clear destination will not consider any other direction but his favorite one, namely $\xi = 0$; on the contrary if there is no clear destination, one might choose to explore all directions, namely $\xi = z/2$, in the hope of finding a hidden way out.

To create a sufficiently diverse crowd, the parameter ξ is initially randomly chosen for each pedestrian. For the sake of convenience, we would like to generate this diversity using a continuous parameter $\lambda \in [0, \infty[$ which describes the mean behavior of the crowd. We therefore use a discretized power-law distribution, namely we compute $\xi = [(4x^{\frac{1}{\lambda}})]$ where $[]$ is the integer part function and $x \in [0, 1]$ is a random variable uniformly distributed.

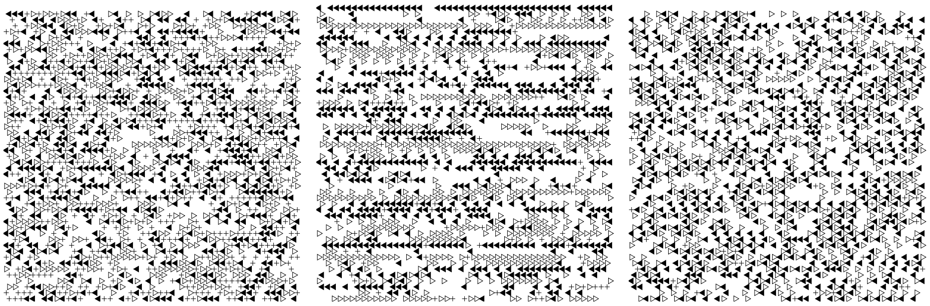

Figure 6.5: Lane formation in a crowd. Three different situations are depicted, which correspond to different values of the models parameters. The left picture shows a crowd with no lanes: movement is essentially a sequence of collision with no deviation. The center picture shows the presence of dense lanes where pedestrians strongly follow each other. The right picture shows a sparse lane where pedestrians spread over the whole space. Black triangles indicate cells in which the mobility points to the left, whereas white ones indicate that the mobility points to the right. A cross shows a cell with zero mobility.

With this method, ξ will take integer values between 0 and 3. The probability that $\xi = l$ is given by

$$\begin{aligned} P(\xi = \ell) &= P(\ell \leq 4x^{1/\lambda} < \ell + 1) \\ &= P\left(\left(\frac{\ell}{4}\right)^{\lambda} \leq x < \left(\frac{\ell+1}{4}\right)^{\lambda}\right) \\ &= \left(\frac{\ell+1}{4}\right)^{\lambda} - \left(\frac{\ell}{4}\right)^{\lambda} \end{aligned} \tag{6.12}$$

These probabilities result in a mean value of

$$\langle \xi \rangle = 3 - \frac{3^{\lambda} + 2^{\lambda} + 1}{4^{\lambda}}$$

When $\lambda \to 0$, ξ is always equal to 0 which means no pedestrian ever considers any other cell but its favorite direction; with a value of $\lambda = 1.0$, values of ξ are equiprobable with $\langle \xi \rangle = 3/2$. For higher values of λ the density of pedestrians with $\xi = 3$ increases. Again the actual value of ξ is probably situation dependent and should vary dynamically.

6.4 Numerical results

All simulations in this section were obtained using a hexagonal lattice with 2500 pedestrians and $\rho_0 = 2$ with an object oriented code C++ code[57] running on a single processor with CPU clock at 700MHz under Linux.

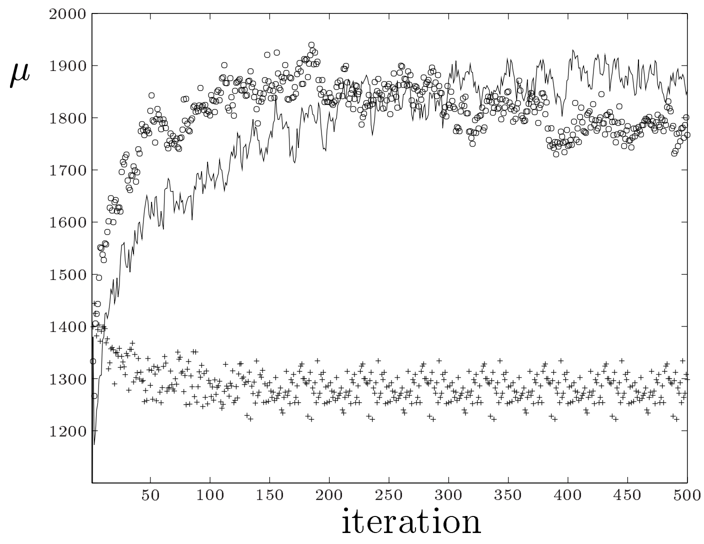

Figure 6.6: A measure of total mobility in a crowd for the three cases shown in figure 6.5:(squares) no lanes $\lambda \approx 0, \eta \approx \frac{1}{2}$, (diamonds) dense lanes $\lambda \approx 1, \eta \approx \frac{1}{2}$,(line) sparse lanes $\lambda \approx 0, \eta \approx 1$. Note that the maximum value of the total mobility is 2500, i.e. the total number of pedestrians.

6.4.1 Lane formation

The formation of lanes in two crowds moving in opposite directions is one of the macroscopic collective behavior of interests to validate our approach. Figure 6.5 shows the three types of states the model is able to produce. The first is a state with no lanes, pedestrians do not consider deviation form their favorite direction ($\lambda \approx 0$) and create high density cells where movement is reduced. The second is a dense lane formation with pedestrians strongly following each other($\lambda \approx 1, \eta \approx \frac{1}{2}$) even when no obstacles are present. The third is a sparse configuration of pedestrians where pedestrians have optimized the space occupation, ($\lambda \approx 0, \eta \approx 1$). This configuration might be due to the effect of sub-lattices. Sub-lattices are simply the effect of pedestrians "crossing" each other during the propagation step and not having performed any mutual collision since they did not belong to the same lattice site. The ability of the crowd to optimize its total mobility $\boldsymbol{\mu} = \sum_{\boldsymbol{r}} \boldsymbol{\mu}(\boldsymbol{r}, t)$ under the three above conditions is shown in figure 6.6. We see that the global behavior of the crowd is highly dependent of η and $\langle \xi \rangle$ which leads us to conclude that a realistic simulation must most probably include a mechanism which dynamically sets the values of η and ξ with regards to circumstances. However, without this sophistication, the system qualitatively behaves in a correct way. Indeed, the optimization of mobility occurs because it has specifically been chosen in our algorithm. The fact that from it emerges the formation of lanes is a hint that some variation of a least action principle

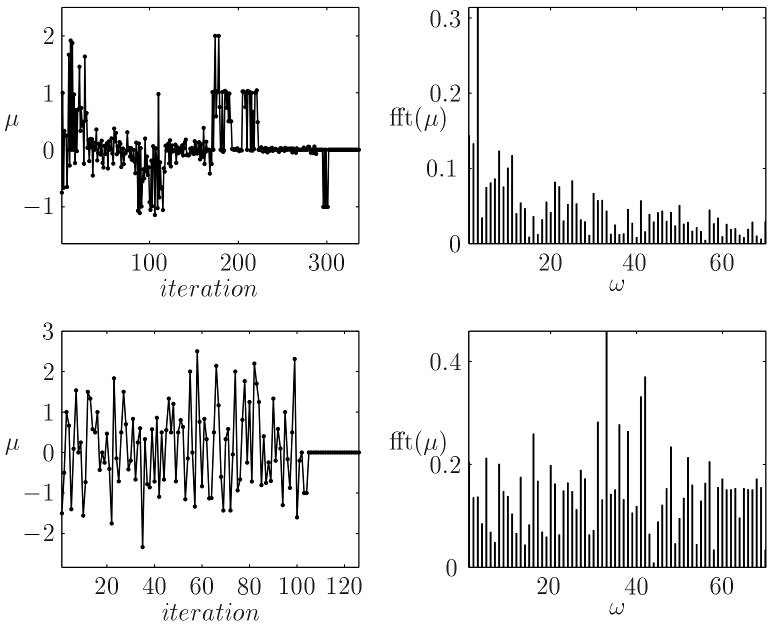

Figure 6.7: Measure of total mobility(left) and its Fourier transform(right) at a door of width 3 in a 200×50 hexagonal lattice with a wall at $x = 100$. The bottom plots are obtained with pedestrians who do not interact. This measure serves as a test of the noise at the door due to the initial random configuration of the crowd. The top plots are the ones with an interacting crowd: we observe higher amplitude peaks at low frequency showing that the two crowd gain access through the door with oscillations.

underlies the behavior of pedestrians as an autonomous system.

6.4.2 Door oscillations.

We now look at the oscillations at a door between two crowds moving in opposite directions. The door serves as a bottleneck and jamming naturally ensues at the door. Oscillations appear when, for noise fluctuations reasons, a population on one side of the door wins access through the door thus finally increasing mobility for people behind. This results in a burst of one population through the door until fluctuations will inverse the situation.

Since in this model pedestrian are in fact allowed to occupy the same cell simultaneously, it is not obvious to visualize the appearance of oscillations at the door. Therefore in order to shows the bursts, we measure the total mobility at the door and compare it with a test simulation where no interaction ($\rho_0 > \rho, \eta = 0$) occurs between pedestrians. In order to outline the oscillations, we look at the Fourier transform of the signal, see figure 6.7. We thus observe that the

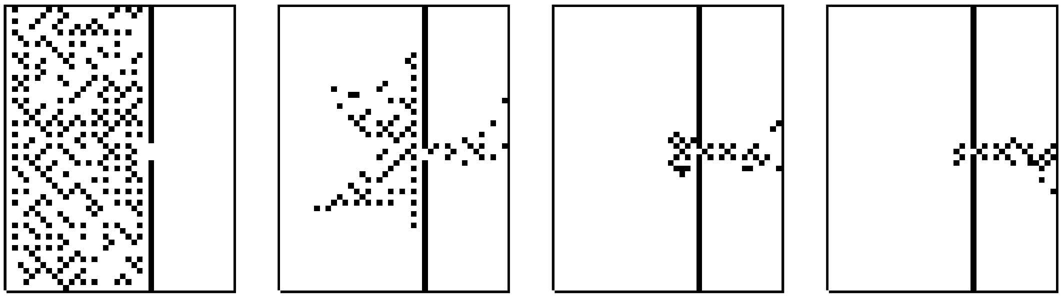

Figure 6.8: The evacuation of 2500 pedestrians out a room through a single door. Initially the crowd is randomly distributed. In the first few time steps, the whole crowd gathers around the door and creates jamming. The time of evacuation as a function of the disorder parameter ξ is shown on figure 6.9.

Fourier transform of the signal for interacting crowd possess higher amplitudes at low frequencies. This shows that the throughput across the door oscillates over periods of time significantly higher than an iteration. The test simulation also has frequencies higher than an iteration but it does not posses a structure whereas the interacting crowd does.

6.4.3 Evacuation problem

In the third experiment we look at the influence of the disorder parameter ξ on the time needed for a crowd to evacuate a room, see figure 6.8. The ξ parameter statistically determines how much a pedestrian will search in other directions to find mobility. By doing so however we increase the diffusion of pedestrians and should consequently increase the time needed to reach the door, thus increase the total time to evacuate the room. Due to the threshold on the density, however, we observe a "faster-is-slower" effect, see figure 6.9. The average effect of increasing $\langle\xi\rangle$ is to lower evacuation time. Indeed, as λ increases, we observe a decrease of the number of iterations needed to evacuate all the pedestrians initially placed in the room. The somehow oscillating structure of the plot is not yet understood; among possible explanations are the effect of the finite values of scalar product in equation (6.10) or an effect of sub-lattices.

6.5 Conclusion

We propose a new model to describe the dynamic of pedestrians using local rules of evolution. The model is inspired by the lattice gas techniques also used in fluid dynamics. The main novelty consists in create a evolution rule independent of the scale of the problem. The exclusion principle usually taken for granted in crowd modelling is thus relaxed. The resulting algorithm is easy to understand and to implement either on a sequential computer or parallel supercomputer.

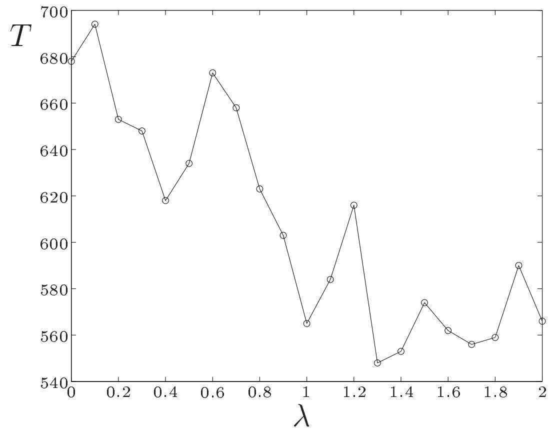

Figure 6.9: The time T needed to evacuate a room as a function of λ. Low λ means people do not consider other directions than the favorite one. The plot shows that by increasing the directions considered and thus slowing the mean velocity to the door, higher throughput is achieved and the total evacuation time is reduced. The plot is the result of single runs with all pedestrians on one side of wall with a door of size 3.

The ingredients of the evolution rule are: above a critical density ρ_0, movement is hindered but not forbidden, pedestrian try to increase either their agreement with their desired direction or the mobility they achieve by slightly changing direction. These features are modelled with two parameters: η weighs the strategy a pedestrian adopts and ξ defines the number of alternate directions he considers. These parameters have fixed values in the simulation and to be more realistic, they should most probably vary dynamically during the simulation. They are in fact situation dependent. Indeed, a pedestrian may change strategy depending on whether he may be far or near a exit door for example. These further possible developments considered, the model does show a good ability to reproduce complex collective behavior of crowds such as the lane formation, flow oscillation at a door and room evacuation.

The fact that pedestrian constitute autonomous system enhance the difficulty of the modelling. To tackle this autonomy problem, we have, in our model, explicitly incorporated a mechanism to search for the local optimum situation. The question is to see whether this produces a better global behavior out of the collective behavior. For the lane formation experiments it has worked well: for a well chosen set of parameters, the crowd, i.e. the collective behavior of individuals with local rules, is able to increase its total mobility. The same optimisation mechanism is also able to reproduce the other expected behaviors of a crowd. Thus, this constitutes a strong indication that a sort of the least action principle is at work even in autonomous system. There may be more theoretical tools than empirical modelling available for the study of such systems.

Chapter 7

Conclusion

The subject of the work presented in this dissertation has been the use of the mescoscopic approach to the modelling of complex phenomena. This approach founded on ideas from statistical physics can be summarised as follow: describe a phenomena from the essential properties of its constituents, the details cancel out. Indeed, most understanding of complex systems are obtained without incorporating all the details. We thus try to move from a microscopic level, which should in theory contains all physical laws known to this day, to a intermediate or mesoscopic level of description. The confirmation that the essential ingredients have been correctly identified is obtained once the correct macroscopic behavior of a system is recovered. The advantages of this approach are twofold. First, identifying the essential basis of a phenomena does require a better understanding of the phenomena itself. It does not necessarily mean that we know how to control it though. Indeed, the predictive power is often set aside to the advantage of a computer simulation. This directly brings us to the second point. Having now to deal only with simple ingredients, the efficiency of simulations is consequently greatly enhanced. It is worth repeating: the benefits, when successful, of this approach brings greater understanding and greater numerical performance to numerical simulations.

Mesoscopic modelling has been developed in this dissertation through the study of five different, sometimes related, phenomena: solid dynamics, fluid dynamics, solid and fluid interface, viscoelasticity and the motion of a crowd. The first four subjects are physical problems some of which are well known. Again, our approach aims at a better understanding of the physics even when it is more than three centuries old as is the case of the solid model in chapter 2. Nonetheless, this renders the modelling more constraining since it is ultimately an obligation to recover all the known theory. The price to pay, however, is not high compared to the prize to collect which includes very efficient numerical schemes and often the possibility to simulate new complex situations.

The last subject, the motion of a crowd, differs from the other problems in the sense that there does not exist any formal theory underlying it. At first, this does allow for more liberties in the modelling but later the question arises how much these liberties were not deliberately chosen to yield the correct behavior. The interest of this problem, however, really resides in the fact that is a good example of an autonomous system. Autonomous systems differ from physical systems in that there is an intrinsic freedom in the constituents of the system. The question which arises therefore is “how much freedom?”. As we have seen, the collective behavior of autonomous pedestrians does obey certain rules and therefore the freedom of an autonomous system constrained by the environment. Our crowd model shows that the mesoscopic approach is perfectly suited to model such systems and might even shed light on what kind of principle akin to the least action principle of physics may be underlying the behavior of autonomous systems.

With all its marvelous possibilities, our approach is not a direct road. Indeed, the path is full of drawbacks. First, identifying the essential ingredients of a problem is not always an easy task, although this in itself is very enlightening. Indeed, it is never very clear what has been lost on the way to the mesoscopic level as the incomplete elasticity of lattice Boltzmann model for a solid has shown. Simplified assumptions may well work wonderfully in some and not at all in other, it is thus very time consuming to try and distinguish what is good and bad in a given experiments. On top of this, numerical instabilities may well appear as an unexpected jack-in-the-box and completely crush all hopes of ever finding a way out. The road is arduous but again it is worth it. The reason to this is that not only that the outcome might one day serve the purposes of an engineer but the whole process in itself requires the qualities which are the living core of science and anyone on this road can only be enriched by the journey.

Bibliography

[1] Dirk Helbing, Peter Molnar, and Frank Schweitzer. Computer simulations of pedestrians dynamics. *Evolution of Natural Structures*, pages 229–234, 1994.

[2] C.Burstedde, K.Klauck, A.Schadschneider, and J.Zittartz. Simulation of pedestrian dynamics using a two-dimensional cellular automaton. *Physica A*, (295):506–525, 2001.

[3] R.Feynman, R.Leighton, and M.Sands. *The Feynman lectures on physics*. Addison-Wesley publishing company, 1964.

[4] J.D. Achenbach. *Wave Propagation in Elastic Solids*. North-Holland, 1973.

[5] L.B. Freund. *Dynamics fracture mechanics*. Cambridge Monographs on Mechanics and Applied Mathematics, 1989.

[6] Eli Sternberg. On the integration of the equation of motion in the classical theory of elasticity. *Archive for Rational Mechanics and Analysis*, 6:34–50, 1960.

[7] Farid F. Abraham, D. Brodbeck, R. A. Rafey, and W. E. Rudge. Instability dynamics of fracture: a computer simulation investigation. *Physical Review Letters*, 73:272–275, 1994.

[8] Huajian Gao, Yonggang Huang, and Farid Abraham. Continuum and atomistic studies of intersonic and supersonic crack propagation. http://www.eng.abdn.ac.uk/~apm2002/abstracts/Gao_Huang_Abraham-1/Gao_Huang_Abraham-1.html.

[9] Y. Dumont, D. Goeleven, M. Rochdi, and M. Shillor. Simulations of beam's vibrations between stops. submitted.

[10] Bastien Chopard. A cellular automata model of large-scale moving objects. *J. Phys. A: Math. Gen*, 23:1671–1687, 1990.

[11] G. Kron. Equivalent circuit of the field equations of maxwell. *Procs IRE*, 32:289–299, May 1944.

[12] Wolfgang J. R. Hoeffer. The transmission-line matrix method. theory and applications. *IEEE Transaction on microwave theory and techniques*, MTT-33(10):882–893, oct 1985.

[13] Kerson Huang. *Statistical Mechanics.* John Wiley and Sons, 2nd edition, 1987.

[14] Bastien Chopard and Michel Droz. *Cellular Automata Modeling of Physical Systems.* Cambridge University Press, 1998.

[15] P. Bhatnagar, E.P. Gross, and M.K. Krook. A model of collision processes in gases. *Physical Review Letters*, 94(511), 1954.

[16] H.J.Herrmann and S.Roux, editors. *Statistical models for the fracture of disordered media.* Elsevier Science Publishers B.V(North-Holland), 1990.

[17] X. He and L.-S. Luo. Lattice Boltzmann model for the incompressible Navier-Stokes equation. *J. Stat. Phys.*, 88:927–944, 1997.

[18] F.J. Alexander, H.Chen, S.Chen, and G.D. Doolen. Lattice boltzmann model for compressible fluids. *Physical Review A*, 46(4):1967–1970, 1992.

[19] L.Landau and E.Lifchitz. *Mécanique des fluides.* Editions Mir, Moscou, 1971.

[20] Kerson Huang. *Statistical Mechanics.* J.Wiley and sons, 2nd edition, 1963.

[21] Bastien Chopard, Alexandre Dupuis, Alexandre Masselot, and Pascal Luthi. Cellular automata and lattice boltzmann techniques: An approach to model and simulate complex systems. *Advances in complex systems*, 5(2):1–144, 2002. special issue on: Applications of Cellular Automata in Complex Systems.

[22] Y.H. Qian, D. d'Humieres, and P. Lallemand. Lattice BGK for Navier-Stokes equation. *Europhysics Letters*, 17(6):479–484, 1992.

[23] Hai ping Fang, Rong zhen Wan, and Zhi fang Lin. Lattice boltzmann model with nearly constant density. *Physical Review E*, 66:036314, 2002.

[24] X. Shan and H. Chen. Simulation of nonideal gases and liquid-gas phase transitions by the lattice boltzmann equation. *Phys. Rev. E*, 49:2941–2948, 1994.

[25] T. Inamuro, M. Yoshino, and F. Ogino. A non-slip boundary condition for lattice boltzmann simulations. *Physics of Fluids*, 7(12):2928 – 2930, 1995.

[26] Alexandre Dupuis. *From a lattice Boltzmann model to a parallel and reusable implementation of a virtual river.* PhD thesis, University of Geneva, June 2002. `http://cui.unige.ch/spc/PhDs/aDupuisPhD/`.

[27] J.R. Womerlsey. . *Journal of Physiology*, 127:553, 1955.

[28] Bastien Chopard and Alexandre Dupuis. A mass conserving boundary conditions for lattice boltzmann models. In *LGA2002*.

[29] Haiping Fang, Zuowei Wang, Zhifang Lin, and Muren Liu. Lattice boltzmann method for simulating the viscous flow in large distensible blood vessels. *Physical Review E*, 65:051925, 2002.

[30] A.J.C. Ladd. Numerical simulation of particulate suspensions via a discretized boltzmann equation. *J. Fluid Mech*, 271:285,310, 1994.

[31] O. Behrend. Solid-fluid boundaries in particle suspension simulations via the lattice boltzmann method. *Phys. rev. E*, 52:1164–1175, 1995.

[32] C.K. Aidun and Y. Lu. Lattice boltzmann simulation of solid particles suspended in a fluid. *J. Stat. Phys.*, 81:49–59, 1995.

[33] D.J. Tritton. *Physical fluid dynamics.* Clarendon Press, 1988.

[34] Alexander J. Smits. *A Physical Introduction to Fluid Mechanics.* John Wiley & Sons, inc., 2000.

[35] A.Artoli, A.Hoekstra, and P.Sloot. Simulation of a systolic cycle in a realistic artery with the lattice boltzmann bgk method. In *LGA2002*, 2002.

[36] R.W Whorlow. *Rheological techniques.* Halsted Press, 1980.

[37] H.Temmen, H.Pleiner, M.Liu, and H.Brand. Convective nonlinearity in non-newtonian fluids. *Physical Review Letters*, 84(15):3228–3231, 2000.

[38] J.G. Oldroyd. On the formulation of rheological equations of state. *Proceedins of the Royal Society of London A*, 200(1063):523–541, 1950.

[39] Jochen Kronjäger. Numerical studies of viscoelastic shear turbulence. Master's thesis, Phillipps-Marburg University, 2001. http://www.physik.uni-marburg.de/kosy/Kronjaeger/diplom.pdf.

[40] J.E.Marsden and T.J.R.Hughes. *Mathematical foundations of elasticity.* Dover Publications, New York, 1994.

[41] Robert Owens and Tim Phillips. *Computational Rheology.* Imperial College Press, 2002.

[42] R.B. Bird and J.M. Wiest. Constitutive equations for polymeric liquids. *Ann. Rev. Fluid. Mech*, 27:169–193, 1995.

[43] E. Aharonov and D. Rothman. Non-newtonian flow (through porous media): a lattice boltzmann method. *Geophys. Res. Lett.*, 20:679–682, 1993.

[44] N.Rakotomalala, S.Salin, and P.Watzky. Simulations of viscous flows of complex fluids with a bhatnagar, gross and krook lattice gas. *Phys.Fluids*, 8(11):3200–3202, 1996.

[45] L.Giraud, D.D'Humières, and P.Lallemand. A lattice Boltzmann model for jeffreys viscoelastic fluid. *Europhysics Letters*, 42(6):625–630, 1998.

[46] Patrick Ahlrichs and Burkhard Dunweg. Simulation of a single polymer chain in solution by combining lattice boltzmann and molecular dynamics. *Journal of Chemical Physics*, 111:8225, 1999.

[47] Daan Frenkel and Berend Smit. *Understanding Molecular Simulation*. Academic Press, 2002.

[48] T.Biben and C.Misbah. Tumbling of vesicles under shear flow. to be published.

[49] Carl Couch. Collective behavior: an examination of some stereotypes. *Social Problems*, 15:310–322, 1968.

[50] *Network and Spatial Economics*, 2003.

[51] Serge P. Hoogendoorn. Walker behaviour modelling by differential games. unpublished.

[52] D.Helbing. A fluid-dynamic model for the movement of pedestrians. *Complex Systems*, 6(391):391 – 415, 1992.

[53] D.Helbing and P.Molnar. Social force model for pedestrian dynamics. *Phys. Rev E*, 51(5):4282, 1995.

[54] Andreas Schadschneider, Ansgar Kirchner, and Katsuhiro Nishinari. Ca approach to collective phenomena in pedestrian dynamics. In Stefania Bandini, Bastien Chopard, and Marco Tomassini, editors, *Cellular Automata*, number 2493 in LNCS, pages 239–248. Springer, 2002.

[55] Farid Abraham. Computational statistical mechanics. methodology, applications and supercomputing. *Advances in Phyics*, 35(1):1–111, 1986.

[56] Stefan Marconi and Bastien Chopard. A multiparticle lattice gas automata model for a crowd. In Stefania Bandini, Bastien Chopard, and Marco Tomassini, editors, *Cellular Automata*, number 2493 in LNCS, pages 231–238. Springer, 2002.

[57] Alexandre Dupuis and Bastien Chopard. An object oriented approach to lattice gas modeling. *Future Generation Computer Systems*, 16(5):523–532, March 2000. Best selected papers from HPCN'99.